Experimental research into the stability of crown walls on a rubble mound breakwater

Master of Science Thesis

D.J.E. Vos

Marine ingenuity

TKI DELTATECHNOLOGIE

Experimental research into the stability of crown walls on a rubble mound breakwater

Master of Science Thesis

by

D.J.E. Vos

in partial fulfilment of the degree of Master of Science
at the Delft University of Technology,
defended publicly on September 25, 2024 at 15:00

Thesis committee:

Student number:	4443179	
Chair:	Prof. Dr. ir. M. R. A. van Gent	TU Delft & Deltares
Supervisors:	Dr. ir. B. Hofland	TU Delft
	Ir. D. C. P. van Kester	TU Delft & Van Oord
	Dr. ir. A. Antonini	TU Delft
Place:	Faculty of Hydraulic Engineering, Delft	
Project Duration:	September, 2023 - September, 2024	

Faculty of Civil Engineering · Delft University of Technology

Preface

This Master Thesis research project is the concluding phase of my pursuit of a master's degree in Civil Engineering at Delft University of Technology, specializing in Hydraulic Engineering. Embarking my own research project has been an exciting and challenging experience. It has given me the opportunity to engage with all aspects involved in conducting research projects. The project was carried out on behalf of the Dutch marine contractor Van Oord. The experimental investigation was conducted at the Waterbouwlab of the Faculty of Civil Engineering in Delft, the Netherlands. The collaboration between TU Delft and Van Oord has resulted in an increase in understanding regarding the stability of a crown wall situated on top of a rubble mound breakwater.

I commenced this study in September 2023. Now, a year later in September 2024, I am pleased to publish the definitive version of this thesis. This achievement would not have been possible without the assistance of numerous individuals. At first, I would like to express my gratitude to the members of my graduation committee: Dr. Ir. B. Hofland, Prof. Dr. Ir. M.R.A. van Gent, Ir. D.C.P. van Kester and Dr. Ir. A. Antonini. The committee meetings were stimulating, and you offered valuable information, perspective and critique. I would like to express my gratitude to Bas Hofland, my supervisor at TU Delft, for his exceptional enthusiasm during every meeting and extensive expertise. His support and guidance were vital in keeping me motivated throughout this research endeavor. I am especially grateful to my supervisor, Dennis van Kester X, from Van Oord, for offering valuable practical knowledge, providing clear direction, and consistently taking the time to address any questions I had about the topic and model tests. I express my gratitude to the Waterbouwlab personnel for their assistance in configuring the model and addressing many practical obstacles.

On a personal note, I want to express my deep and sincere gratitude to my family, especially my parents and brother for their unparalleled love, support, and encouragement throughout my entire study. They have always believed in me and formed the basis for who I am as a person. In particular, I want to thank my father for the inspiration and motivation to continue my studies. Additionally, I am thankful for my friends, who helped me balance studying and relaxing. Without the unwavering support of all these people, I would not have been able to complete this journey.

Abstract

This report examines the pressures and forces on, and stability of crown walls on top of rubble mound breakwaters. Crown walls, installed at the crest of these breakwaters, are designed to reduce the material used compared to conventional breakwaters. Crown walls reduce wave overtopping and facilitate access to the breakwater, thereby providing several functional advantages. Despite extensive research on this topic, uncertainties persist regarding the horizontal and vertical forces acting on crown walls. Consequently, the main objective of this study is to advance the understanding of wave loading on these structures and address existing gaps in the literature. What distinguishes this study from previous research is its focus on determining the instantaneous horizontal and vertical loads, to avoid overly conservative estimates that arise from using the maximum values of both forces. Previous studies have identified the foundation level, or base freeboard, as an important parameter influencing uplift forces, and therefore will be a central focus of this study. Furthermore, the impact of core permeability on these forces was explored.

In this study, physical model tests were used to address the identified knowledge gaps. The tests were performed in the wave flume at the Hydraulic Engineering Laboratory of the University of Technology in Delft, using a model of a rubble mound breakwater with a crown wall at the crest. A relatively standard breakwater model was selected to ensure the broad applicability of the results. The setup included 13 temperature shock-proof sensors— 7 positioned in the base and 6 in the wall — partially protected by an armour layer in front of the crown wall. Various hydraulic parameters were systematically varied during the tests, including wave height, wave steepness, and water level (base freeboard), along with different geometric breakwater configurations. The influence of these variables on wave loading was analyzed, encompassing pressures, forces, and stability, referred to as the factor of safety in this study. The investigation also examined the point of failure, or the minimum factor of safety, to gain additional insights. Furthermore, by rebuilding the model with a different core, the impact of permeability on the forces and stability of a crown wall was assessed.

The tests reveal that for each increase in base freeboard level, the uplift forces decrease by approximately 70%, with a larger reduction observed for swell waves than for storm waves. The reduction in horizontal forces was found to be roughly 50% for each increase in base freeboard level and is identical for both tested wave steepnesses. For both tested permeabilities (0.16 m/s and 0.10 m/s), the decrease in vertical forces is 36% and 46% for storm waves and swell waves, respectively. Additionally, at the lower permeability, an increase in horizontal forces of 47% is observed for storm waves and 10% for swell waves. The findings in this report indicate that most design methods do not align with the measured results, particularly at non-zero foundation levels. This misalignment is largely attributed to underlying assumptions, such as the presumption that both force peaks occur simultaneously, and subsequently result in failure. For two of the methods a correction factor is proposed, accounting for scenarios involving non-zero freeboard levels. Additionally, the findings indicate that failure is not attributable to the simultaneous occurrence of maximal horizontal and vertical forces, but rather by a combination of instantaneous loads, in which one force typically reaches its maximum value while the other has a lower value. Therefore, an additional factor is introduced, which considers this interaction between both and includes base freeboard level. This two-step method, derived from the data, allows for compensation of existing design methods to more accurately estimate wave loads. Subsequently, the results demonstrate that permeability significantly affects wave loads on crown walls. Reducing permeability results in lower uplift forces but, simultaneously increases runup, thus, increases horizontal forces. This has negative implications for stability, as the crown wall becomes less stable on a less permeable core. These findings underscore the importance of horizontal forces at the point of failure. From the findings of this research, the current knowledge on crown wall stability and forces acting upon it is enhanced, providing better approaches for the design and analysis of crown walls.

Contents

Nomenclature

List of Symbols

α	Slope angle breakwater	[°]
Δt	Time lag between maximal horizontal and vertical pressure	[s]
μ_s	Friction factor	[-]
ρ_w	Density of water	$[kg/m^3]$
σ	Surface tension	[N/m]
ξ	Iribarren (breaker parameter): tan $\alpha/\sqrt{\frac{H_s}{L}}$	[-]
ξ_{0m}	Irribarren based on L_{0m}	[-]
A_c	Armour crest freeboard	[m]
B_a	Armour berm width	[m]
B_c	Base length of the crown wall	[m]
$C_{F,V}, C_{F,b}$	Empirical coefficient for the vertical force	[-]
d	Height of the structure	[m]
d_a	Thickness of the armour layer	[m]
d_c	Height of the crown wall	[m]
$d_{c,prot}$	Protected part of the crown wall	[m]
d_{ca}	Unprotected part of the crown wall	[m]
$d_{n,15\%}$	15% - value of the grading curve	[m]
$d_{n,50\%}$	50% - value of the grading curve	[m]
$d_{n,85\%}$	85% - value of the grading curve	[m]
F	Force exerted on the crown wall	[N/m]
F_b	Base freeboard of the crown wall	[m]
F_g	Self weight of the crown wall	[N/m]
F_H	Horizontal force acting on the crown wall	[N/m]
F_V	uplift force acting on the crown wall	[N/m]
$F_{H,0.1\%}$	0.1% Horizontal force acting on the crown wall	[N/m]
$F_{V,0.1\%,FoS}$	0.1% Vertical force acting on the crown wall at the instance of failure	[N/m]

$F_{V,0.1\%}$	0.1% Vertical force acting on the crown wall	[N/m]
g	Gravitational acceleration	$[m/s^2]$
h	Water depth	[m]
H_s	Significant wave height	[m]
$H_{0.1\%}$	0.1% highest wave	[m]
i	Hydraulic gradient	[m/m]
k	Permeability	[m/s]
L_{0m}	Deep water wave length corresponding to T_m	[m]
L_{0p}	Deep water wave length corresponding to T_p	[m]
L_m	Length model	[m]
L_p	Length prototype	[m]
p_h	Hydrostatic pressure at crown wall face	$[N/m^2/m]$
p_m	Pressure at crown wall face due to wave impact	$[N/m^2/m]$
p_u	Uplift pressure at the crown wall base	$[N/m^2/m]$
R_c	Crown wall crest freeboard	[m]
$R_{0.1\%}$	0.1% Run-up height above SWL	[m]
R_U	Run-up height above SWL	[m]
s_{0p}	Wave steepness based on T_p	[-]
s_o	Maximum run-up level at the seaward edge of the armour	$[N/m^2/m]$
T_m	Average wave period	[s]
T_p	Peak wave period	[s]
u	Flow velocity	[m/s]
u_f	Filter velocity	[m/s]
v	viscosity	[-]
V_1, V_2	Volumes used in Pedersen	$[m^3/m]$
W^*_{crit}	Dimensionless critical weight	[kg/m]
x_c	Wetted length	[m]
x_u	length at loading moment that remains dry	[m]
y	Thickness run - up zone	[m]
y_{eff}	Effective height wave impact zone	[m]
$z_{2\%}$	Vertical 2% run-up distance calculated with Van Gents method	[m]

List of Figures

List of Tables

1

Introduction

Coastal ports must be ensured of calm water to enable vessels to safely enter/leave and moor in the port. Breakwaters are the primary coastal defense structures used to facilitate these conditions. They provide shelter from wave action origination from sea, subsequently creating calm conditions that are beneficial for port operations. Additionally, breakwaters protect beaches against erosion due to the calmer local conditions (wave climate & tide). A breakwater's construction requires large amounts of material, hence it can be highly expensive to build one. As a result, engineers and contractors are exploring ways to reduce the cost of breakwaters. Crown walls, mounted atop breakwaters, present one such solution, and will be the focus of this research.

1.1. Theoretical background

Before discussing the motivation, problem definition, and methodology of this research, it is necessary to first introduce the key concepts related to the topic. This section begins by defining what a crown wall is and briefly outlining its application in breakwater construction. Subsequently, the key failure mechanisms and stability considerations will be discussed, providing the necessary theoretical background to support the research objectives and approach.

Crown wall

Crown walls are placed on the crest of breakwaters. Among the various types of breakwaters, rubble mound breakwaters are the most commonly used in shallow water. Main advantage of a rubble mound breakwater is its high effectiveness at dissipating wave energy due to its rough surface and porous nature, which helps reduce wave reflection and scour at the toe of the structure. The multi-layer design further enhances their ability to absorb and dissipate wave energy efficiently. Due to their capacity to reduce wave reflection and dissipate wave energy, they are particularly beneficial for use in harbors. Additionally, compared to other breakwater types, their construction is relatively straightforward, as they do not require specialized construction techniques, machines, or materials. This makes them suitable for remote or less developed regions.

(a) Crown wall during construction **(b)** Crown wall **(c)** Crown wall during construction (St. Helena)

Figure 1.1: Real-world examples of crown walls

Bekker (2017) describes crown walls as *"a gravity based structure on top of a rubble mound breakwater which gains stability due to its own weight and friction between the base and contact surface of the rubble mound'*. These structures are often L-shaped and face the seaside. Crown walls serve several critical functions. Primarily, they increase the height of the breakwater and reduce wave overtopping in a cost-efficient manner. By doing so, crown walls decrease the total amount of material required for the construction of the breakwater. Additionally, they offer practical benefits, such as simplifying access to the breakwater for maintenance and operations. The advantages mentioned above, have been illustrated in Fig. 1.2, as outlined by CIRIA et al. (2007).

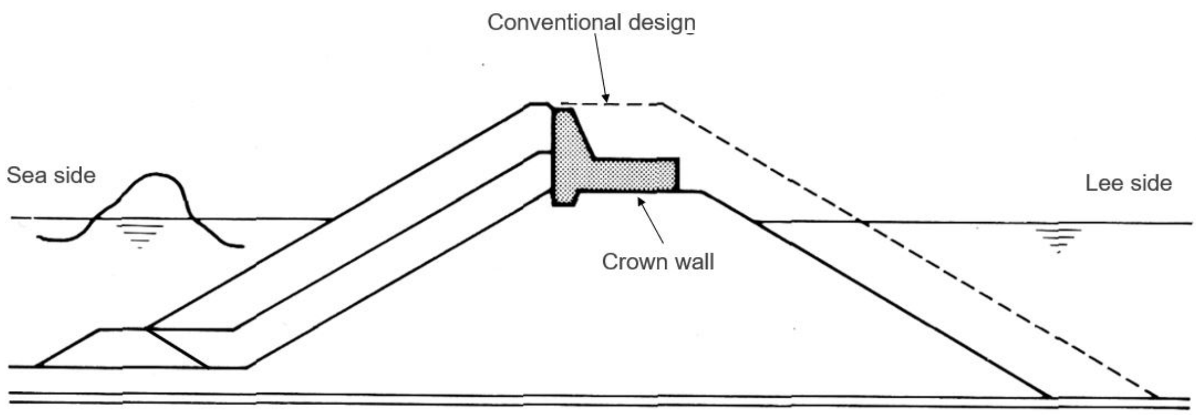

Figure 1.2: Crown wall benefits as illustrated in CIRIA et al. (2007)

Failure modes

When evaluating the stability of a coastal structure, and in this case a rubble mound breakwater with crown wall on top, all individual components are important for the total stability, since failure of one will lead to loss of function and failure of the whole structure. This also holds for crown walls, which is also confirmed by Pedersen (1996). To facilitate the design and stability calculations, various failure mechanisms have been investigated. According to CIRIA et al. (2007), there are four distinct failure mechanisms, which can be categorized into those depending on the strength of the superstructure (breakage) and those depending on the interaction with the underlying structure (sliding and overturning). All failure mechanisms are illustrated in Fig. 1.3. Additionally, Pedersen (1996) mentions that sliding is the most prevalent failure mechanism displayed by crown walls, which is why this study solely focused on the stability criterion of sliding.

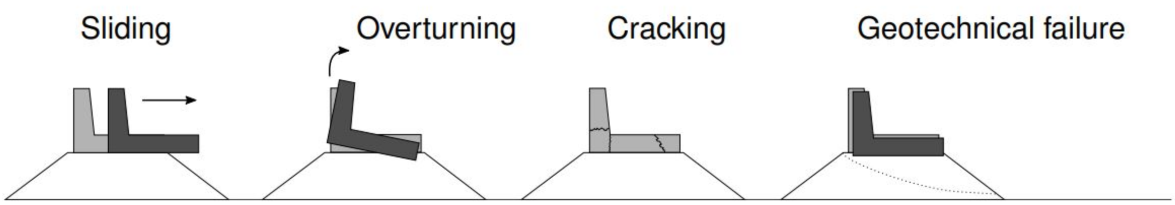

Figure 1.3: Different failure modes (Pedersen, 1996)

Stability

For crown walls without anchoring or key, stability is maintained if the resistance against sliding is larger than the horizontal wave load acting on the element. How this resistance against sliding is produced can be seen in Fig. 1.4, where a simplistic sketch is given of the present forces acting on the crown wall. Additionally, the stability criterion is give in Eq. (1.1) and the derivation of the Factor of safety Eq. (1.1), which will be used in the remainder of this study.

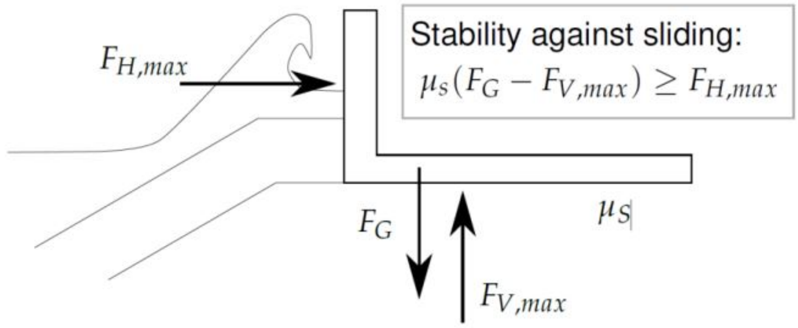

Figure 1.4: Simplified wave load analysis on a crown wall in the stability criterion (Bekker, 2017)

$$\mu_s(F_G - F_{V,\text{max}}) \geq F_{H,\text{max}} \tag{1.1}$$

$$\text{Factor of Safety} = \frac{\mu_s(F_G - F_{V,\text{max}})}{F_{H,\text{max}}} \tag{1.2}$$

Where:

μ_s	=	Coefficient of friction	(-)
F_G	=	Gravitational force	(N)
$F_{V,\text{max}}$	=	Maximum vertical force	(N)
$F_{H,\text{max}}$	=	Maximum horizontal force	(N)

As shown in Eq. (1.1), the stability is ensured when when the criterion is satisfied.

1.2. Motivation

While current design methods for crown walls may seem accurate, closer inspection reveals notable limitations. Model tests conducted by Molines et al. (2018) and a comparative analysis by Negro Valdecantos et al. (2013) highlight significant discrepancies in the estimation of wave forces on these structures. In many cases, the predicted forces did not align with the measured forces, resulting in inaccuracies that lead to overly conservative designs. Moreover, these discrepancies became more pronounced as certain parameters changed, indicating potential dependencies and further emphasizing the limitations of current methods. This highlights key areas for further research.

Veringa's research not only confirmed the mismatch between predicted and measured forces but also underscored a broader issue in the understanding of wave-structure interaction. The results suggest that the existing design methods do not fully capture the complexities of wave loading. Consequently, there is a compelling need for further research into the behavior of crown walls, not only from an academic perspective to improve theoretical knowledge but also from a practical standpoint to enhance the safety and cost-effectiveness of breakwater construction. By addressing these gaps in understanding, this study aims to refine design methods and provide more accurate predictions of wave forces, ultimately contributing to the advancement of coastal engineering practices.

1.3. Problem definition

As previously mentioned, existing design methods lack comprehensive understanding, resulting in significant differences in force estimations. After a thorough literature review, we identified several specific knowledge gaps that this study aims to address.

Before delving into the problem definition, it is important to elaborate several technical definitions that will help in understanding the following sections. Freeboard — zero or non-zero — refers to the vertical distance between the still water level and the base of the structure. This concept directly influences uplift pressures, the forces exerted upward by water along the base of the crown wall. To obtain the total uplift force, one should summarize the pressure acting over the whole base of the crown wall. Finally, permeability is a measure to describe how easily a fluid can move through the porous medium. Understanding these concepts is crucial for grasping the issues discussed in the following sections.

Uplift pressure distribution

Regarding the uplift pressures two situations can be distinguished: zero and non-zero base freeboard. The situation of non-zero freeboard is illustrated on Fig. 1.2, where the base of the crown wall is not equal to the water level (SWL). For zero freeboard, the assumption of triangular uplift distribution holds quite well, also confirmed by Veringa (2023) measurements (Fig. 1.5a). Contrarily, the opposite is observed in cases where the freeboard is non-zero (Veringa, 2023). After comparing the adapted uplift distribution by Bekker (2017), Fig. 1.5c, to the pressure measurements of Veringa (Fig. 1.5b), significant differences can be seen, which again proves the inadequate understanding for the situation. When further analyzing the point of maximum vertical pressure, Bekker states that it occurs at the seaward side of the base. However, this assumption lacks support from Veringa's measurements, which indicate a slightly more inward point. Additionally, in stability calculations for non-zero freeboard, hydrostatic pressure is assumed, which is not a valid assumption. This has also been confirmed by Veringa's measurements, that display different vertical and horizontal pressures acting on the crown wall corner. These are some examples, illustrating a still present knowledge gap.

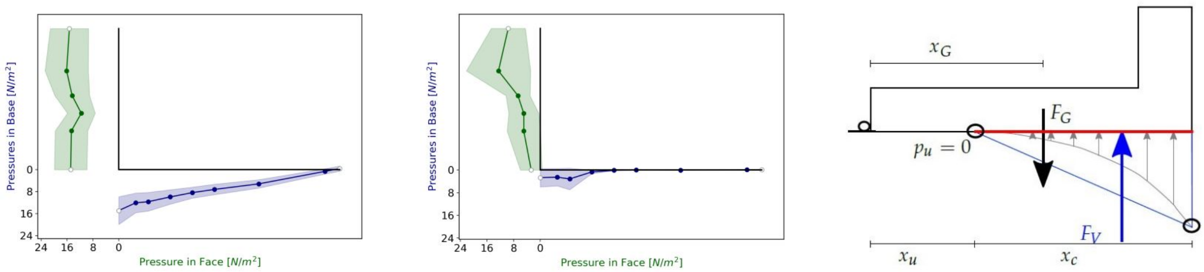

(a) Zero freeboard pressure measurement by Veringa (2023)

(b) Non-zero freeboard pressure measurement by Veringa (2023)

(c) Pressure distribution for non-zero freeboard Bekker (2017)

Figure 1.5: Difference between proposed and measured uplift pressure distribution

Permeability influence on uplift pressure

The literature review has highlighted the lack of substantial research on the impact of core permeability on uplift pressures. It is expected that the influence of core permeability will be significant, especially for larger freeboard scenarios. Martin et al. (1999) studied the effect of armour permeability on the resulting pressures on crown walls and Reedijk et al. (2009) and van der Meer (1988) studied the effect of core permeability on the armour layer stability, however neither, made any significant conclusions regarding the uplift pressures. The aforementioned points, make the research on the influence of core permeability interesting and highlight the current knowledge gap.

Horizontal pressure reduction

As highlighted by the literature review, currently there are only two methods available to determine the horizontal pressures on the sheltered face of the crown wall. The first method, derived by Pedersen (1996), assumes a 50% pressure reduction, as illustrated in Fig. 1.6a. The second method, developed by Martin, uses a λ-reduction factor, which is a function of the armour crest width and the wave length, Fig. 1.6b. Both methods however, assume a stepwise decrease in pressures, as Fig. 1.6 illustrates. The simplicity of this assumption appears inadequate. It is more reasonable that the reduction in pressure is proportional to the amount of armour in front of the wall. Hence, a gradual decrease over the height of the armour crest is expected, in stead of the stepwise reduction. This emphasizes the incomplete understanding of armour crest reduction, indicating the need for further research.

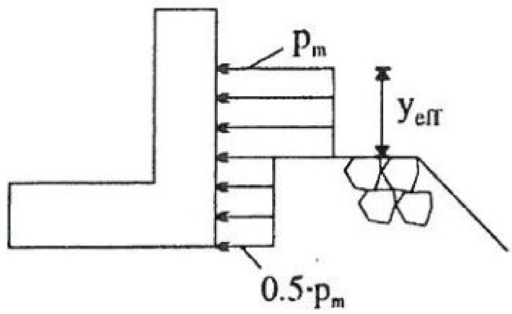

(a) Assumed 50% pressure reduction by Pedersen (1996)

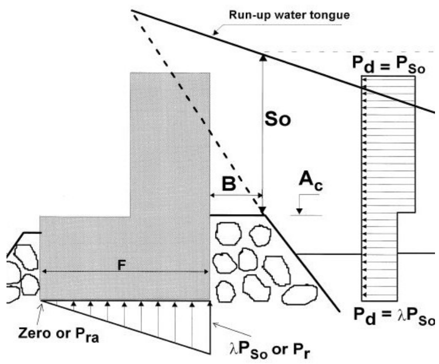

(b) λ-reduction factor by Martin et al. (1999)

Figure 1.6: Different methods to calculate pressures on the sheltered part of the crown wall

1.4. Research objective

The research objective of this research is to close all the aforementioned knowledge gaps. The data obtained from the physical model tests will help to generate a greater understanding of the permeability influence on the uplift pressure distribution. The research questions, given below, will help to fill the knowledge gap.

How do the vertical and horizontal pressure distributions on a crown wall develop?

To guide the research and help questioning the research question, multiple sub-questions have been derived, which can be seen below:

- How can uplift pressure distribution and force better be described?
- What is the impact of core permeability on the vertical and horizontal forces acting on a crown wall? Is stability of the crown wall influenced?
- How do the horizontal forces develop as a function of different armour layouts, and how does this impact overall stability?

Furthermore, it would be valuable to create a comprehensive dataset from the data obtained by the physical model tests. The data can be used for calibration and validation of CFD models (e.g. OpenFOAM). This, however, falls in the category 'nice to have' since answering the research question is the main objective of this research.

1.5. Research strategy

The research strategy adapted in this study consists of a literature research, small-scale tests and a thorough data analysis. Each component is a cornerstone in this research, as they are essential in answering the research question and will therefore be discussed in separate chapters. Below a short description of each research component is given, a more detailed description can be found in the corresponding chapter.

Literature research

First step of the study is to explore all available literature on the topic of research, in this case crown wall stability on top of a rubble mound breakwater. One should get familiar with all current knowledge regarding the topic before starting his research. After the literature research is conducted, a knowledge gap can be identified and the research objectives can be set-out. The literature research covers most of the influential methods for wave force estimations, to design crown walls on rubble mound breakwaters. The concepts used in the derivations will be discussed, followed by a short critical analysis and comparison of the methods, highlighting all shortcomings. Subsequently, the literature research gains a review of all available design methods and helps in identifying the knowledge gap.

Small-scale model tests

To study the research objective and gain valuable insights that help answering the research question, model tests will be performed. The wave flume in the Hydraulic Engineering Laboratory of the University of Delft is used to perform physical model tests. During the tests multiple parameters will be varied to investigate their influence on the stability of the crown wall. To acquire insights, pressure transducers are installed along both faces of the crown wall. The pressure transducers (Kulite's HKM-375M) are able to measure pressure changes due to differences in wave loading. Therefore, the small-scale model tests will yield extensive pressure records, which will be thoroughly analysed. Additionally, this study also uses cameras. The cameras is directed towards the side of the breakwater, providing a side view that shows the core. This arrangement allows us to monitor the evolution of the phreatic line within the breakwater core. Analysis of the videos will provide a visual representation of the temporal evolution of the phreatic line following wave impact. By visualizing the pressure wave and comparing it to the pressure records, we hope to gain valuable insights.

Data analysis

The final part of this study consists of the data analysis of the model measurements obtained. In this phase, the pressure measurements will be both validated and analyzed to generate pressure distributions along the crown wall faces. Following a comparison of these pressure records, conclusions can be drawn regarding the reduction in horizontal pressure and the influence of permeability on vertical pressures. Although video analysis was initially planned, it was ultimately not performed due to time constraints. With these insights, obtained from the pressure records, we aim to address the research question and fill existing knowledge gaps.

2

Literature research

This chapter explores various methods for calculating wave forces on crown walls. First, a method description is given, followed by a critical analysis to identify any knowledge gaps. Small-scale wave flume tests have been fundamental in the derivation of the methods, since the results have been used to derive empirical formulations for the estimations of wave forces. This chapter starts with the Iribarren and Nogales' method and progress with later developments.

2.1. Current crown wall design methods

Iribarren & Nogales, 1954

Iribarren and Nogales (1954) were pioneers in introducing a method for calculating wave forces on walls, notable for its simplicity. Their method was developed using a specific breakwater geometry and broken waves arriving at the breakwater. The method lacks consideration of various parameters, such as wave height and berm width. Additionally, their approach only accounts for horizontal pressures and neglects the uplift pressures, as is illustrated on Fig. 2.1.

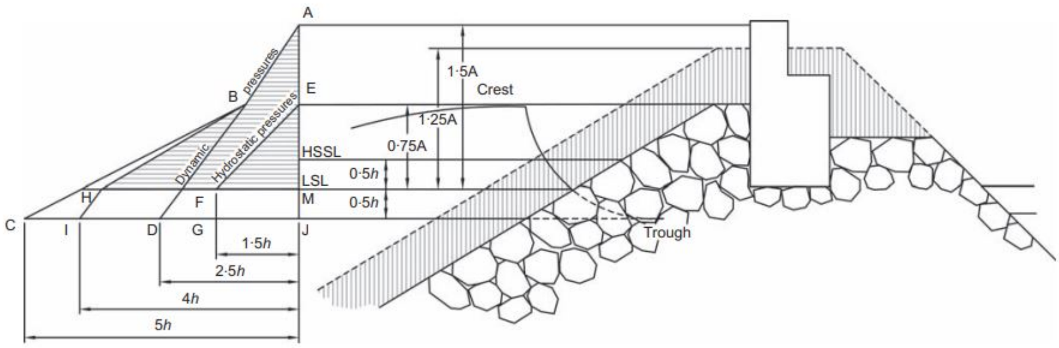

Figure 2.1: Pressure distributions proposed by Iribarren and nogales (Negro Valdecantos et al., 2013)

The authors were the first to assume that the presence of the armour crest reduces the pressures by 50%. The pressure on the wall is illustrated by ABD, Fig. 2.1, and the total pressure exerted on the wall is visualized by ABH, Fig. 2.1. Later (Martin et al., 1999) concluded that this method was too conservative. *Original paper/publication was not found: review is based on second hand papers*

Günback & Göcke, 1984

Günback and Göcke (1984) developed their method to estimate wave forces based on wave run-up. The total wave pressure distribution is divided into two parts. Firstly, they introduced the concept of virtual run-up, which represents the run-up that would occur on an infinitely sloped surface (Fig. 2.2a), resulting in a hydrostatic pressure on the wall. Secondly, they determined the impact pressure due to wave impact. Both distributions are illustrated in Fig. 2.2b, and their summation yields the total pressure distribution. The authors were the first to consider an uplift force on the crown wall. They assumed a triangular distribution, starting from the hydrostatic pressure assumption at the face and decreasing to zero at the crown wall heel(Fig. 2.2b).

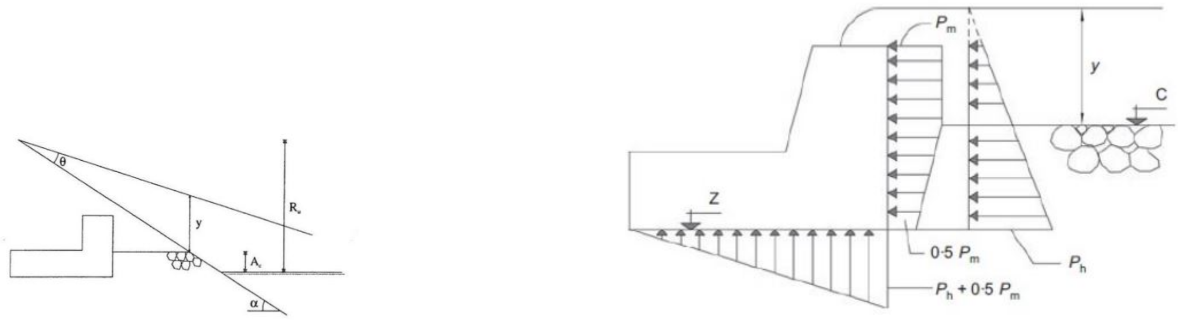

(a) Virtual run-up

(b) Pressure diagrams by Günback & Göcke method

Figure 2.2: Parameters and assumptions outlined by Günback & Göcke method (Pedersen, 1996)

The hydrostatic pressure (P_h) can be computed with the run-up (R_U) and the length over which it acts (y), the formulation is illustrated below.

$$P_h = \gamma_w y \tag{2.1}$$

$$y = \frac{R_U - A_c}{\sin\alpha} \frac{\sin\theta}{\cos(\alpha - \theta)} \tag{2.2}$$

$$R_U = \begin{cases} 0.4H & \text{if } \xi_m < 2.5 \\ H & \text{if } \xi_m > 2.5 \end{cases} \tag{2.3}$$

The impact pressure (P_m) could be described as:

$$P_m = \frac{\gamma_w(\sqrt{g \cdot y})^2}{2} = \frac{\gamma_w \cdot y}{2} \tag{2.4}$$

The method of Günback and Göcke has several limitations, which are summarized briefly hereafter. Firstly, the method lacks clarity as it remains unclear which wave height is used in Eq. (2.3). Additionally, the range of applicability is not specified, which is crucial for determining the method's usage. Lastly, for the impact pressures at the protected part of the wall, a reduction factor of 0.5 is assumed. However, this factor should be a function of the breakwater armour parameters (crest width, permeability, and height), a concept later validated by (Martin et al., 1999; Veringa, 2023).

Martin, 1999

Martin et al. (1999) developed a semi-empirical approach for estimating wave forces on crown walls after identifying limitations in prior methods. According to Martin, the method of (Iribarren & Nogales, 1954) was overly conservative, while the method of (Günback & Göcke, 1984) were too challenging to apply. To address these shortcomings, Martin conducted model tests, varying parameters such as the width of the armor crest and armor size, primarily under regular wave conditions.

Martin's methods distinguishes two types of pressures: the *dynamic* pressure (P_d) and the *reflective* pressure (P_r), as illustrated in Fig. 2.3. The dynamic pressure has separate values for the protected and unprotected parts of the wall. Beneficial of Martin's methods is that he distinguishes different loading combinations, treating each pressure type individually. This approach provides greater insights into the stability of a crown wall.

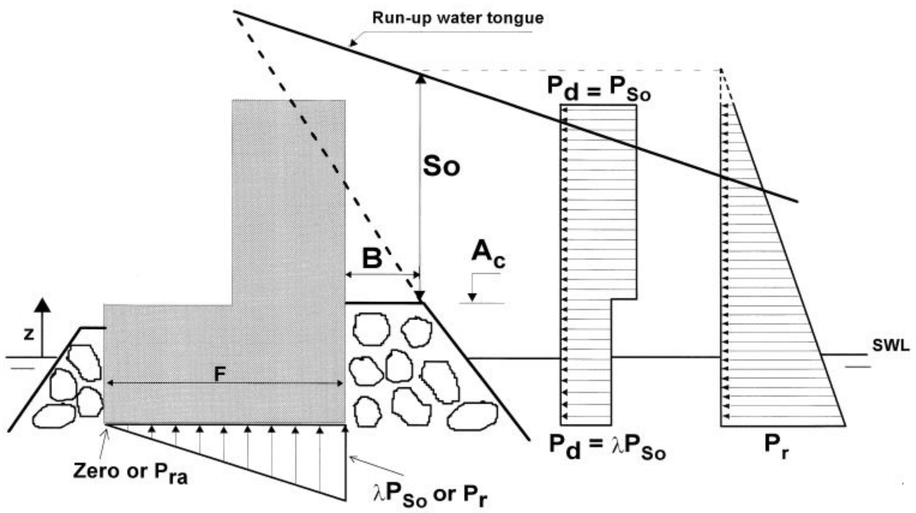

Figure 2.3: Pressure distributions proposed by (Martin et al., 1999)

The dynamic pressure, resulting from the impact of the wave, for the unprotected part can be calculated using the following three equations:

$$\begin{aligned} p_i(z) = p_{so} &= c_{wl}\rho_{wl} g S_0, \\ S_0 &= H(1-\frac{R_{ca}}{R_u}), \\ c_{wl} &= 2.9(\frac{R_u}{H}\cos\alpha)^{-2}. \end{aligned} \tag{2.5}$$

Martin used the empirical relation derived by (Losada & Giménez-Curto, 1980), who have formulated the run-up on an infinite slope with monochromatic waves of normal incidence.

$$\frac{R_u}{H} = A_u(1-e^{B_u \cdot \xi_m}) \tag{2.6}$$

For the pressures on the protected part, Martin created an empirical reduction factor (λ) that can be applied on the pressure of the protected part (P_{so}), illustrated on Fig. 2.3. The reduction factor can be computed with Eq. (2.7):

$$\lambda = 0.8e^{-10.9\frac{B_a}{L}} \tag{2.7}$$

Likewise, the reflective pressure is derived as follows:

$$\begin{aligned} p_p &= \mu\rho_{wl} g(S_0 + R_{ca} - z), \\ \mu &= a \cdot e^{c(\frac{H}{L}-b)^2}. \end{aligned} \tag{2.8}$$

The factors a, b and c represent non-dimensional factors and are a function of the non-dimensional berm width (B/L_e). μ is a reduction factor for the number of armour units in the crest. Ultimately, the uplift pressure is derived with Eq. (2.9). Contrarily to other methods, the pressure at the heel isn't assumed to be zero, therefore it can have a minimum value at the rear (p_{re}).

$$\begin{aligned} p_{re} &= p_p, \\ p_{ra} &= \frac{B_c}{L_p} p_{re}. \end{aligned} \tag{2.9}$$

As is illustrated, Martin's method is more inclusive than previous methods, due to the inclusion of different crest parameters. The distinct separation of dynamic wave pressure from reflective (quasi-hydrostatic) pressure is a significant strength, as it accurately represents the physical processes at play. However, (Negro Valdecantos et al., 2013) lists some important critique. Firstly, the method relies on regular waves which do not reflect real-world design conditions. Additionally, the method is validated on an atypical breakwater. Besides, the method does not specify which wave height was used in the tests, therefore the users of the method have to make educated guesses, on which wave height to use.

Pedersen, 1996

The current approach most commonly used is developed by Pedersen. He formulated his method through extensive physical model experiments, adjusting various breakwater parameters such as crown wall height, crest berm width, and slope. He confirmed that impact pressures are dominant in the wave forces, a notion which seemed obvious but needed empirical validation. Vertical forces were assumed to be linear and approximated by the hydrostatic assumption at the toe of the wall, gradually decreasing to zero at the end of the underside; however, these forces were not directly measured in the research.

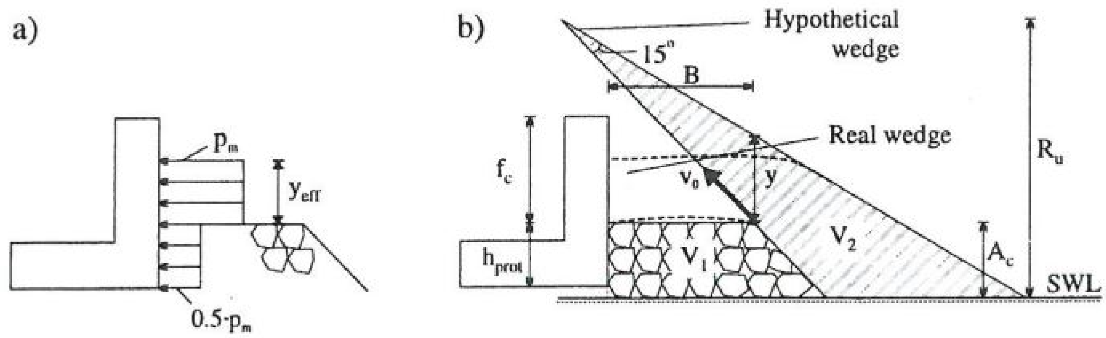

Figure 2.4: a) Proposed pressure distribution on crown wall (Pedersen, 1996), and b) Run-up wedge and design parameters (Pedersen, 1996)

In Pedersen's method, the impact pressure is a function of the run-up and can be estimated with Eq. (2.10), visualized in Fig. 2.4. For the run-up calculations Pedersen used the method developed by (van der Meer & Stam, 1992), (Eq. (2.11)).

$$p_m = g\rho_w(R_{u,0.1\%} - A_c) \tag{2.10}$$

$$\frac{R_{u,0.1\%}}{H_s} = \begin{cases} 1.12\xi_m & \text{if } \xi_m \leq 1.5 \\ 1.34\xi_m^{0.55} & \text{if } \xi_m > 1.5 \end{cases} \tag{2.11}$$

Regarding the horizontal force on the protected part, Pedersen assumes a constant reduction factor of 0.5, independent on the height. As illustrated in Fig. 2.4 he used a hypothetical and vertical run-up wedge, to determine the incoming wave energy. The thickness of the hypothetical run-up can be derived via Eq. (2.12). The real wedge determines the run-up that pertains to the structure and has a thickness(Eq. (2.13).

$$y = \frac{(R_{u,0.1\%} - A_c)}{\sin\alpha} \cdot \frac{\sin(15°)}{\cos(\alpha - 15°)} \tag{2.12}$$

$$y_{eff} = \min(\frac{y}{2}, d_{ca}) \tag{2.13}$$

The force generated by a 0.1% wave is determined by the formula below:

$$F_{H,0.1\%} = 0.21\sqrt{\frac{L_{0m}}{B_a}}(1.6p_m y_{eff} + V\frac{p_m d_{c,prot}}{2}) \tag{2.14}$$

Additionally, Pedersen advises to only use the equations within the parameters ranges given in Table 2.1. Where H_s is obtained from the time signal of the surface elevation.

Parameter	Range
ξ_m	1.1 - 4.2
H_s/A_c	0.5 - 1.5
R_c/A_c	1 - 2.6
A_c/B	0.3 - 1.1
$cot\alpha$	1.5 - 3.5

Table 2.1: Range of applicability of the Pederson method (Pedersen, 1996)

Pedersen's method is build upon extensive model tests with numerous waves for each test, resulting in a substantial dataset. His research systematically explores various parameters. Furthermore, seen in Table 2.1, he was the first researcher to provide an application range in which his method could be used safely. Also, he clearly defined all the parameters involved. Already touched upon in the method description, Pedersen does not thoroughly discuss uplift pressures, but, assumes a triangular uplift pressure distribution for both zero and non-zero base freeboard of a crown wall. This is an impactfull assumption, therefore, this remains the main point of critics for his method. He does mention the reasoning behind this method, as according to him measuring these pressures is impossible due to strong scaling effects. Pedersen does acknowledge that his method for addressing uplift tends to produce conservative estimates, which is a consequence of his triangular pressure assumption.

Nørgaard, 2013

Originating from the same university as Pedersen, (Nørgaard et al., 2013) introduced an extension to the method of Pedersen. Model tests performed by Nøgaard confirmed that Pedersen's semi-empirical formulae overpredict the loads in shallow water wave conditions. Therefore, based on 162 physical small-scale model tests, he presented a modification to include both deep and shallow water wave conditions. The modification is made by altering wave run-up term and using $H_{0.1\%}$ instead of H_s. The result of these modifications are seen below:

$$R_{u,0.1\%} = \begin{cases} 0.603 \cdot H_{0.1\%}\xi_m & \text{if } \xi_m \leq 1.5 \\ 0.722 \cdot H_{0.1\%}\xi_m^{0.55} & \text{if } \xi_m > 1.5 \end{cases} \tag{2.15}$$

During his research Nøgaard noticed that the sensors Pedersen used were influenced by dynamic amplifications. To account for this phenomenon, he adjusted a factor in the force estimation formula of Pedersen, Eq. (2.16), from 1.6 to 1. Therefore, the formula becomes:

$$F_{H,0.1\%} = 0.21\sqrt{\frac{L_{0m}}{B_a}}(p_m y_{eff} + V\frac{p_m d_{c,prot}}{2}) \tag{2.16}$$

In his model tests Nøgaard varied the ratio of armour height to crown wall height. Therefore, the horizontal attack point on the crown wall face differs compared to the Pedersen method. The adaptation for the overturning moment are illustrated below.

$$M_{H,0.1\%,mod.} = (h_{prot} + \frac{1}{2}y_{eff}e_2)F_{Hu,0.1\%} + \frac{1}{2}h_{prot}F_{Hl,0.1\%}e1 \tag{2.17}$$

With:

$$\begin{aligned} F_{Hu,0.1\%} &= 0.21\sqrt{\frac{L_{0m}}{B}}p_m y_{eff} \\ F_{Hl,0.1\%} &= 0.5 \cdot 0.21\sqrt{\frac{L_{0m}}{B}}p_m V d_{c,prot} \\ e_1 &= 0.95 \text{and} e_2 = 0.4 \end{aligned} \tag{2.18}$$

The benefit of this extension is that it increases the range of application to shallow water conditions. Just like Pedersen, Nørgaard also gives a range of application. Herein, Nørgaard differentiates between a fully protected crown wall face ($d_{ca} = 0$) and unprotected wall face ($d_{ca} > 0$). Additionally, it is important to mention that the H_s in Section 2.1 is derived from the time signal of the surface elevation.

Parameter	$d_{ca} = 0$	$d_{ca} > 0$
ξ_m	2.3 - 4.9	3.31 - 4.64
H_s/A_c	0.51 - 1.63	0.52 - 1.41
R_c/A_c	0.71 - 1	1 - 1.7
H_{m0}/h	0.19 - 0.55	0.19 - 0.55
H_{m0}/L_{m0}	0.018 - 0.073	0.02 - 0.041

Table 2.2: Range of applicability of the Nøgaard adaptation (Nørgaard et al., 2013)

Nørgaard's adaptations are regarded as insightfull and significant, as it extends the range of applicability for Pedersens method. Regarding the uplift, Nørgaard did measure vertical pressures, however, no modifications on the vertical pressure distribution were proposed. A time lag between the maximum uplift pressure and the maximum horizontal pressure is recorded, and excluding this from the calculations would result in a conservative estimation (Nørgaard et al., 2013). Small criticisms, is that the method is not provide accurate estimates for long waves. Therefore, this method is not suitable to use in swell-wave conditions.

Bekker, 2017 & 2018

Subsequent to Nørgaard's work, (Bekker, 2017) conducted physical model tests in which he specifically focused on the uplift pressures and the time lag between the dynamic and reflecting impact. One of the results of Bekker's research was a set of equations to calculate the dimensionless critical mass. The set of equations, Eqs. (2.19) and (2.20), can be used for swell ($s_{op} = 0.04$) and storm ($s_{op} = 0.01$) waves and H_s or $H_{0.1\%}$.

$$W^*_{crit,swell} = \begin{cases} 0.83\frac{H_s^2}{R_{ca}^2} + 0.03, & \text{if } 0.5 \leq H_s^2/R_{ca}^2 \leq 2.2 \\ 0.25\frac{H_{0.1\%}^2}{R_{ca}^2} + 0.18, & \text{if } 1.0 \leq H_{0.1\%}^2/R_{ca}^2 \leq 6.6 \end{cases} \tag{2.19}$$

$$W^*_{crit,storm} = \begin{cases} 0.62\frac{H_s^2}{R_{ca}^2} - 0.23, & \text{if } 0.5 \leq H_s^2/R_{ca}^2 \leq 2.2 \\ 0.21\frac{H_{0.1\%}^2}{R_{ca}^2} - 0.19, & \text{if } 1.0 \leq H_{0.1\%}^2/R_{ca}^2 \leq 6.6 \end{cases} \tag{2.20}$$

Additionally, he defined his dimensionless mass as follows:

$$W^*_{crit} = \frac{W_{crit}}{\mu_s \rho_w g B_c d_c} \tag{2.21}$$

Furthermore, Bekker proposed a reduction factor for the uplift pressure, that can be applied on Nørgaards modification. According to (Bekker, 2017), the reduction factor depends on the effective length (x_c, illustrated in Fig. 2.5a), or known as 'wetted length', which decreases as the crown wall base freeboard increases. The resulting reduction factor can be determined as follows: $\gamma_v = x_c/B_c$. Since, this method only allows for visual measurements of the effective length, Bekker composed 6 equations to calculate this reduction factor.

$$\gamma_{crit,swell} = \begin{cases} 0 & \text{if } H_s/R_{ca} \leq 0.64 \\ 2.41\frac{H_s}{R_{ca}} - 1.54 & \text{if } 0.64 \leq H_s/R_{ca} \leq 1.05 \\ 1 & \text{if } H_s/R_{ca} > 1.05 \end{cases} \tag{2.22}$$

$$\gamma_{crit,storm} = \begin{cases} 0 & \text{if } H_s/R_{ca} \leq 0.75 \\ 2.41\frac{H_s}{R_{ca}} - 1.54 & \text{if } 0.75 \leq H_s/R_{ca} \leq 1.34 \\ 1 & \text{if } H_s/R_{ca} > 1.34 \end{cases} \tag{2.23}$$

With the results of his model tests, (Bekker et al., 2018) also proposed some modifications to the current assumed uplift pressure, Fig. 2.5b. He found that the shape of the distribution is rather S-shaped in stead of triangular (red pressure distribution in Fig. 2.5b) and that the length, over which the force acts, depends on the wave height and freeboard.

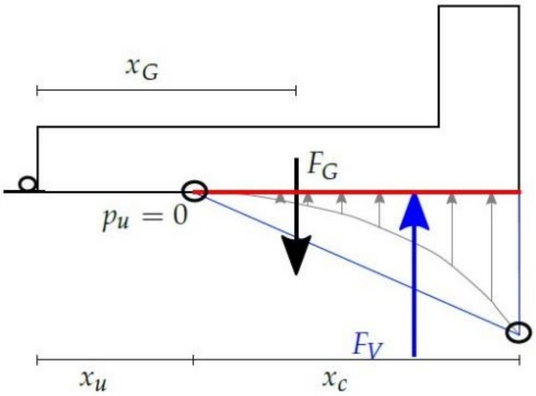

(a) Pressure diagram by Bekker (Bekker, 2017)

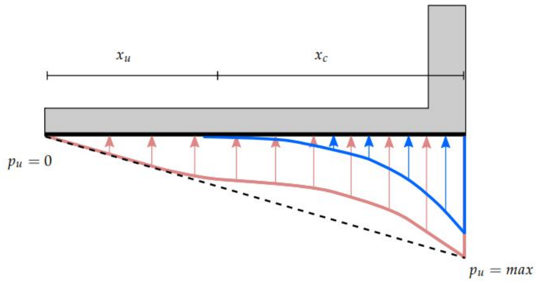

(b) Adapted uplift pressure distribution (Bekker et al., 2018)

Figure 2.5: Adaptions proposed by Bekker (Bekker, 2017; Bekker et al., 2018)

The range of applicability of the Bekker's reduction factor can be seen in Table 2.3.

Parameter	Range
H_s/A_c	0.71 - 1.48
H_s/L_{0p}	0.01 & 0.04
B_a/d_a	1.88
d_c/d_a	1.88
$d_{50,c}/d_{50,a}$	0.4
$(d_{85}/d_{15})_c$	1.39
$(d_{85}/d_{15})_a$	1.45
$cot\alpha$	2

Table 2.3: Range of applicability of the Bekkers adaptations (Bekker, 2017)

The concept Bekker introduces of improving the contact surface, instead of assuming that the uplift pressure is exerted over the total length, seemed quite promising, since it yields positive results. This was confirmed after both Bekker's own tests and the modifications made to Pedersen's and Nørgaard's methods, which resulted in more accurate wave force estimations. The method of determining this contact surface, namely through visual inspection received considerable critiques. Which he obviously acknowledges. Besides, Bekker comprehensively addressed the difficulties he encountered during his data collection and analysis. The problem primarily arose due to the fact that the pressure sensors were prone to capturing noisy signals. Heavy filtering was applied to mitigate this, which could have significantly impacted the conclusions drawn from the dataset.

Molines, 2018

All discussed methods exhibit a considerable resemblance in their approach to measuring wave forces on crown walls, they all use a type of run - up, either virtual run - up or another version. Nevertheless, Molines et al. (2018) introduces a markedly distinct methodology, by using the wave overtopping as a 'primary factor' to estimate wave forces, since measuring overtopping is relatively easy in scale tests, whereas virtual run-up cannot be measured. Molines did not conduct his own tests; instead, he utilized the tests conducted by Pedersen and other researchers, reanalyzing them with the help of a neural network. With the help of this tool he was able to identify a set of new parameters, with a particular focus on overtopping, to calculate wave forces of crown wall.

Moreover, he is one of the first to develop a separate formula for uplift pressure based on data, rather than relying on an assumed pressure distribution. For the horizontal forces, he developed two different formulas: a short formula and a long one, which is able to estimate the horizontal force more accurate. Similarly, he proposed two different formulas for the uplift pressure ($Pb_{0.1\%}$): a shorter, simpler version and a longer, more accurate one. Additionally, he provided a formula to calculate the maximum uplift force when the maximum horizontal forces occur $PbF_{0.1\%}$.

$$\begin{aligned} \frac{Fh_{0.1\%}}{0.5\rho g C_h^2} &= 3.6 + 0.6 \log Q \\ \frac{Fh_{0.1\%}}{0.5\rho g C_h^2} &= \left(0.23 + (\log Q + 6)\left(0.27 \ln(\zeta_{op}) + 0.1\right)\left(0.5\frac{R_c - A_c}{C_h} + 1\right) - 0.15\right) \end{aligned} \tag{2.24}$$

$$\begin{aligned} \frac{Pb_{0.1\%}}{0.5\rho g C_h} &= 4.3 + 0.52 \log Q \\ \frac{Pb_{0.1\%}}{0.5\rho g C_h} &= 0.9 + \left(0.4\frac{R_c - A_c}{C_h} + 0.6\right)(\log Q + 6) \\ \frac{PbF_{0.1\%}}{0.5\rho g C_h} &= 0.02\left(\frac{F_c}{L_{0p}}\right)^{-1/2} \end{aligned} \tag{2.25}$$

Additionally, he provides the parameter ranges within which this method can be applied.

Parameter	**Range**
$R_c/(\gamma_f H_{m0})$	1.67 - 6.55
ξ_m	1.39 - 7.77
$\gamma_f R_{u,0.1\%}/R_c$	0.36 - 1.41
$(R_c - A_c)/C_h$	0.0 - 0.59
$log(Q)$	-6.0 - -2.78
F_c/L_{0p}	0 - 0.03

Table 2.4: Range of validity of the method derived by Molines et al. (2018)

Molines revised his method for estimating wave forces a few times after it was first published, where a new wave overtopping estimator forms the basis of the wave force estimators. Furthermore, this newly formed estimator was compared with the CLASH project, that had been tested by van Gent et al. (2007). Even though the new estimator performs well, the main goal of the study seems to be creating a more understandable equation in order to reduce the intricate physics underpinning overtopping events. Molines' use of a neural network has drawn a lot of criticism because of its intrinsic ”black-box” nature, which raises questions regarding interpretability and transparency. Neural networks are capable of producing results with high accuracy, but they frequently do so without offering precise explanations for their assumptions, making it difficult to understand how particular inputs and outputs relate to one another.

Furthermore, Molines et al. (2018) claims that his formulations are simpler than current techniques. However, it is clear from a closer look of the design techniques covered in this part that the formulation includes the variable Q, which stands for overtopping discharge. In the event that this data is not accessible, estimation using the intricate formulations created by CLASH is required.

Apart from these discoveries, the underlying physical idea has a flaw. The phrasing seems to imply a relation that is paradoxical. In particular, although considerable overtopping due to a smaller crown wall could result in limited forces on the structure, this dynamic is not sufficiently reflected in the existing formulation. If one were to imagine an indefinitely high wall, the concept suggests that there would be no overtopping, and consequently, no forces would act on the crown wall. This is counterintuitive since it suggests that wave forces on crown walls cannot be accurately predicted using overtopping as a main predictor. This shows that when estimating the forces acting on these structures, overtopping alone might not be the best component to consider. Nevertheless, within specific (limited) ranges, the method by Molines et al. (2018) may provide reasonable results.

Veringa, 2023

Veringa (2023) continued Bekker's work, by using physical model tests. Acknowledgeding the still present knowledge gap regarding the uplift pressure, giving special attention on this topic and the time delay between both the horizontal and vertical maximum pressures. The innovative aspects of this research was the usage of twelve shock proof pressure sensors along the crown wall face and base. Veringa varied wave height (H_s), steepness (s), foundation level ($F_c\ H_s$), armour crest width ($G_c\ d_{a,n50}$) and crown wall height ($h_c\ H_s$), and researched their influence on wave loading.

From the results it was concluded that the assumed triangular pressure distribution is accurate but incomplete. The shape of the pressure distribution differs for non-zero foundation levels. The study also measured a relative time lag ($\Delta t\ T_p$) between horizontal and vertical maximum pressures in the range of 0 - 0.2 [-]. Veringa states that, if present, the time delay must be included in stability considerations for non-zero base freeboard. The reduction factor Veringa introduces to account for this phenomena, derived as a correction to the method proposed by Pedersen (1996), is shown below:

$$\gamma_t = \frac{F_{V,0.1\%,FoS}}{F_{V,0.1\%,max}} = 1.52\frac{F_c}{H_s} + 1.0 \tag{2.26}$$

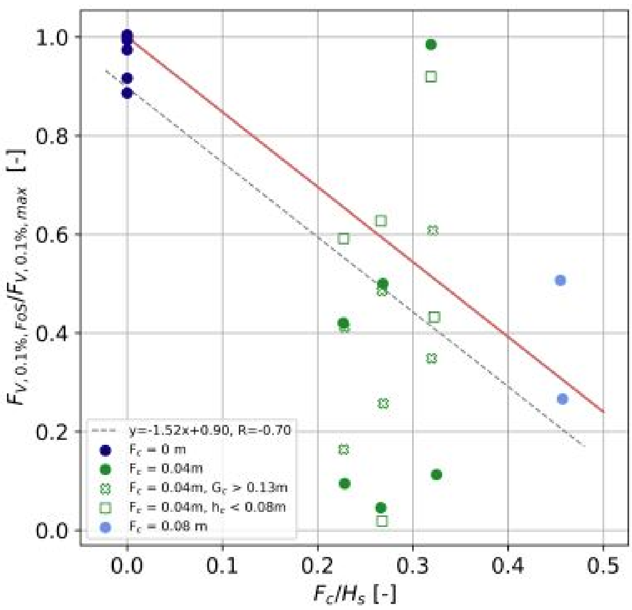

Figure 2.6: Graph by Veringa illustrating the correction factor for time lag, increasing with higher freeboard levels.

Additionally, he obtain pressure measurements in time, that neatly display the temporal evolution of the pressure distributions on the crown wall, Fig. 2.7.

Veringa identified a knowledge gap concerning the distribution of uplift pressure. A significant finding of his research was that for non-zero freeboard situations, the maximum uplift pressure is not located at the most seaward part of the crown wall base but slightly inward. Acknowledging potential criticisms, he noted that water depth variations were recorded along the flume, likely due to the structure's weight. Special adjustments were necessary to minimize this effect. Another point is that he did not use an active reflection compensation (ARC), which could potentially affect the pressure measurements. The most critical concern relates to the pressure sensor signal. Similar to Bekker's study, extensive filtering was applied to the measurements, but there's no way to confirm its accuracy. Moreover, the filter's effectiveness is reduced in cases of very closely spaced wave groups or when a wave is rapidly succeeded by another without a "zero" value in between.

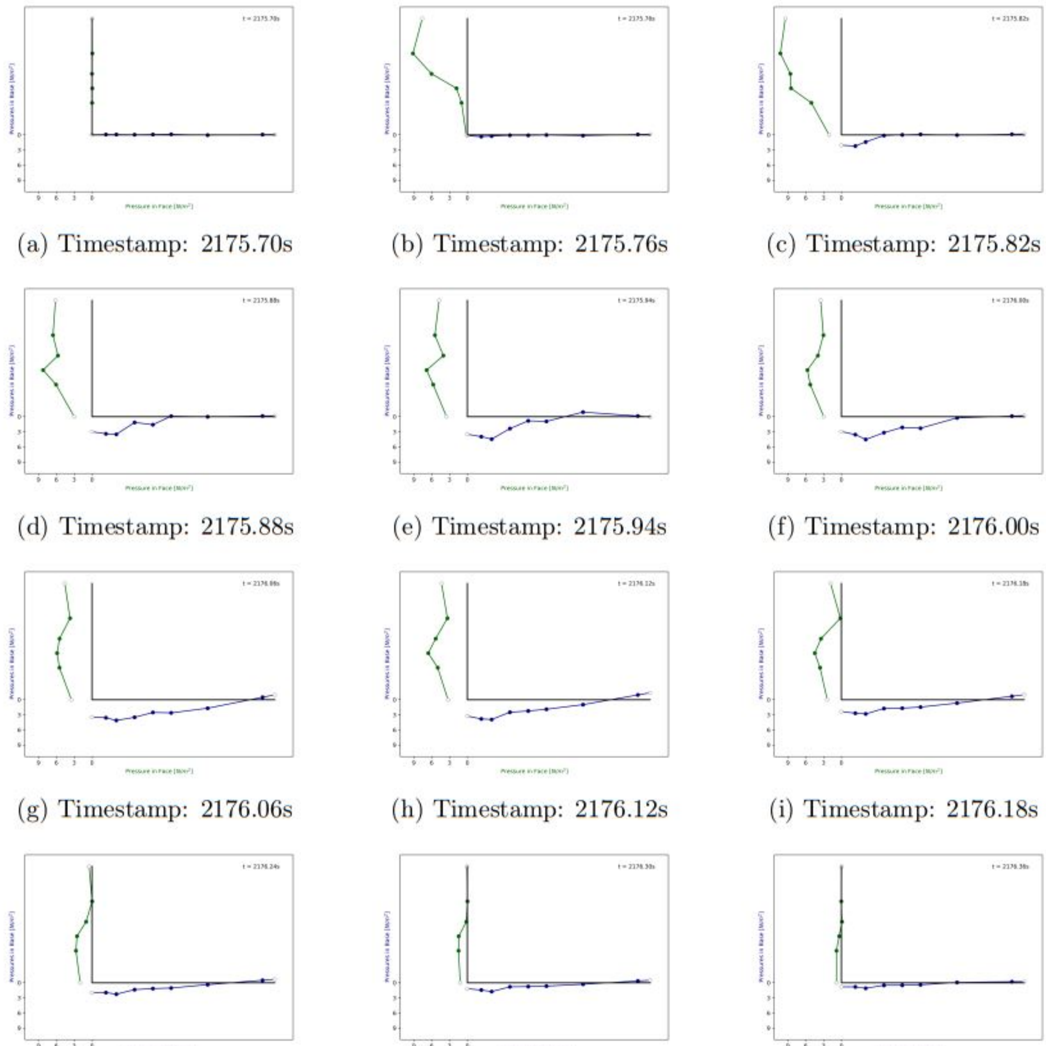

(a) Timestamp: 2175.70s (b) Timestamp: 2175.76s (c) Timestamp: 2175.82s

(d) Timestamp: 2175.88s (e) Timestamp: 2175.94s (f) Timestamp: 2176.00s

(g) Timestamp: 2176.06s (h) Timestamp: 2176.12s (i) Timestamp: 2176.18s

(j) Timestamp: 2176.24s (k) Timestamp: 2176.30s (l) Timestamp: 2176.36s

Figure 2.7: Pressure distributions on a crown wall (Veringa, 2023)

Van Gent, 2022

van Gent and van der Werf (2019) is the most recent researcher to publish work on the effects of oblique waves on coastal structures. In his study, he investigates how oblique waves impact the forces exerted on crown walls, alongside wave overtopping, though the latter will not be focused on. He highlights the limitations of existing methods, particularly their focus on perpendicular waves, and addresses these shortcomings by conducting comprehensive model tests. These tests vary wave heights, wave periods, and water levels, with the primary objective of measuring the horizontal and vertical forces acting on the crest wall.

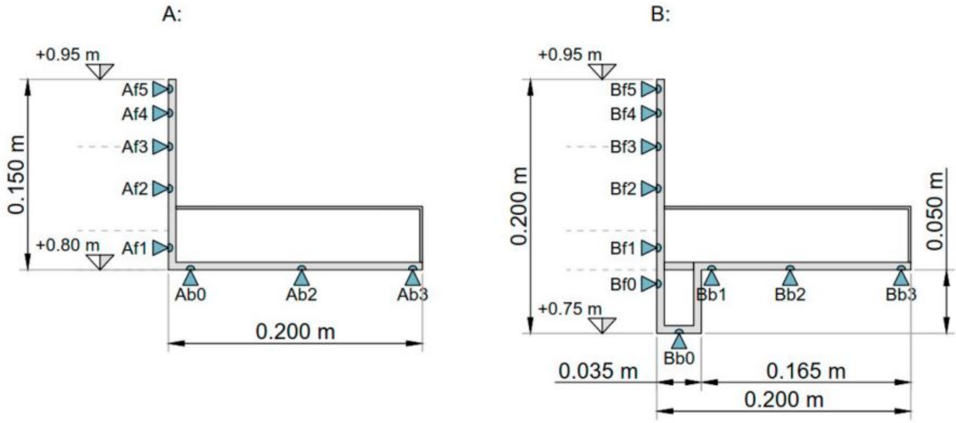

Figure 2.8: Sketch illustrating the different crown wall configurations tested by van Gent and van der Werf (2019)

A novel aspect of Van Gent's research is the testing of two different crest wall configurations: a crown wall with and without a key, as shown in Fig. 2.8. Additionally, by using different water depths, he incorporates the effect of base freeboard (F_b) in his tests. This analysis will focus exclusively on the methods he presents for predicting forces.

The tests illustrate a significant effect of oblique waves, where perpendicular waves result in the highest forces and show a reduction if the wave incidence angle increases. This underscores the importance of accounting for this effect in analyses. The paper present a new method to determine the virtual runup, which include the effect of oblique waves, shown as the γ factor in Eq. (2.27).

$$\begin{cases} \frac{z_{2\%}}{\gamma H_s} = c_0 \xi_{m,-1} & \text{for } \xi_{m,-1} \leq p \\ \frac{z_{2\%}}{\gamma H_s} = c_1 - \frac{c_2}{\xi_{m,-1}} & \text{for } \xi_{m,-1} \geq p \end{cases} \tag{2.27}$$

The adjusted run-up predictor is included in the new estimation methods predict the horizontal forces (Eq. (2.28)) and vertical forces (Eq. (2.29)), show below.

$$\begin{aligned} F_{H,2\%} &= c_{F,H}\, \rho g H_{\text{wall}} \left(z_{2\%} - A_c \right) \\ F_{H,0.1\%} &= 1.6 F_{H,2\%} \end{aligned} \tag{2.28}$$

The method developed to estimate the vertical force, shown below, includes the impact of a non-zero freeboard. Additionally, the influence of different crest wall configurations is also included in **??**, by the factors $C_{F,V}$.

$$\begin{aligned} F_{V,2\%} &= c_{F,V} \rho g B_{\text{wall}} \left(z_{2\%} - \gamma_A A_c \right) \left(1 - \left(\frac{F_b}{A_c} \right) \right)^{c_{F,b}} \\ F_{V,0.1\%} &= (2.88 - 32 s_{op}) F_{V,2\%} \end{aligned} \tag{2.29}$$

The test results show that for a crest wall with a key, the horizontal forces on the crest wall increase proportionally with the ratio of the crest wall height between configurations with and without the key.

However, the vertical uplift forces are reduced to 75% of those observed for a crest wall without a key. This is an interesting and unexpected outcome, as one might intuitively expect that the addition of a key, which is designed to enhance stability, would influence both the horizontal and vertical forces in a similar manner. The ranges of validity for these findings are also provided in the paper.

Parameter	**Range**
R_c/A_c	1.27 - 1.55
$(R_c - A_c)/H_s$	0.26 - 0.77
R_c/H_s	0.79 - 2.18
F_b/H_s	0 - 0.62

Table 2.5: Range of validity of the van Gents method (van Gent & van der Werf, 2019)

2.2. Conclusions of literature research

As seen, over the years, an increasing number of methods have been proposed for calculating wave forces on wave walls. Although this is a complex area of study, we observe an improvement in accuracy. However, a significant disparity still exists between horizontal and vertical forces, with horizontal forces being better understood compared to vertical forces (Molines et al., 2018). The uplift forces can be subdivided into two categories, namely: zero and non-zero freeboard. In particular, in non-zero freeboard situations, our understanding is limited, as uplift pressures are significantly lower in such cases. To conclude, we understand that freeboard reduces the magnitude of the uplift forces and their distributions, but we are uncertain on how it influences them. Moreover, similar observations can be made regarding the influence of permeability on vertical pressures and the presence of a crest on horizontal forces. It is self-evident that both must have an influence, but the exact extent remains unclear.

Part I

Scale model

3

Physical model set-up

To address the research questions outlined in Section 1.4 and gain a deeper understanding of the topic, a physical model was employed. This chapter begins by discussing all the relevant parameters considered when designing a crown wall, providing the necessary context for the study. Following this, the details of the physical model used in the research will be thoroughly explained. Additionally, the test conditions will be presented.

3.1. Physical and Hydraulic parameters

To design coastal structures numerous factors have to be accounted for, since the design of such structures, of which crown walls are an example, depends on multiple parameters. These different parameters, can be categorized into two groups, factors related the geometric conditions (physical parameters) and wave conditions (hydraulic parameters).

Hydraulic parameters

The hydraulic parameters are all parameters that play a role in the forces acting on the wall, theretofore have to be considered during the design face.

- **Wave Height (H_s, H, H_{m0})**: Wave height is a critical factor in crown wall design, as the wall must withstand the forces exerted by the waves. Traditionally, the significant wave height (H_s), defined as the average height of the highest one-third of the waves, has been the standard metric, as utilized by Pedersen (1996). However, recent advancements in design practices have favored the use of the 0.1% wave height, as demonstrated by Nørgaard et al. (2013). This preference results from the need to take extreme wave events into account, since these lead to instant failure. In order to ensure the stability of crown walls in the worst-case scenarios, a more accurate portrayal of these extreme scenarios is provided by the 0.1% wave height.
- **Wave period ($T_p, T_{m-1,0}$)**: The mean spectral wave period ($T_{m-1,0}$) and peak period (T_p), which are obtained from the wave spectrum, are the two most commonly utilized wave periods.
- **Wave length (L_{0p}, L_{0m})**: Both represent the deep water wave length. L_{0p} represents the deep water wave length based on wave period T_p: $\frac{gT_p^2}{2\pi}$, and L_{0m} is the average deep water wave length, where T_m is used.
- **Wave steepness (s_0p)**: During this study waves with steepness's (s_{0p}) of 1.5 % and 4 % were tested. s_{0p} is defined as the ratio of wave height to wave length. Generally speaking, a storm wave has a steepness of 0.04, while a swell wave has a steepness of 0.015. Therefore this research studies the effects of both wave types.
- **Breaker parameter (ξ)**: This parameter defines the type of breaking of waves on a slope. It can be calculated with the following ratio: $\frac{tan\alpha}{\sqrt{H_s\ L_{0p}}}$. Here α represents the slope angle of the breakwater and L_{0p} is based on T_p

Physical parameters

To enhance the readability of this section, Fig. 3.1 illustrates the parameters, while Table 3.1 provides a comprehensive overview of all the parameters.

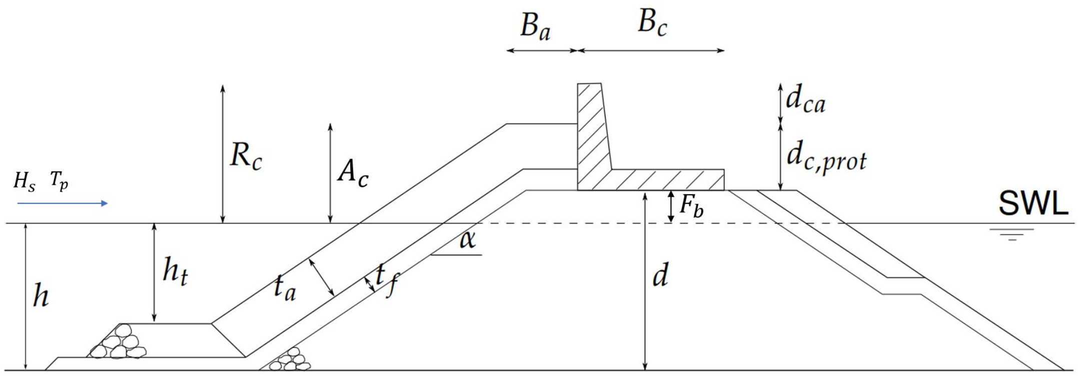

Figure 3.1: Physical parameters CIRIA et al. (2007)

Parameters	Description	Unit
h	Water depth	m
h_t	Water depth at the toe	m
R_C	Crest freeboard above still water level (SWL)	m
A_C	Armour crest freeboard above SWL	m
F_b	Base freeboard	m
t_a	Thickness of the armour layer ($\approx 2d_{n50}$)	m
t_f	Thickness of filter layer (not used in model)	m
α	Slope angle of the breakwater	$\circ$
B_a	Armour berm width	m
B_c	Width of the crown wall	m
d	Height of the rubble mound breakwater	m
d_{ca}	Unprotected crown wall height	m
$d_{c,prot}$	Protected crown wall height	m
k	Permeability	m/s

Table 3.1: Table of physical parameters

Throughout the testing campaign, several key parameters were adjusted to examine their influence on the wave loading on a crown wall. The hydraulic parameters that were varied are wave height, water depth (and consequently, base freeboard), and wave steepness. The specific values for these parameters are detailed in Section 3.3. Additionally, the main physical parameter varied in this study is the permeability, which is further discussed in Section 3.5 and Subsection 3.6.1.

3.2. Scaling

The scaling down of coastal structures to research multiple aspects and derive valuable insights, is a common measure applied in the discipline of coastal engineering. Advantages of these experiments, when scaled down, is that conditions (e.g. wave height, steepness, etc) are easier to control, therefore simplifying the research on the influence of geometrical parameters. Almost, all known formulations in the field of coastal engineering are derived in likewise manner, which can also be concluded from the literature research.

This method of study, however, is not universally applicable, as there is a limit to how much the prototype can be downscaled, depending on the research topic. Scaling the model can introduce discrepancies between the model and the prototype. Significant disparities result in model, measurement, and scale effects, which will be briefly discussed shortly.

- **Model effects**: Differences between prototype and down scaled model, (examples: different wave height or length and different breakwater geometries).
- **Measurement effects**: Differences in the measurement techniques between the model and the prototype.
- **Scale effects**: Arise when force ratios between the prototype and scale model are not similar, resulting in deviations when the model is up-scaled to real-world dimensions. The study's main aim is to research the forces and pressures on a crown wall, therefore, the aim is to reduce the occurrence of scale effects.

To describe the occurring scale effects, a scale factor can be used (Eq. (2.7)), which compares the characteristic length of the prototype and model (Heller, 2011).

$$n_L = \frac{L_p}{L_m} \tag{3.1}$$

Since, this study is not based on a specific breakwater, a rather standard breakwater cross-section is used. Primarily because testing a conventional breakwater will yield more valuable insights than examining a rather specific cross-section of a breakwater. Since, reducing scale effects is of the largest importance in this study, these will be further elaborated in the following.

Similitude and scale effects

A model that behaves identical to it's prototype is referred to as mechanical similar. This similitude, identical behaviour, of the model to prototype is required within three classes (Schiereck, 2019):

- **Geometric similarity**: implies similar shape. When all the geometric lengths in the prototype have the same scale factor as the model (parameters: length, area and volume)
- **Kinematic similarity**: the time-dependent processes in the model have similar time relations to the processes in real-life (parameters: velocity, acceleration and discharge)
- **Dynamic similarity**: entails that forces in model and nature have a constant relation, also ensuring geometric and kinematic similarity.

Since, the study focuses on the forces on a crown wall, scaling laws that guarantee dynamic similarity are used to calculate different parameters for the scale model. Below, the three most important scaling laws can be seen and a short describtion is given. Froude relates the inertial force to the gravitational force. Reynolds relates the inertial to the viscous force and Weber, subsequently, relates the inertial force to the surface tension. To conclude, all laws give a ratio between a specific force to the inertial force and are given below (Wolters et al., 2010).

$$
\begin{aligned}
Froude &= (\frac{inertialforce}{gravityforce})^{0.5} = \frac{u}{\sqrt{gL}}, \\
Reynolds &= \frac{inertialforce}{viscousforce} = \frac{uL}{v_k} \\
Weber &= \frac{inertialforce}{surfacetensionforce} = \frac{\rho u^2 L}{\sigma}
\end{aligned}
\tag{3.2}
$$

To create dynamic similitude of the rubble mound breakwater, the above given numbers have to be similar in the model and prototype. According to Frostick et al. (2011), this is impossible, since scaling a model for Froude and Reynolds similarity, needs subsequent scaling of the ratio of kinematic viscosity between the model and the prototype, this however, remains fixed by the geometric scales. Therefore, for most scales, it becomes impossible to find a suitable fluid, which is why real similarity cannot be achieved.

To help engineers in the scaling of models Frostick et al. (2011) gives a few general scaling criteria that have to be obliged to. They do state that similarity of a structure depends on a variety of structural and physical parameters:

- Overall structural dimensions are scaled *geometrically*
- Flow hydrodynamics (waves) need to conform to *Froude scaling*
- Turbulent flow conditions have to exist within the armour layer
- It is advised to use large scales (since viscous forces can have a larger effect when too small models are used)

The following section discusses the scaling operations.

Geometrical similarity

As the general scaling criteria above describe, the largest dimensions possible should be to reduce model effects. Therefore the scaling to achieve geometric similarity, is limited by the dimensions of wave flume available for model tests, which is elaborated by Fig. 3.11. The working depth of the flume is between 0.5 - 0.7 m, however, since the largest waves will be used in the tests (0.2 m), a core crest height of 0.6 m is chosen.

Froude similarity

When scaling the model, a Froude scaling law should be used, since the wave field is mainly dominated by influences of gravity and inertia. To perform this procedure, the Froude number of the model, given in Eq. (3.2), should resemble the Froude number in the prototype. Therefore the Froude scaling factor is limited to 1. To scale all variables in the study (e.g. wave heigth, period and forces), this scale factor will be used.

$$
\begin{aligned}
\frac{u_{prototype}}{\sqrt{g_{prototype} L_{prototype}}} &= \frac{u_{model}}{\sqrt{g_{model} L_{model}}}, \\
n_{Fr} = 1 &= \frac{n_u}{\sqrt{n_g n_L}}
\end{aligned}
\tag{3.3}
$$

This Froude scaling law can be used to derive the scaling laws seen below, which are expressed in the scale factor n_L of the length, given in Eq. (3.1).

Wave height [m]	$n_H = n_L$
Time [s]	$n_T = n_L^{0.5}$
Velocity [m/s]	$n_T = n_L^{0.5}$
Acceleration [m/s^2]	$n_a = 1$
Mass [kg]	$n_M = n_\rho \cdot n_L^3$
Pressure [kN/m^2]	$n_P = n_\rho \cdot n_L$
Force [kN]	$n_F = n_\rho \cdot n_L^3$

Reynolds similarity

Besides Froude scaling, one should also apply Reynolds scaling to achieve Reynolds similarity. As already highlighted above, it is impossible to achieve both Froude and Reynolds similarity. Since, in our case, friction does not play a large role, due to the relative short length of the flume, the viscous forces do not have a large effect. Additionally, a considerable spectrum of Reynolds numbers have the same drag coefficient. Therefore, according to Wolters et al. (2010), when Froude scaling is used and it is insured that the Reynolds number of the model is in the same range of the prototype (turbulent or laminar), the Reynolds number does not have to be exactly the same.

Reynolds similarity becomes more important when the flow through a structure and drag forces on structures are modelled, which applies in this study. Therefore, ideally, one should come as close as possible to the Reynolds number of the prototype, and still accurately model the waves. Except when the Reynolds number is large enough and turbulent flow conditions in the armour layer are still present (Re > 30000) (Dai & Kamel, n.d.) scaling the forces by Froude alone is sufficient.

Weber similarity

Similar to the Reynolds similarity, the Weber similarity can be neglected, due to the fact that the surface tension is negligible on prototype scale. Given that the model is not too small, Weber similitude can be neglected (Dai & Kamel, n.d.). The conditions for which this holds are: $L > 3cm, T > 0.35s$ and $h > 2cm$. Since, all test conditions meet these limit conditions, Weber similarity can safely be neglected. If not, the model will exhibit wave motion dampening, which is not present in the prototype.

Permeability similarity

Scaling of the under layers and core is crucial to correctly represent the prototype. Geometric scaling of this relatively small material, will lead to an increased influence of viscous scale effects since these layers can become less permeable, thus limiting wave-driven flows through porous materials and increasing the flow effects in the armour (Oumeraci, 1984). Subsequently, this scaling approach leads to different of reflection and transmission values, compared to reality - more energy reflected (due to the smaller permeability) and less transmitted. To address the influence of scaling effects in this study, we propose to scale based on permeability, by altering the the rock sizes. Permeability scaling, as this approach is called, is accomplished by computing the hydraulic gradient between the different layers (van Gent, 1995b; Wolters et al., 2010). The Forchheimer equation (Eq. (3.4)) is used in this approach (Wolters et al., 2010) and is illustrated below:

$$I = au_f + bu_f|u_f| \tag{3.4}$$

Where:

I	=	Hydraulic gradient [m]
u_f	=	Filter velocity [m/s]
a & b	=	Friction coefficients [s/m] & [s^2/m^2]

The friction coefficients have been derived by van Gent (1995a, 1995b). The first term of Eq. (3.4) symbolizes the importance of the laminar flow and the second term (with quadratic velocity) the turbulent flow term. For large diameter materials (prototype scale) the laminar term can be neglected and the turbulent term can be neglected when scaling down, and the viscous forces gain importance. Therefore, the ratio of both terms give the relative importance. If Froude scaling is applied and rock diameter of 7 mm or larger ($D_{n50,core,froude} > 7mm$) is found, the following relation regarding the enlargement factor holds Wolters et al. (2014):

$$\frac{D_{n50,core,corr}}{D_{n50,core,froude}} = 1 \tag{3.5}$$

In essence, this suggests that rock diameters exceeding 7 mm require no enlargement factor. Similar to Reynolds scaling, permeability scaling can be neglected if rock diameters are sufficiently large. Furthermore, viscous forces can be minimized in the model if the diameter exceeds 3-5 mm (in model scale) (Wolters et al., 2010). Hence, the scaling of the core material is is chosen such that the model maintains a similar turbulent regime as the prototype, adhering to the aforementioned guidelines.

3.3. Test conditions

As already touched upon, the test conditions used in this research, will be discussed in the following section. During this research two types of waves are used. Waves with a low steepness ($s_{op} = 0.015$), hereafter referred as 'swell waves' and waves with a high steepness ($s_{op} = 0.04$), referred to as 'storm waves'. Furthermore, the research uses 3 wave heights ($H_s = 0.11 - 0.13 - 0.15cm$) and 3 different water levels ($h = 0.55 - 0.57 - 0.59cm$). The water levels, were chosen in such a way to reproduce the non-zero freeboard scenarios, implying that during all test conditions the still water level was always lower than the base of the crown wall ($h = 0.60cm$). The full test program can be seen in Appendix E. Since, one of the goals of this research is to study the influence of core permeability on the uplift pressures on crown wall, the largest part of the test program will be repeated for both core types. This approach allows for a direct comparison between both set-ups. A quick overview of all the test conditions used can be seen Table 3.2 .

Symbol	Description	Value
H_s	Significant wave height	0.11 - 0.13 - 0.15 (m)
h	Water depth	0.55 - 0.57 - 0.59 (m)
F_c	Base freeboard	0.01 - 0.03 - 0.05 (m)
s_{0p}	wave steepness	0.04 - 0.015

Table 3.2: Overview of test conditions

3.4. Stability tests

The key tests during this research will consist of both stability tests and pressure measurements. In the stability tests, the transition point of stability is examined by iteratively adjusting the weight. By following this procedure, the critical weight—under which the crown wall is barely stable and shows no movement—is studied. Simultaneously, pressure transducers, further elaborated in Subsection 3.6.1, will be used to measure and analyze the pressures acting along the crown wall.

As was previously mentioned, pressure measurements and stability evaluations are the two primary topics of the main tests. The purpose of the stability tests is to determine whether the crown wall remains in position hence defining a precise failure criterion is essential. The failure threshold has been defined as a displacement greater than 0.2 mm. This value was used because it is the measurement accuracy of the equipment chosen to track the displacement of the structure, which was a magnetic proximity switch with a range of 2 cm, illustrated in Fig. 3.2. A stopping mechanism was installed at top of the core to protect the proximity switch from potential harm in the event of severe wall movement.

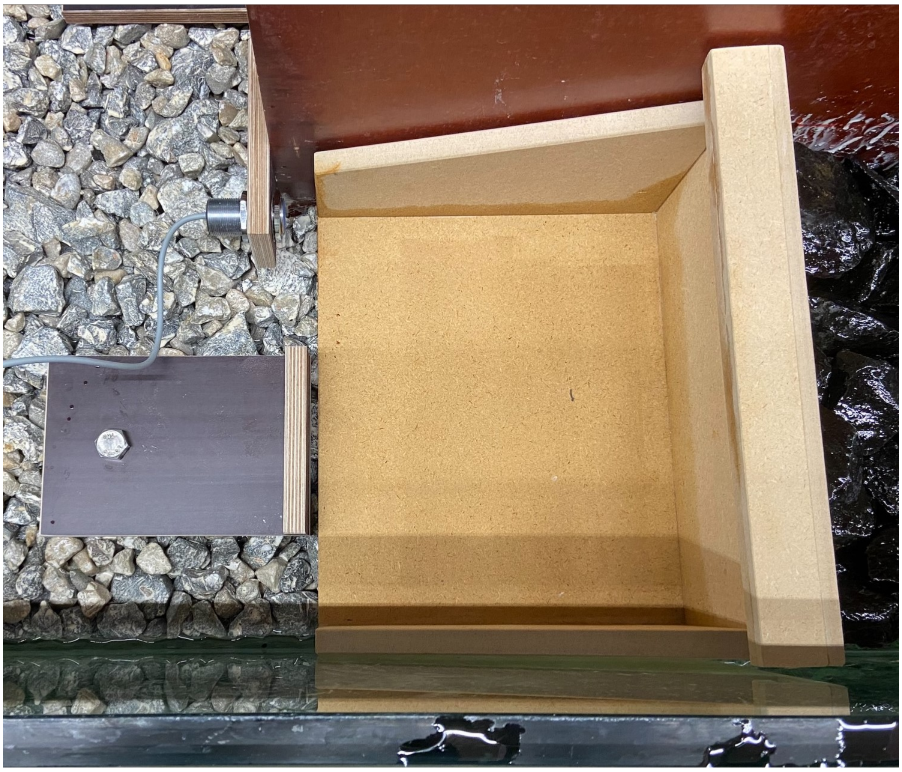

Figure 3.2: Stopping mechanism used during testing campaign

3.5. Permeability test

Since a significant part of the conclusions from this study will be based on comparing the permeability of both cores, it is valuable to test both permeability's. This was conducted using the constant head test, of which pictures and a brief explanation are provided in Appendix B. The results of this test are presented in the table below.

	Value (m/s)
Permeable core	0.16
Less permeable core	0.10

3.6. Experimental set-up

Following section discusses the experimental set-up. Firstly, the small scale model is discussed, treating all components and the assumptions made. Followed by the layout of the flume.

3.6.1. Model description

As previously mentioned, a breakwater with standard cross-sectional dimensions is selected to yield the most valuable insights, as it is more practical than opting for atypical dimensions. A typical breakwater slope of 1:2 is chosen, without a rear slope, as this aspect is not within the scope of the study. Additionally, the design guidelines in CIRIA et al. (2007) are adhered to. Therefore the widths of crest and toe are chosen to be: 3 * D_{n50} and the thickness of the armour layer is 2 * D_{n50}.

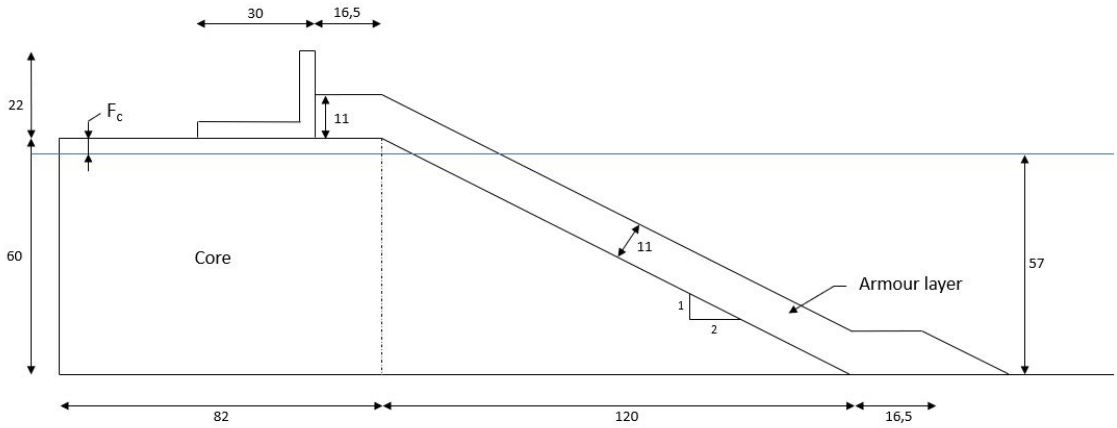

Figure 3.3: Breakwater cross section [cm]

This study reuses the core Veringa (2023) created, therefore sharing the same characteristics, which can be found in Appendix F. Throughout this study, it is referred to as 'permeable core'. This granular core material was glued together, using epoxy, creating a solid block. Additionally, the study tests a different, less permeable, core. The characteristics of this, less permeable, core, are chosen based on the permeability of the permeable core. This is done to ensure that both core types have different permeabilities. By comparing the effects of both cores, it is hoped to gain greater knowledge on the influence of permeability on the uplift pressures.

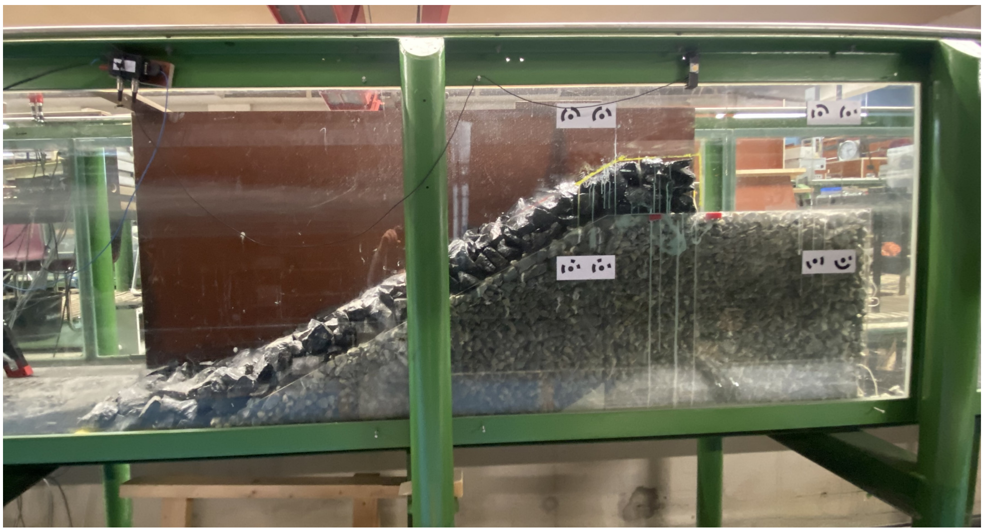

Figure 3.4: Side view of the first tested setup with a permeable core.

The permeability can be calculated using the parameters of the permeable core listed in Appendix F and formula 5.293 in CIRIA et al. (2007), yielding k = 0.16 m/s. As shown in Appendix B, the calculated permeability was tested and found to align with the actual measured permeability. With a $D_{n50} = 0.9$ cm as opposed to the permeable core's $D_{n50} = 2.21$ cm, smaller material was utilized to create the less permeable core. Additionally, both core types have a wide grading in accordance with CIRIA et al. (2007). Ultimately, a less permeable core was created, resulting in a permeability of 0.10 m/s, which still indicates turbulent flow and is therefore representative of actual conditions.

Figure 3.5: Side view of the second tested setup with a less permeable core.

Armour layer

As already highlighted, the guidelines given by CIRIA et al. (2007) were used to design a model with typical dimensions. With the help of the van der Meer and Stam (1992) equations, the nominal rock diameter of the armor layer can be calculated. With the conditions of the test program and the parameters given in Table 3.3 a nominal rock diameter of 5.28 cm was calculated. By using these stones, the armour layer and stones in the permeable core, also comply with the breakwater filter rule: $D_{n50,a}/D_{n50,f} \approx 2.2$, given by (Schiereck, 2019). Therefore, no filter between both layers was needed. To ensure the stability of the armour layer and to ensure that moving stones will not affect the measurements, it was chosen to coat the armour rocks in epoxy. The final sieve curve of the armour layer, as it's characteristics, can be seen in Appendix F.

Symbol	Description	Value
H_s	Significant wave height	15 cm
T_p	Peak wave period	2.55 s
P	Notional Permeability	0.4
S	Damage level	2
N	Storm Duration	waves
$cot(\alpha)$	slope angle	2
Δ	Submerged Density	1.65
$D_{n,50}$	Nominal Diameter	5.28 cm

Table 3.3: Parameters used to calculated required $D_{n,50}$

The less permeable core, however, did not satisfy the above mentioned filter rule. Therefore, a mesh was used to act as filter between both layers. The mesh had relative large gaps, 1.0 cm, since the main function was to prevent movement of material between both layers. The mesh is illustrated in Fig. 3.7, before placement of the armour layer.

Figure 3.6: Construction of the armour layer

Figure 3.7: Mesh used with less permeable core.

Crown wall

The chosen material for the crown wall is tricoya wood. This material was selected primarily because it demonstrates minimal expansion when in contact with water. Consequently, it is reasonable to assume that during the tests, this characteristic will have no effect on the pressure measurements.

For research purposes, larger dimensions were chosen for the crown wall, especially when comparing the model to a prototype. The height of the vertical face was increased to illustrate a larger unprotected part, providing a greater area for horizontal pressure distribution. This layout enables for direct comparison between the protected and unprotected sections. Additionally, the base of the crown wall was chosen to be larger to provide sufficient length for measuring the point of zero uplift pressure, as observed by both Bekker (2017) and Veringa (2023). Consequently, the face of the crown wall had a height of 22 cm and the base a width of 30 cm. An illustration of the crown wall layout can be found in Appendix G.

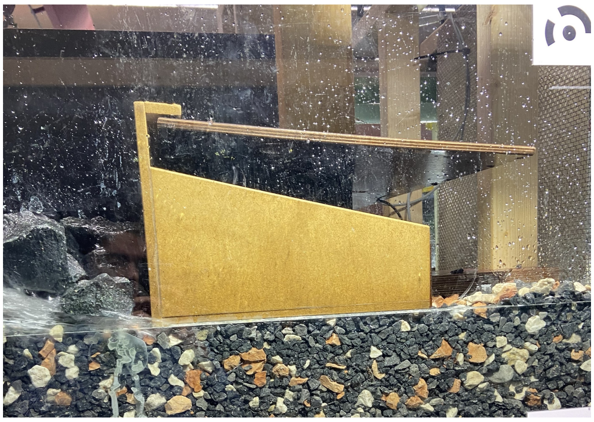

Figure 3.8: Crown wall positioned on the less permeable core.

Sensor placement

For this study, 13 temperature shock-proof sensors were available for use, with 1 spare sensor allocated to address any issues during the testing campaign. Consequently, areas of interest along the crown wall needed to be identified. Given that the primary focus of this research was on uplift pressures, the majority of sensors were installed in the base of the crown wall. Furthermore, the seaward part of the base was deemed more critical, as it was expected to experience the highest pressures and the gradual reduction of uplift pressure. As a result, a higher sensor density was chosen for the seaward part of the base, compared to the leeside.

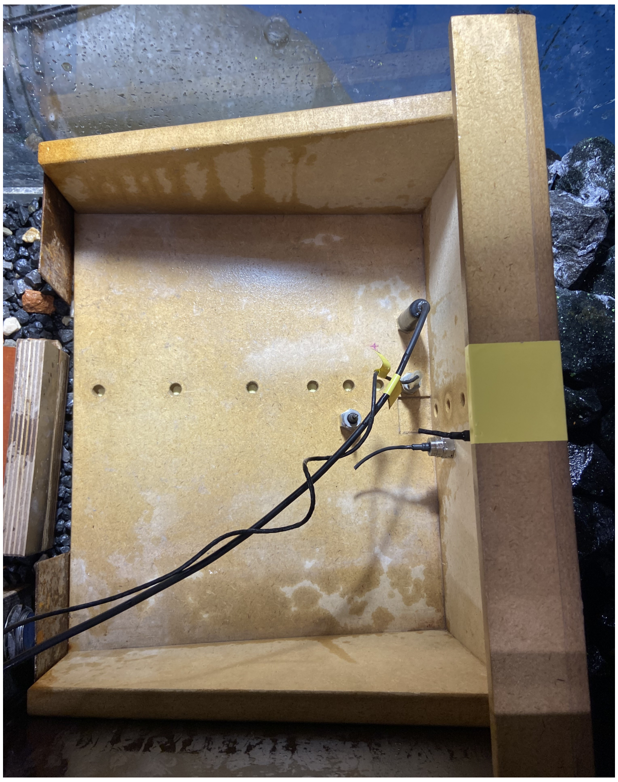

Figure 3.9: Pressure transducers from TU Delft (lower, thinner cable) and Deltares (upper, thicker cable) used during the sensitivity analysis, each connected to its respective amplifier (not visible in the image).

It was decided to install an equal number of sensors in both the protected and unprotected parts of the face, with equal distances between each sensor. This led to three sensors being installed in each section. Another consideration was the placement of sensors at the corner of the crown wall, where the face and base meet. It was chosen to install sensors in both the face and base at equal distances (2 cm) from the corner, ensuring that the extrapolation lengths for determining pressures were equal at the corner. Achieving this required staggering the sensors, resulting in a different line of installation, as illustrated in Fig. 3.10. A detailed overview of sensor placement in both the base and face can be found in Appendix G.

Figure 3.10: Staggering of the sensors

3.7. Flume

The 2D wave flume in the Hydraulic Engineering laboratory at the Delft University of Technology is used for the model tests. The flume has an effective length of 39 m, width of 0.79 m, height of 1 m and a typical working depth of 0.5 - 0.7 m. The waves in the flume are generated via an electrical piston-type generator, that is able to generate waves up to 0.2 m, both regular as irregular. Additionally, the flume has an active reflection correction (ARC) installed, this system compensates the wave paddle to account for the reflected waves of the breakwater, therefore, it prevents that the reflected waves will be re-reflected back again into the wave flume. The ARC is able to do this for both waves and flow, or combination of both.

Furthermore, Fig. 3.11, gives an illustration of the model test set-up in the wave flume. In this study two sets of three wave gauges are used, this is done to assure that the desired wave conditions are present in the tests and to fulfill the objective set-out in Section 1.4, to use the data to generate a comprehensive dataset of wave data. The wave gauges are arranged as such, that the length of the deep water section (between wave paddle and breakwater slope) is long enough to ensure that the evanescent wave modes near the wave paddle have decayed. Usually a length of 3–5 m fulfils these requirements (Frostick et al., 2011).

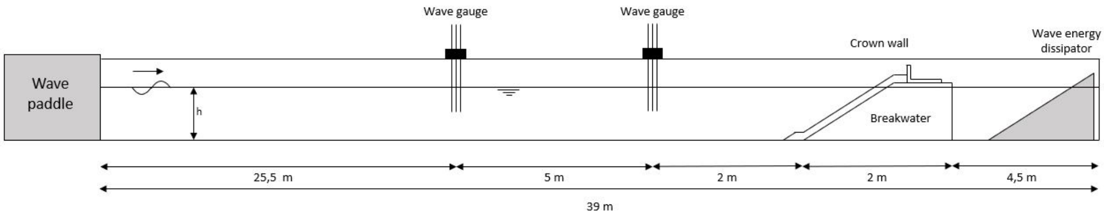

Figure 3.11: Flume overview used during model tests (not to scale)

An overview of all the instruments used during this testing campaign, can be found in Appendix C.

Part II

Test results

4

Experimental results and analysis

The main objective of this research is to explore the relation between the permeability of the breakwater core and the stability of a crown wall under varying wave conditions. This chapter is structured to address this objective. Before starting the analysis and discuss the results, it is important to elaborate on how the forces are derived. It then delves deeper into the analysis of these results to extract valuable insights from the testing campaign. This chapter addresses the following topics to ultimately provide a comprehensive answer to the research question:

- Pressures along the crown wall
- Forces on the structure
- Analysis of the stability (Factor of Safety)

4.1. Pressure signal analysis

Similar to the observations made by Veringa (2023), an ambiguous phenomenon in the pressure measurements was observed, identified as slow and fast decay. The fast decay occurs after wave impact on the pressure transducers, illustrated on Fig. 4.1, characterized by a high-pressure reading. In contrast, the slow decay is marked by a gradual return to the reference value over a period ranging from several minutes to up to two hours. This phenomenon was observed exclusively when the transducer was fully submerged, a condition that occurs with significant overtopping. However, this effect was not significant during the testing campaign, as only non-zero freeboard levels were tested. After applying his recommendation, to switch to a constant current (2V) instead of a constant voltage (10V), the phenomenon persisted but was significantly reduced, as is illustrated by the orange line in Fig. 4.1.

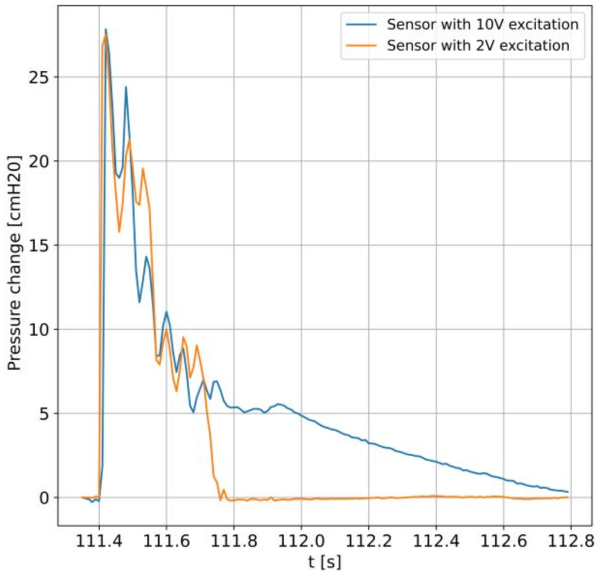

Figure 4.1: Illustration of the fast decay and the effect of switching to 2V, as provided. Obtained from. Veringa (2023)

A sensitivity analysis suggested that the observed effect could be attributed to the amplifiers from TU Delft, used to amplify the pressure signal. When the amplifiers from Deltares were employed, the effect appeared to diminish, and the pressure signal returned to approximately zero after the short negative pressure post-wave impact, as illustrated in Fig. 4.2. The conclusion is based on tests where both TU Delft and Deltares sensors and amplifiers were tested simultaneously. During these tests, the TU Delft sensors were connected to their corresponding amplifiers, and the Deltares sensors to theirs, as shown in Fig. 3.9. Both sets of sensors were mounted at the same location to ensure that identical forces were measured, allowing for a direct comparison of the outputs. The results indicate that, after using the Deltares sensor/amplifier combination, the pressure signal returned to roughly zero between waves, which is the expected behavior when no wave activity occurs. However, since this conclusion is based on a limited number of tests, it cannot be concluded that one sensor/amplifier combination is superior to the other, as the TU Delft sensor does not return to zero, while the Deltares sensors exhibit a high noise level. Both of these observed phenomena have magnitudes of the same order. Additionally, the observed bias of approximately 2 mm occurs during periods that are not of primary interest to this study, and this difference falls within the noise level of the Deltares amplifiers. Furthermore, the absolute value of the wave pressure peaks remains unaffected by this phenomenon; only the measurements between waves show variation. This is shown in Fig. 4.1, where the signals from both amplifiers remain consistently high during wave events. Given that this study focuses on the analysis of extreme wave forces, which are not impacted by the minor bias observed, no compensation or filtering has been applied to the pressure signal.

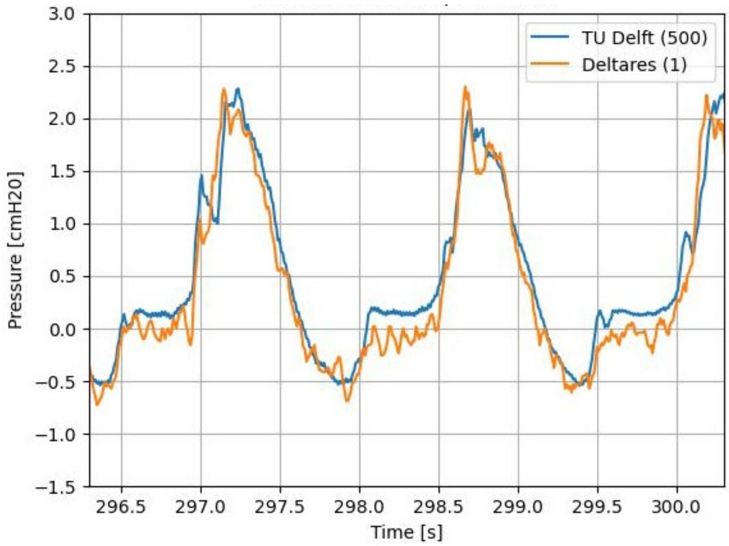

Figure 4.2: Pressure measurements from the sensitivity analysis comparing both amplifiers (TU Delft and Deltares). Sensors were mounted at the same location with respect to the incoming wave direction, using storm waves ($s_{0p} = 0.04$ and $H_s = 0.15$ m).

The effect itself was most pronounced in tests with the largest wave conditions, where greater volumes of overtopping were observed. This phenomenon was particularly evident in scenarios with the smallest base freeboard. It is therefore suggested that the issue may be caused by the rearside of the sensors (or cables) coming into contact with water, though this is not confirmed. Furthermore, the effect was also observed with the second, less permeable core, but the decay occurred at a much slower rate than with the permeable core. This suggests that the permeability of the core influences the severity of the phenomenon. This difference is likely because the less permeable core has smaller voids, which cause water to drain more slowly. As a result, there is less suction effect on the sensor, making the decay less pronounced in the less permeable core. Additionally, it was noted that the fast decay was not observed by the exposed sensors (above the armour layer), as shown in Fig. 4.5a, suggesting that the fact that sensors are covered by material might cause this phenomenon.

Pressure signal filtering

To enable this research, two additional sensors were borrowed from Deltares. Despite being identical to the existing sensors, differences in the pressure measurements were observed. The Deltares sensors exhibited significantly more noise, as shown in Figures Fig. 4.2 and Fig. 4.3b. Therefore, a moving average filter with a window size of 3 was applied to both Deltares signals. The initial measuring frequency was 100 Hz, which means that after the filter application the Deltares sensors measured with 30 Hz. The difference between the original and filtered signals is illustrated in Fig. 4.3.

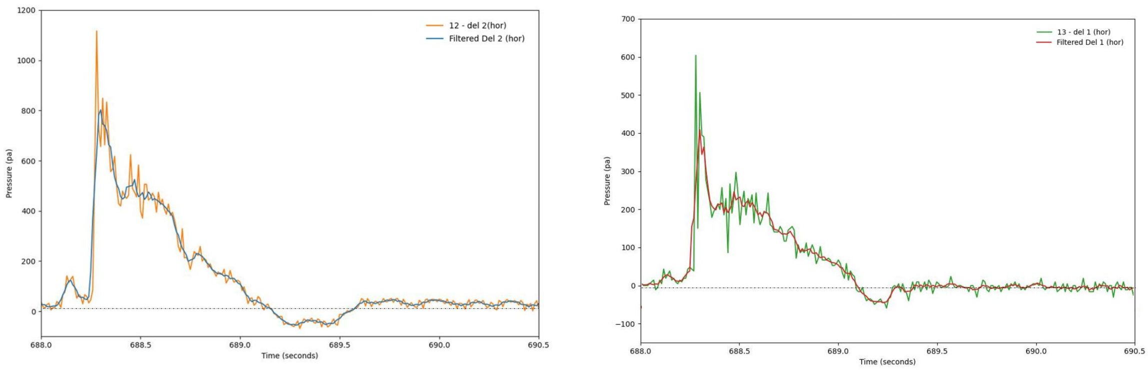

(a) Original and filtered data from Deltares sensor 2 **(b)** Original and filtered data from Deltares sensor 1

Figure 4.3: Raw and filtered data from both Deltares sensors

Pressure signal

After the filter is applied, the initial analysis of the pressure signal can be made. The analysis of the 13 data signals, corresponding to the 13 sensors used in the crown wall, will form the main part of the analysis. Fig. 4.4 gives an overview of which sensors are placed where along the crown wall. This illustration helps to understand Fig. 4.5, where the individual pressures are plotted per sensor. To enhance the readability, smoothners are used, and separation has been made between the horizontal and vertical pressure transducers. Fig. 4.5a illustrates the horizontal pressures and Fig. 4.5b shows the vertical pressures, with pressure (pa) on the y-axis and time on the x-axis.

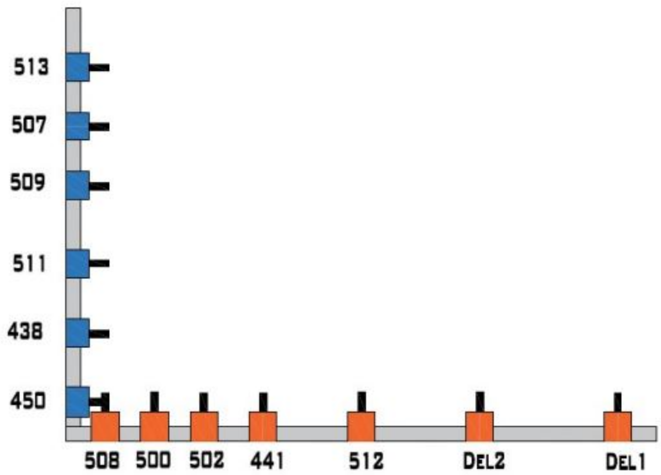

Figure 4.4: Sketch of the sensors along the crown wall

When analyzing Fig. 4.5, several conclusions can be drawn. The time lag between the horizontal and vertical pressures, as observed by Bekker (2017) and Veringa (2023), is evident in both graphs, thereby confirming their findings. Subsequently, the graph illustrates that the horizontal pressures are larger compared to the vertical pressures. The pressure readings illustrate another effect: the pressure 'wave' through the porous medium is clearly visible after wave impact. This is evidenced by the sensors at the back of the crown wall base (Deltares 1 & 2) measuring a pressure increase later in time than the sensors at the front (508 & 500). Chronologically, the pressure increases from the front to the back of the base, illustrating the pressure wave through the porous core. This effect is not present in the sensors measuring horizontal pressures, as they are simultaneously exposed to the wave impact, which affects all the horizontal sensors at once.

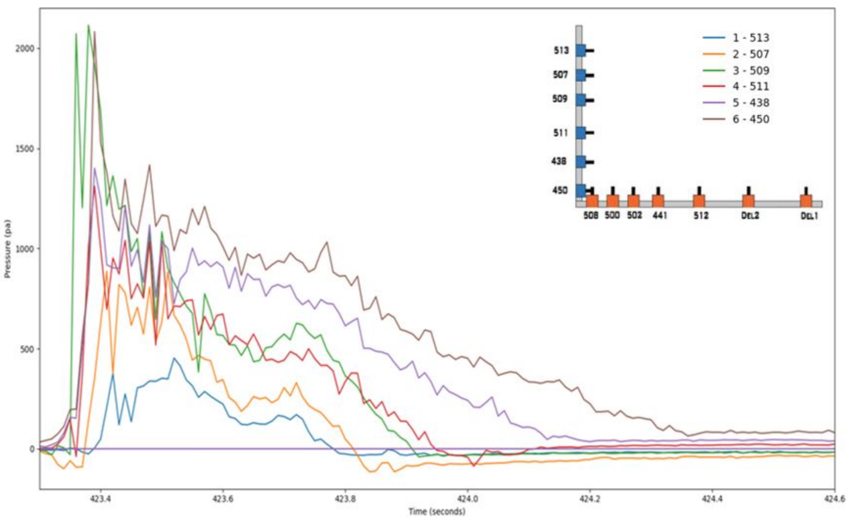

(a) Horizontal pressure after the impact of a representative wave.

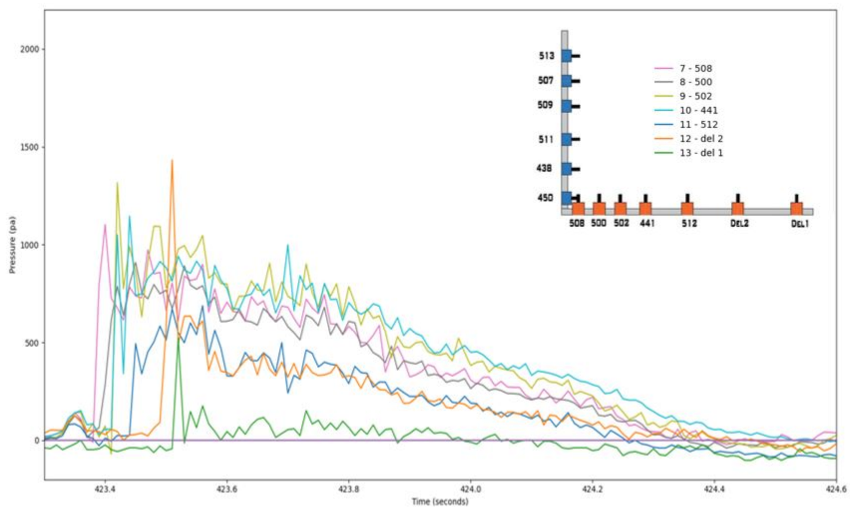

(b) Vertical pressure after the impact of a representative wave.

Figure 4.5: Pressures along a crown wall after the impact of a representative wave.

Another notable observation is that the phenomenon previously described as 'fast' decay is more prominent in the covered sensors. The sensors in the unprotected part of the crown wall face (sensors 513, 507, and 509 in Fig. 4.5a) illustrate a much faster decay. In contrast, the covered sensors, both on the face and the base, display a more pronounced slow decay, with pressure readings taking longer to return to zero. This suggests that the slow decay is caused by the sensors being covered, which may delay the immediate drainage of water, leading to a slow decay rather than a rapid return to zero pressure. Therefore, it can be concluded that this slow decay effect results from an underlying physical process. Detailed drawings of the crown walls and the sensor locations are provided in Appendix G.

Another notable point is that the measurements do not align with the assumed horizontal pressure profile (by Pedersen, 1996), which assumed a step-wise decrease for the protected part behind the armour layer. This profile is explained and illustrated in Section 1.3. The assumed pressure reduction—a 50% decrease—is not observed in the data. For example, in Fig. 4.5a, sensor 450 (brown line) should display half the pressure of sensor 509 (green line). However, this is not the case, which may indicate that a different process is occurring.

Spatial distribution

An alternative and more insightful approach to examine the pressures involves graphing all individual sensor measurements based on their specific positions on the crown wall. The visualization is essential for comprehending the spatial arrangement of pressures during critical loading. The depiction of the pressure distribution, at that instance, is a frequent used method in the literature. Therefore, it is important to precisely graph this distribution, as is done in Fig. 4.6. In this figure a representative wave is shown, as is mentioned in the figure description.

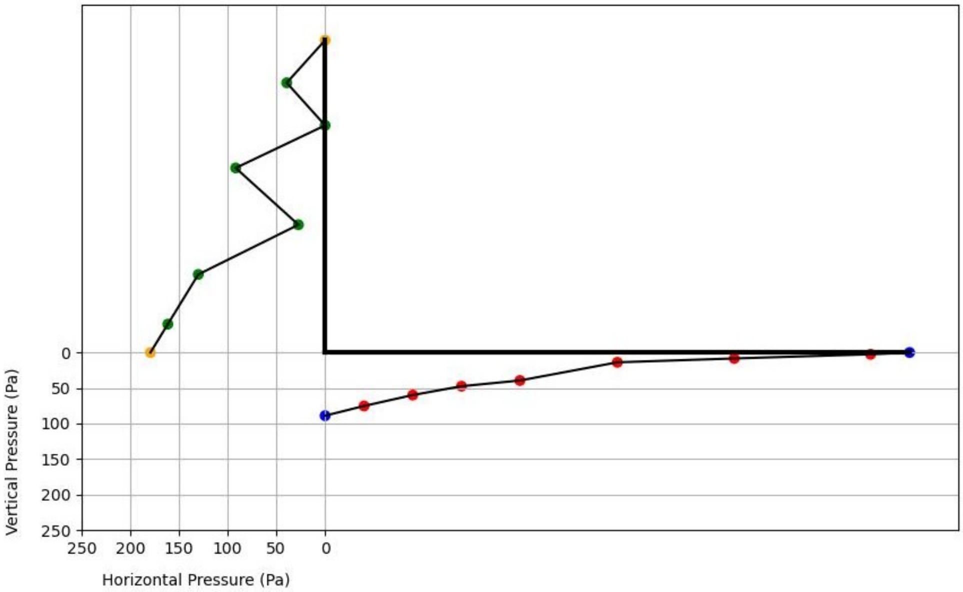

Figure 4.6: Pressure diagram during the impact of an representative wave (conditions: $H_s = 0.15$ m & $F_c = 0.05$ m & $s_{0p} = 0.04$)

The pressure transducers assist in generating a pressure diagram. The red dots indicate the measured vertical pressure, while the green dots represent the horizontal pressure. However, further details about the pressure diagrams will be discussed in a subsequent section. Examining the pressure diagram is essential for comprehending the effects of increasing freeboard on uplift pressures, as emphasized in the literature. Fig. 4.6 illustrates the pressure distribution for the largest freeboard employed during the testing campaign. The polynomial-shaped distribution described by Bekker is evident, and the effect of the reduced wetted length is also apparent. Significant pressures are measured only at the seaward side of the base, indicating that the last part of the base remains dry the critical wave impact.

In Fig. 4.7 and Fig. 4.8, the pressure distributions are illustrated as a function of freeboard, wave steepness, and core permeability. This type of representation facilitates an easy comparison of the effect of core permeability on the pressure distribution. In both pressure diagrams, the solid points represent measurements from the pressure transducers, while the hollow points indicate extrapolated data.

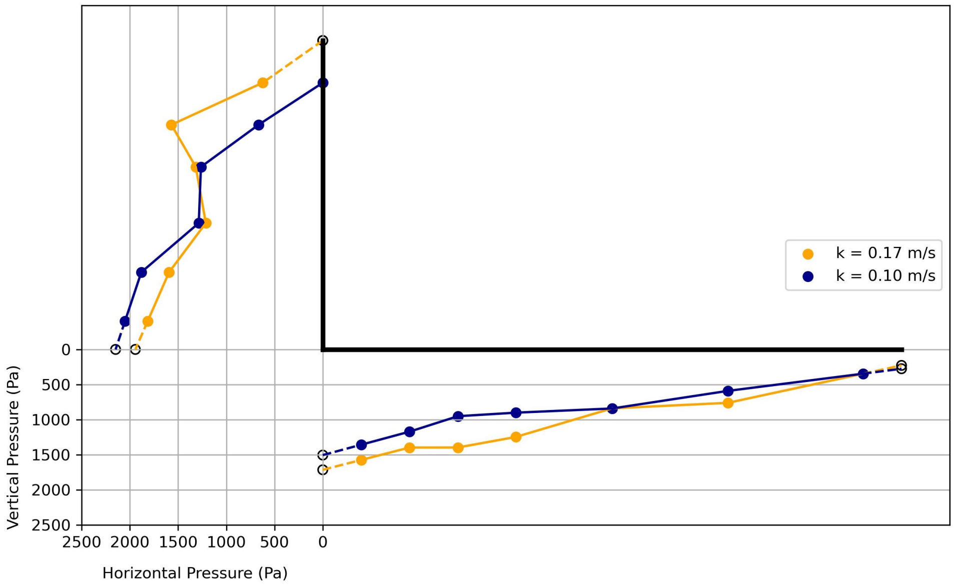

(a) Pressure distributions along the face and base of the crown wall. Here, a representative wave is shown with test conditions: $H_s = 0.15$ m, $s_{0p} = 0.015$ & $F_c = 0.01$ m

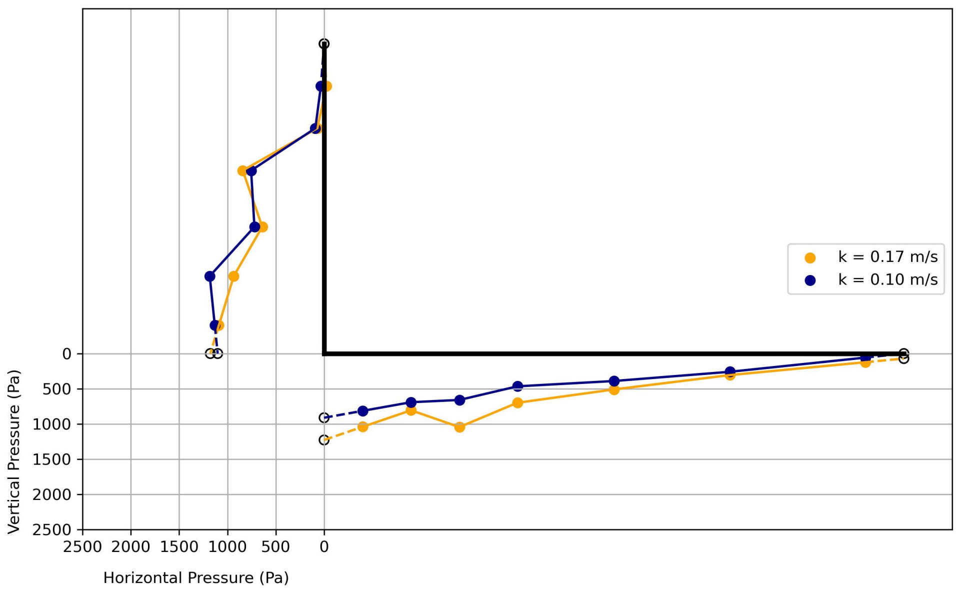

(b) Pressure distributions along the face and base of the crown wall. Here, a representative wave is shown with test conditions: $H_s = 0.15$ m, $s_{0p} = 0.4$ & $F_c = 0.01$ m

Figure 4.7: Pressure diagrams along the crown wall for a representative wave at an $F_c = 0.01$ m level, distinguishing between storm and swell waves, as well as both permeability conditions.

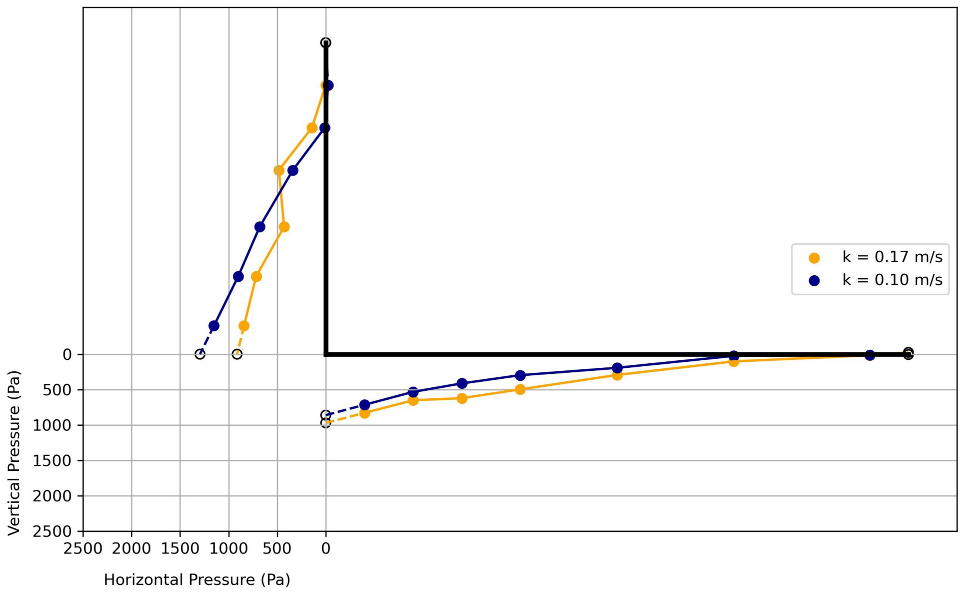

(a) Pressure distributions along the face and base of the crown wall. Here, a representative wave is shown with test conditions: $H_s = 0.15$ m, $s_{0p} = 0.015$ & $F_c = 0.05$ m

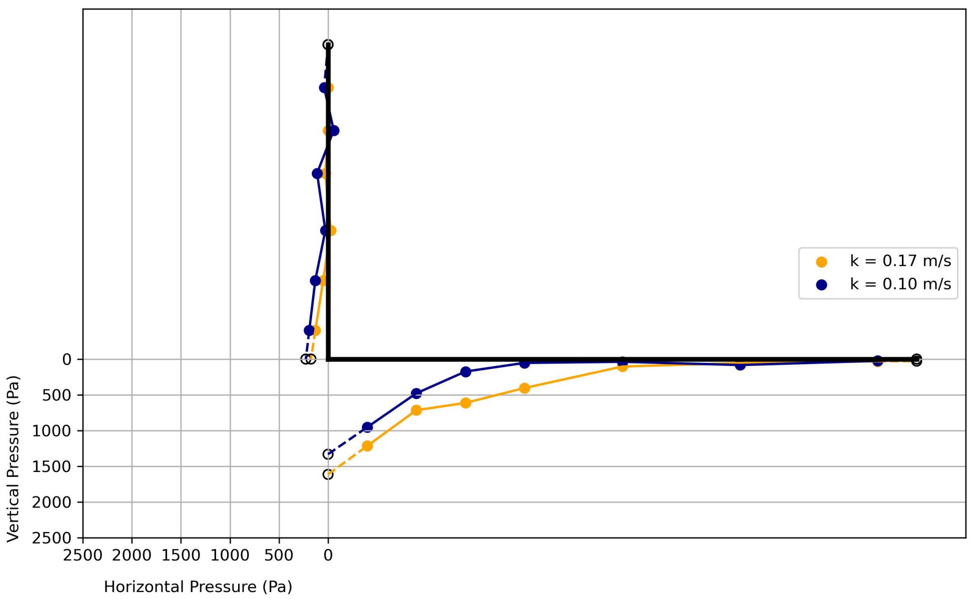

(b) Pressure distributions along the face and base of the crown wall. Here, a representative wave is shown with test conditions: $H_s = 0.15$ m, $s_{0p} = 0.4$ & $F_c = 0.05$ m

Figure 4.8: Pressure diagrams along the crown wall for a representative wave at an $F_c = 0.05$ m level, distinguishing between storm and swell waves, as well as both permeability conditions.

Upon careful examination of Figs. 4.7 and 4.8, several conclusions can be drawn. The effect of permeability is evident across all wave types and freeboard levels. This impact is observed in the uplift distributions, which show a reduction under all conditions, while the horizontal distributions illustrate the opposite, with an increase in pressure. For the uplift distribution, the shape remains unchanged, but the absolute value and the area under the curve (force, which will be further elaborated on in section Section 4.2) decreases. In contrast, the shape of the horizontal distribution does change, with a slight increase in the absolute pressure. This suggests that the dampening effect, or the reduction of force through the breakwater core, remains constant. The shape of the uplift pressure distributions along the crown wall base does not change, but the overall pressure/force decreases. The influence of the base freeboard is also evident, as shown in Figs. 4.7 and 4.8. In addition to the reduction in the total force acting on the crown wall, this influence is illustrated by the changing shape of the uplift pressure distribution. At higher freeboard levels, a significant portion of the base experiences no pressure, meaning it remains dry under these conditions. This effect is clearly demonstrated when comparing Figs. 4.7b and 4.8b, where an almost triangular distribution changes into a polynomial distribution, as described by Bekker et al. (2018). For a low base freeboard ($F_c = 0.01,$ m, Fig. 4.7), the uplift pressure distribution closely resembles an almost triangular shape, consistent with the pattern proposed by Pedersen (1996) and validated by subsequent studies. This pattern is observed across both long and short wavelengths (Fig. 4.7a and Fig. 4.7b), as well as for different levels of permeability.

Surprisingly, the pressure at the end of the crown wall base does not reach zero, for the longer waves, as is illustrated on Fig. 4.7a, which goes against the assumptions made by Pedersen (1996). This effect, however, has been described by Martin et al. (1999), but it is only observed for the long swell waves and not for short storm waves. This could be attributed to the movement of water underneath the crown wall. The distribution described by Bekker for high freeboard is easily observable. Furthermore, the influence of permeability is clearly apparent, since a lower permeability results in a shorter wetted length (Fig. 4.8b).

Temporal distribution

In addition to spatial distribution, temporal distribution of horizontal and vertical pressures can also be analyzed. By graphing these distributions at the moment of failure, as well as at a time step before and a few steps after, we can gain valuable insights. This approach enhances our understanding of pressure variations during the critical wave impact on the crown wall. This has been illustrated in Fig. 4.9 for long (swell) waves with a significant wave height of 0.15 m. The distribution at the critical moment of failure is shown by the green line (squares) in Fig. 4.9, while the blue line represents the step before. The three remaining lines illustrate the steps after, demonstrating the pace at which the pressure decreases.

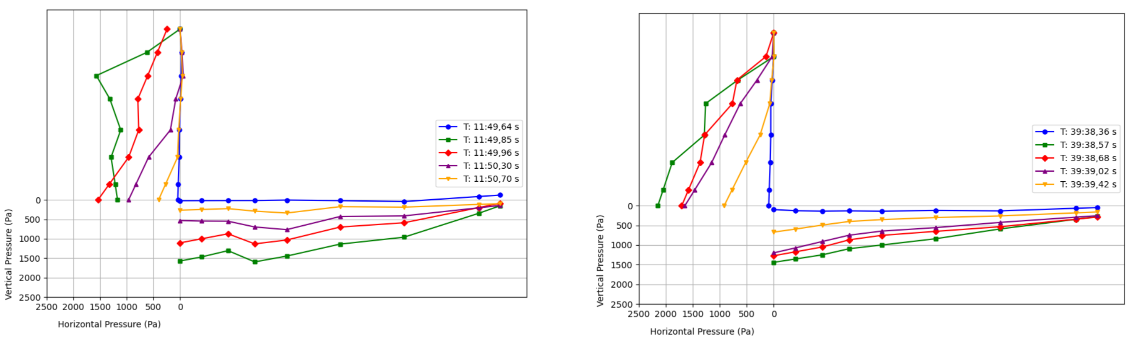

(a) Maximal vertical pressure at 5 timesteps for the permeable core (k = 0.16 m/s)

(b) Maximal vertical pressure at 5 timesteps for the less permeable core (k = 0.10 m/s)

Figure 4.9: Temporal distribution of maximal vertical pressure, where green squares indicate the instances of maximum pressure. Here, a representative wave is shown with test conditions: $Hs = 0.15$ m, $s_{0p} = 0.015$ and $F_c = 0.01$ m

Moreover, analyzing wave pressures requires consideration of not only the shape and amplitude of the pressure diagrams but also of their duration. A comparison of the two graphs in Fig. 4.9 reveals that the graph corresponding to the less permeable core (k = 0.10 m/s), shown in Fig. 4.27b, exhibits a slower rate of pressure decline. The time steps following the maximum pressures display nearly identical pressure profiles, with a significant drop in pressure occurring only in the final time step. In contrast, the more permeable core shows a different pattern. In the more permeable core, pressure decreases shortly after reaching its peak at each time step, indicating a greater capacity for water drainage compared to the less permeable core. Conversely, in the less permeable core, the reduced ability to rapidly remove water causes the pressure to persist longer within the permeable block, thereby prolonging the force within the core and on the crown wall base. This difference is a direct result of the permeability of the materials: lower permeability is associated with smaller voids, which slow down water drainage, while higher permeability allows for larger voids that enable faster water flow out of the breakwater core. As a result, the less permeable core retains pressure longer, which prolongs the force within the structure. This situation could have adverse effects, as rapid wave succession may prevent the less permeable core from relieving pressure in time, potentially leading to a dangerous pressure buildup.

4.2. Force analysis

After analyzing the individual pressure measurements, the next section will examine the forces acting on the crown wall. First, a short explanation will be given on the wave used in the analysis. Followed by a brief description of the methodology used to determine these forces, including the reasoning behind specific design choices. The section will conclude with a detailed analysis of the forces acting on the crown wall.

Wave climate

In the field of coastal engineering, it is common practice to test all coastal structures on their stability, just as is done in this study. This is mainly done by physical model tests, where a storm is simulated by means of three to six thousand waves, where the highest wave in the time series (0.1% wave) is of interest. Therefore, it is crucial to analyze the entire time series instead of individual waves, as this approach captures the highest wave, which is essential for stability calculations. It is therefore self-evident that the current calculation methods (Nørgaard et al., 2013; Pedersen, 1996; van Gent & van der Werf, 2019, also calculate this 0.1% impact force. However, using the 0.1% wave impact poses challenges due to the significant chance of outliers and the influence of coincidence. By analyzing the 1% wave largest, this possible problem, could be solved, being less vulnerable for coincidence. Nevertheless, the 0.1% can't be neglected since it is essential in the determination of stability. Therefore, by comparing both the 1% wave and 0.1% (largest) wave for all conditions, a relation could be derived. By creating a fit trough the gather data (the 1% and 0.1% wave), a relation is determined to make valuable conclusion on the 0.1% wave, which will be used when analyzing the stability. Nevertheless, the remainder of this section will continue the analysis with the 1% wave. The blue line in Fig. 4.10 presents the fit for the uplift forces for the permeable set-up, while the diagonal black line would represent a perfect alignment between $F_{v,1\%}$ and $F_{v,0.1\%}$. Appendix D reiterates Fig. 4.10 and additionally provides the regression statistics, including those for the less permeable set-up.

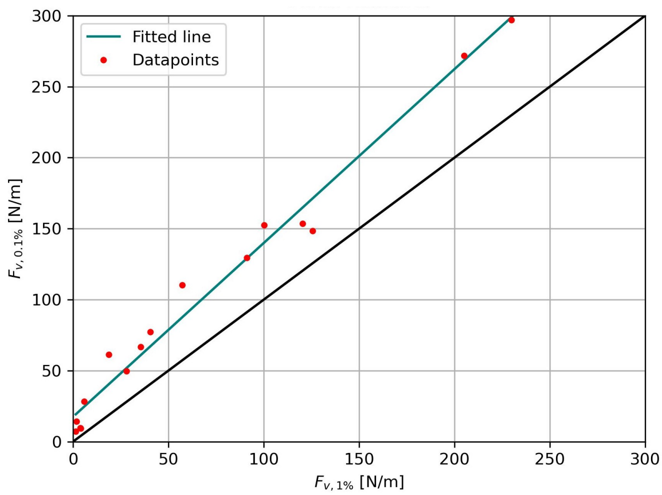

Figure 4.10: Fitted line through $F_{v,1\%}$ to calculate $F_{v,0.1\%}$

The main results will be derived by analysing the influence of the breakwater core permeability on the forces acting on a crown wall. This analysis will be done in the proceeding chapter, and the results of the testing campaign can be separate into different categories. The first part will concentrate on the horizontal and uplift forces. Subsequently, an examination of the stability of the crown wall and the time lag delay between the maximum vertical and horizontal forces will be conducted.

Wave Forces

All individual pressure sensors measured point pressure (Pa or kN/m^2) along the crown wall. The collection of these point pressures forms a pressure distribution on the face and base of the crown wall, as illustrated in Fig. 4.11 and analyzed in Section 4.1. Ideally, it is desirable to install a sensor at the corner of the wall and base, and another sensor at the distant end of the crown wall base. By selecting such a configuration, the ambiguity in pressure readings would be nearly completely eliminated, as the pressures would only require interpolation, rather than extrapolation. Nevertheless, this was not feasible due to the configuration, structure of the crown wall, and the design of the sensors (particularly due to their rear sides, as this is significantly larger than the anterior side). Consequently, the sensors were positioned as close as possible to these interest points, while ensuring that the extrapolation distances remained consistent, as depicted by the orange lines in Fig. 4.11. Interpolation takes place along the black lines in the shown figure. By carefully selecting the location of the sensors, it is possible to further reduce the level of uncertainty. The extrapolated pressures are constrained to a minimum value of zero. By integration, using the area formed underneath the pressure diagram, colored in light blue in Fig. 4.11, and using the acting width per sensor the forces along the crown wall are obtained. The integration of pressure resulted in a horizontal force (F_H) acting on the wall and a vertical force (F_V) at the base. The time signals of these forces were analyzed utilizing a Peak Over-Threshold methodology. The threshold is dynamically determined individually for each wave condition, as setting it too high may result in missing significant peaks. Only peaks above this threshold, with a maximum of one peak per wave, were considered, while peaks below this level were excluded.

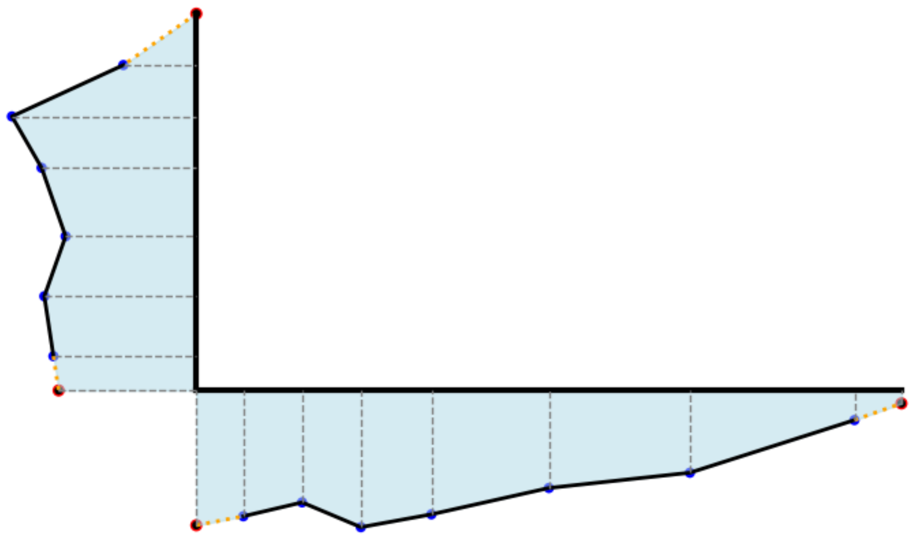

Figure 4.11: Principe of pressure integration

This methodology was employed to determine the forces, which are subsequently analyzed in the following section. Fig. 4.12 depicts the forces generated after wave impact for the 1% wave, comparing the permeable core (left) with the less permeable core (right). To facilitate a valid comparison between the two, the 1% wave is illustrated, as discussed in the first section of this chapter.

In all four graphs, the development of the horizontal and vertical forces after wave impact is visible. Notably, in Figs. 4.12b and 4.12d, it takes much longer for the uplift force to return to zero for the less permeable core. It takes nearly 2 seconds for the uplift force to return to zero, just before the next wave hits the structure. This confirms the conclusion made in Section 4.1. Furthermore, the analysis also includes an examination of the forces, in addition to its temporal distribution. Regarding the horizontal forces, there is an increase visible, when comparing Fig. 4.12c with Fig. 4.12d, however the vertical forces experience a far larger reduction. This is consistent with the anticipated modifications resulting from different permeabilities. Nevertheless, a sound conclusion can only be made by examining the complete time series, rather than a limited number of waves. The forthcoming part will involve an in-depth examination.

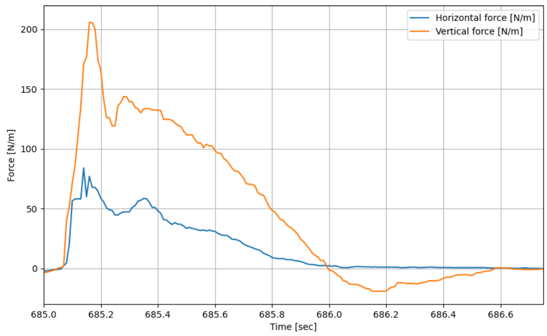

(a) $F_{v,1\%}$ after wave impact for the permeable core

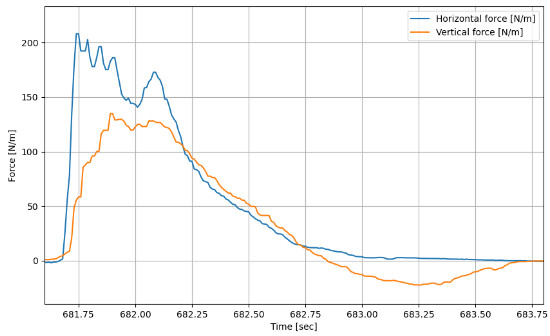

(b) $F_{v,1\%}$ after wave impact for the less permeable core

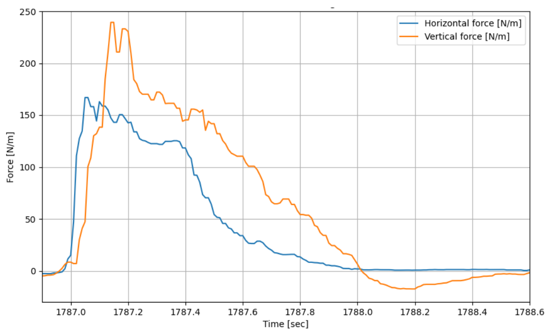

(c) $F_{h,1\%}$ after wave impact for the permeable core

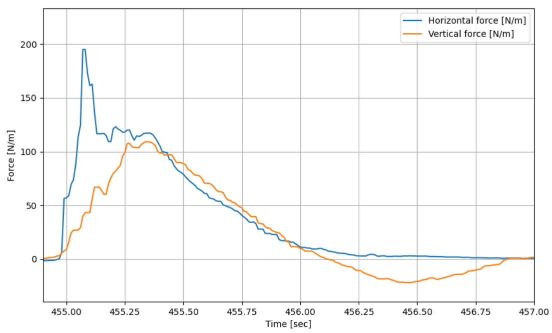

(d) $F_{h,1\%}$ after wave impact for the less permeable core

Figure 4.12: Illustrations showing both $F_{v,1\%}$ and $F_{h,1\%}$ for both tested set-ups ($H_s = 0.15$ m, $s_{0p} = 0.015$ & k = 0.16 - 0.10 m/s)

Uplift force

First and foremost, is the analysis on the uplift forces. As previously mentioned, this is conducted by examining the 1% wave. The time series of all wave conditions were analyzed, resulting in Fig. 4.13. Below, the measured uplift forces are illustrated, with a distinction made between short waves (left) and long waves (right).

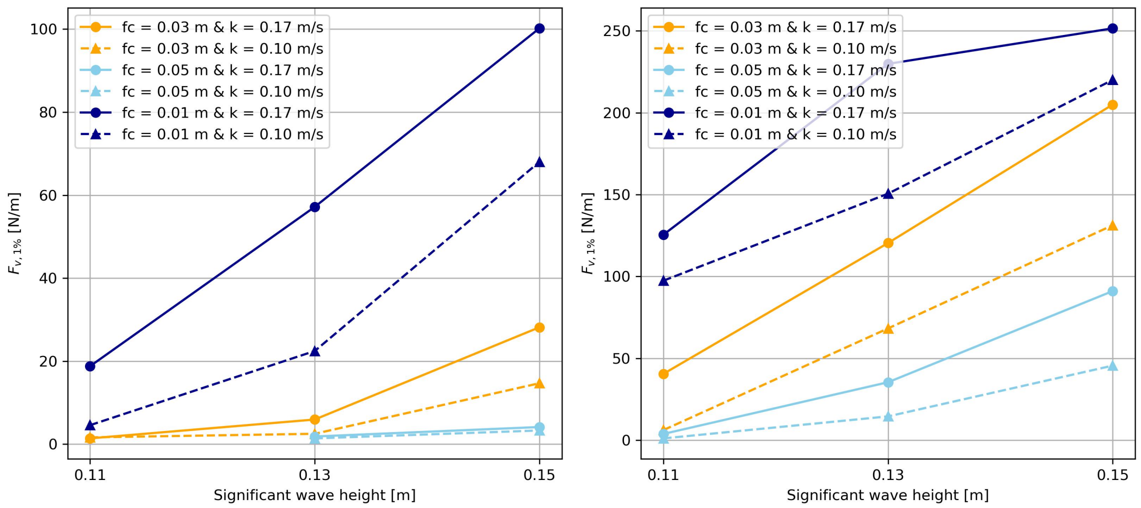

Figure 4.13: Uplift forces caused by the 1% wave for both test set-ups (permeable and less permeable cores). The left graph represents storm waves (s_{0p} = 0.04), and the right graph represents swell waves (s_{0p} = 0.015)

In Fig. 4.13, the influence of core permeability on the uplift forces is illustrated. In both graphs, the permeable core ($k = 0.16$ m/s) is represented with a solid line, while the less permeable core ($k = 0.10$ m/s) is displayed with a dashed line. Similar colors are used to plot identical freeboard levels, enhancing readability. When analyzing the graphs, it can concluded that the results are reasonably consistent, as all the dashed lines are below their corresponding solid lines, illustrating a clear force reduction. A reduction in permeability from 0.16 to 0.10 m/s results in an average uplift force reduction of 36% for storm waves and 46% for swell waves. This indicates that using a less permeable breakwater core leads to lower uplift forces acting on the base of the crown wall. The decrease in uplift forces can be explained by the reduced water infiltration into the less permeable core. A core with lower permeability allows less water to penetrate during wave impact, resulting in lower pore water pressures underneath the crown wall. Consequently, the uplift force exerted on the crown wall decreases. In other words, the less permeable core absorbs less water-induced pressure, leading to reduced upward forces compared to the more permeable core. The difference in uplift force reduction between storm waves and swell waves—namely, decreases of 36% and 46% respectively—can be attributed to the damping factor (δ) as outlined by Wolters et al. (2014). This damping factor depends on various variables, such as the wavelength, wave period, and the size of the core material. As the wavelength increases, the damping factor also increases, leading to a greater force reduction for swell waves. While the difference might seem minor, it provides a plausible explanation for the observed difference between the two wave steepnesses. Furthermore, for the less permeable core, smaller pressures were measured at each individual sensor due to the higher damping effect, which was not observed for the more permeable core. The increased damping in the less permeable core reduces the transmission of pressure within the core, leading to lower pressures and, consequently, reduced uplift forces on the crown wall. The reduced water infiltration, due to lower permeability, and the increased damping effect explain why the measured pressures and forces are lower in the less permeable core.

Horizontal force

A second point that can be analyzed is the horizontal forces acting on the face of the crown wall, as these also significantly contribute to the stability criterion.

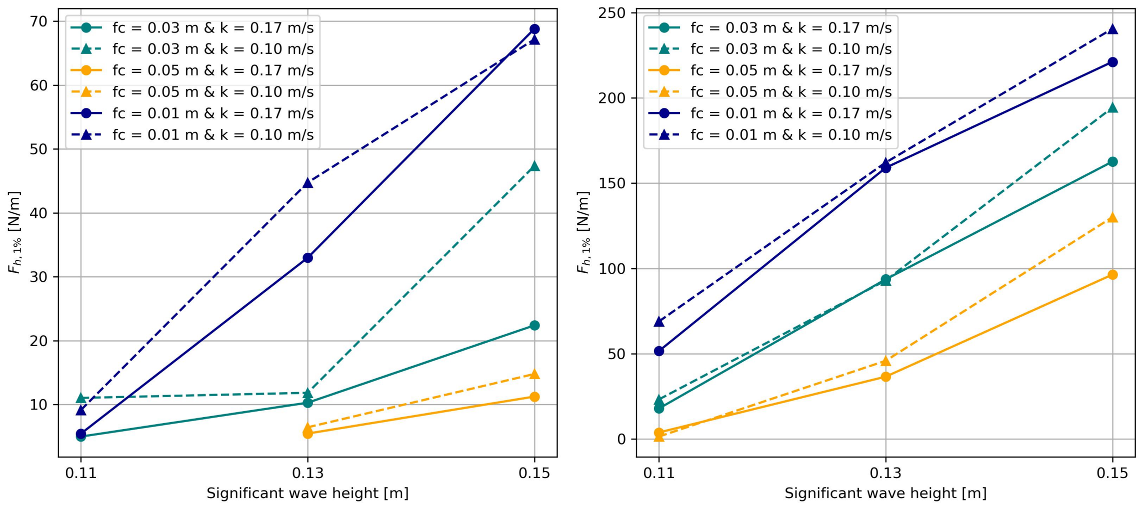

Figure 4.14: Horizontal forces caused by a 1% wave for the both test set-ups (permeable and less permeable core).The left graph represents the storm waves (s_{0p} = 4%) and the right graph the swell waves (s_{0p} = 1.5%)

As illustrated in Fig. 4.14, core permeability significantly influences not only the uplift forces but also the horizontal forces acting on the structure. Similar to Fig. 4.13, Fig. 4.14 represents storm waves (left) and swell waves (right) separately. Contrary to the initial hypothesis—which expected a pronounced effect of permeability on uplift forces alone—the horizontal forces also reacted to changes in permeability. The behavior of horizontal forces contrasts with that of uplift forces: while reduced permeability diminished the uplift forces, it conversely resulted in an increase in horizontal forces. This behavior is observable in Fig. 4.14, where most of the dashed lines (representing lower permeability) are positioned above the solid lines (indicating higher permeability). The impact of permeability varies between storm waves and swell waves, with horizontal forces for storm waves increasing by an average of 47% and by 10% for swell waves. This increase in horizontal forces can be explained by the decreased capacity of the less permeable core to absorb incoming momentum and water. A core with lower permeability allows less water to infiltrate during wave impact, resulting in less water and momentum being absorbed within the core. Consequently, a greater portion of the incoming wave momentum and water is redirected upward along the slope toward the crown wall face. This results in higher wave run-up, leading to larger horizontal forces acting on the crown wall. In other words, the less permeable core cannot absorb as much of the incoming momentum and water, causing more of it to be directed toward the crown wall and increasing the horizontal force exerted. A parallel can be drawn with impermeable dikes, where this effect is more pronounced. There a complete conversion of wave momentum into run-up leads to significantly larger horizontal forces. Although the breakwater core is not entirely impermeable, and some wave momentum absorption and water infiltration occurs, the observed increase in horizontal forces can be explained by this reduced permeability, even if the effect is less pronounced than in fully impermeable structures.

Stability

Another point that will be analyzed is the stability of the crown wall and the influence of permeability on it. This is done by analyzing the stability tests discussed in section Section 4.5. For each wave condition, a stable weight was determined by iteratively adding weights to the crown wall. By following this procedure, the critical weight—the weight at which the crown wall is barely stable—can be obtained. These critical weights, for both wave steepnesses, are plotted in Fig. 4.15, again for both permeability levels, against the significant wave height.

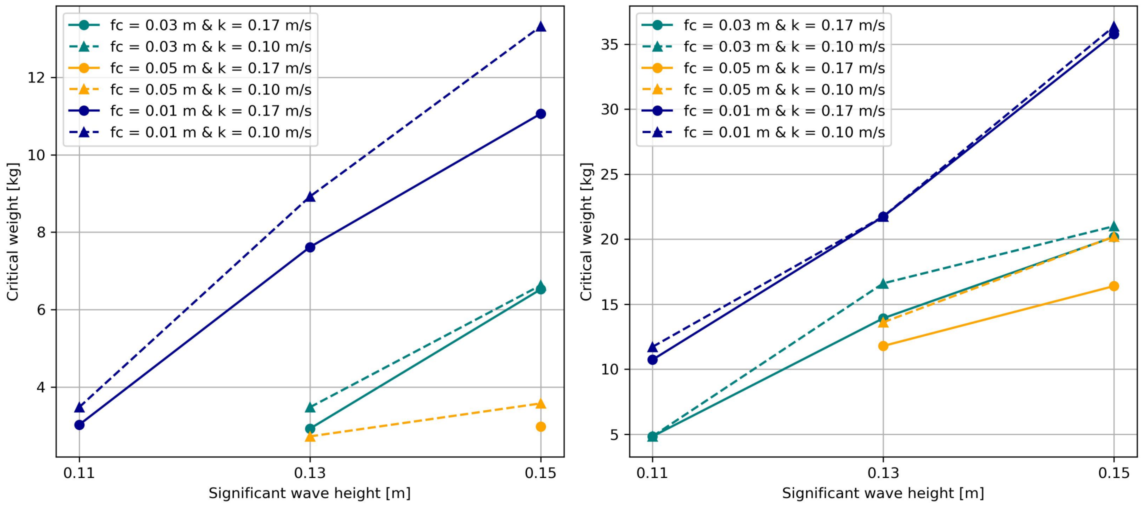

Figure 4.15: Critical weight for all conditions vs significant wave height. The left graph represents the storm waves (s_{0p} = 4%) and the right graph the swell waves (s_{0p} = 1.5%)

In Fig. 4.15, similar behaviour can be observed as with the horizontal pressures. In this scenario, the reduced permeability of the core necessitated an increase in the weight on the crown wall to reestablish stability. This also contradict the initial hypothesis, which stated that a lower critical weight would be required for a less permeable core, as it was expected that only the vertical forces would decrease, leading to a more stable crown wall. Instead, as illustrated in the graphs, a less permeable breakwater core led to a less stable crown wall. On average, the critical weight for storm waves had to be increased by 15% to remain stable, while for swell waves, it needed to be increased by 10%. This indicates that the permeability of the core material is crucial in determining the stability of the crown wall, as variations in permeability directly impact its stability.

Given the explanation provided earlier in Section 1.5 on the how the factor of safety is determined, it becomes evident that the stability of a crown wall is governed by the combination of vertical and horizontal forces. In contrast to the initial hypothesis, the observed phenomenon of decreased vertical forces, accompanied by a rise in horizontal forces, ultimately led to a diminished level of stability. The aforementioned outcome highlights the significance of horizontal forces, indicating that they might hold greater importance than vertical forces in the determination of stability. Experimental findings demonstrate that greater fluctuations in vertical forces, when coupled with an increase in horizontal forces, lead to diminished stability, underscoring the predominant influence of horizontal forces. The unforeseen outcome will be further examined in the subsequent Section 4.5.

Horizontal force reduction

Another topic investigated in this research is the reduction of horizontal forces as a result of increasing the amount of armour in front of the crown wall. In addition to the main configuration, referred to as set-up A, two alternative configurations, set-ups B and C, were tested. Set-up A, illustrated in Fig. 3.3 serves as a base case. Set-up B utilizes an extra armour layer on the crest while maintaining the crown wall at its original position. Set-up C uses the extra armour layer, and relocates the crown wall backwards to obtain a crest width of $3 * D_{n,50}$. Appendix H provides illustrations of all three set-ups, along with a brief explanation of the adjustments made in each set-up compared to the previous one.

Fig. 4.16 displays the force reduction for each set-up. The graph plots set-up used against the horizontal force. As in the preceding sections, the analysis will focus on the horizontal force caused by a 1% wave, as this is less prone to outliers than the 0.1% horizontal force. The graph shows that the largest reduction in horizontal force acting on the crown wall is due to the displacement of the crown wall.

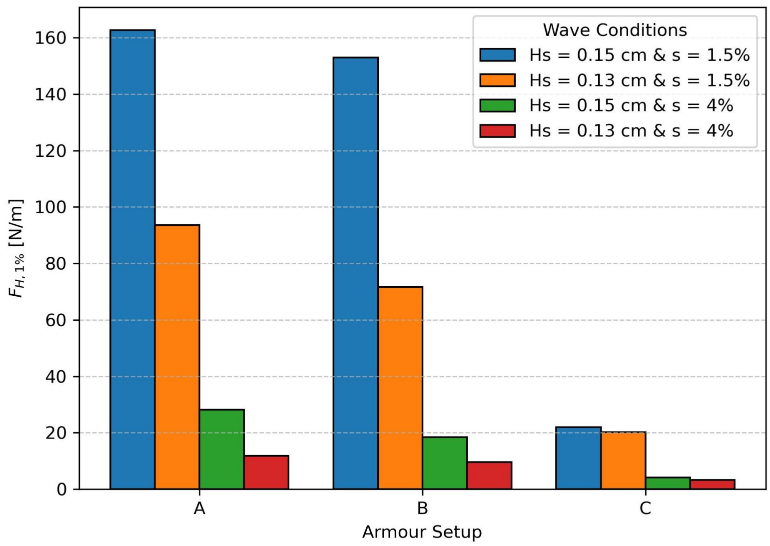

Figure 4.16: Horizontal forces (1%) per set-up

Table H.1 summarizes the data illustrated in Fig. 4.16. Both show that the set-up adaptations lead to reductions in the measured horizontal forces. The average force reduction from A to B is 20.64%, but the largest and more significant force reduction is from B to C, which averages 75.19%. This corresponds with the initial hypothesis, which stated that the adaptation from B to C would lead to a larger horizontal force reduction. This stems from two reasons. The first is that in the modification from B to C, more armor material is added in front of the crest wall compared to the modification from A to B. The extra material allows the incoming wave to dissipate more energy. Additionally, the wall is positioned further back, meaning that the virtual run-up wedge — as described by Pedersen and illustrated in Fig. 2.4 — must travel a greater distance to reach the wall. Consequently, it does not directly impact the crest wall, thereby avoiding a dynamic impact and only developing a hydrostatic pressure. This effect is particularly noticeable under smaller wave conditions (storm waves with H_s = 0.13 m), where the real run-up wedge, already small, does not directly reach the wall.

Vertical force limit

Since the entire research distinguishes between storm and swell waves, this section also explores whether different relations can be established for each. It examines whether a relationship can be derived, based on the current data, that describes the development of vertical forces as a function of the relative freeboard, and if so, whether a limit of relative freeboard can be defined beyond which no vertical forces will occur. This analysis is presented in Fig. 4.17

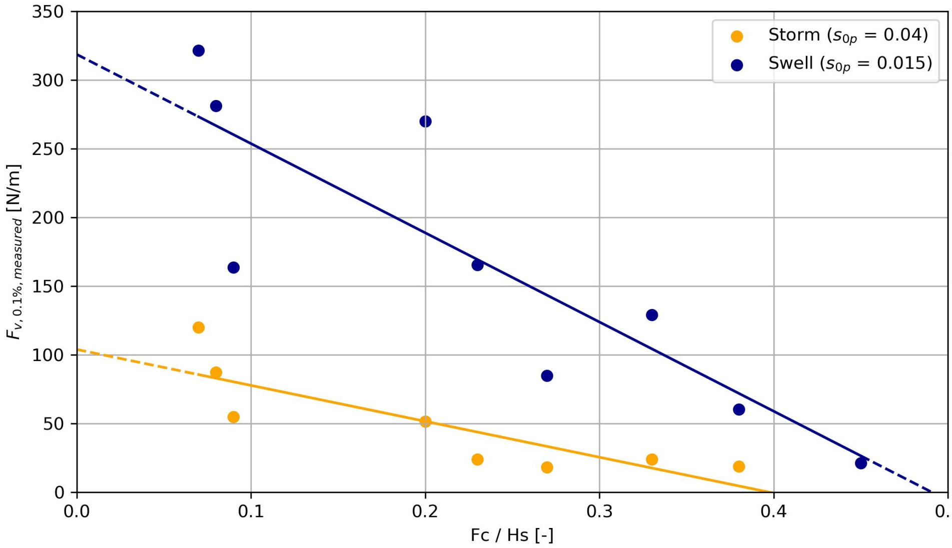

Figure 4.17: Maximal vertical forces, with storm and swell waves plotted separately.

As demonstrated in previous sections, also in this section a clear difference between storm and swell waves can be seen, which is entirely consistent with the earlier findings. In the graph, the solid line represents a fit through the data obtained from the tests, while the dashed line is derived through extrapolation. This allows for a clear determination of the limit, after which no vertical forces will be measured.

As is clear from Fig. 4.17 and the tables below, storm waves exhibit a lower limit compared to swell waves. This difference can be explained by the difference in wavelength, which is far greater for swell waves, resulting in less steep waves. Due to their longer wavelength, swell waves carry more energy and momentum. As a result, these waves penetrate further through the porous medium, which explains why vertical forces are still measured at higher relative freeboard levels, leading to a higher limit compared to storm waves.

Swell waves $s_{0p} = 0.015$	
$F_V[N/m]$	**Condition**
0	$\frac{F_c}{H_s} > 0.49$
$-650\frac{F_c}{H_s} + 318.7$	$\frac{F_c}{H_s} \leq 0.49$

Table 4.1: Lower limit, when no vertical forces are measured for storm waves

Storm waves $s_{0p} = 0.04$	
$F_V[N/m]$	**Condition**
0	$\frac{F_c}{H_s} > 0.4$
$-261\frac{F_c}{H_s} + 103.9$	$\frac{F_c}{H_s} \leq 0.4$

Table 4.2: Lower limit, when no vertical forces are measured for swell waves

4.3. Comparison to existing methods

This section compares the existing methods, as outlined in the literature research, with the measurements from the model tests. The comparative analysis starts with the uplift forces, as shown in Fig. 4.18, followed by the horizontal forces.The main goal of this analysis is to compare the 0.1% forces predicted by each method with the 0.1% forces obtained from the relation, as outlined in Appendix D and illustrated in Fig. D.1. This relation removes the outliers; therefore, this approach enables a more precise comparison between both forces. Based on the performance of these methods, conclusions are drawn.

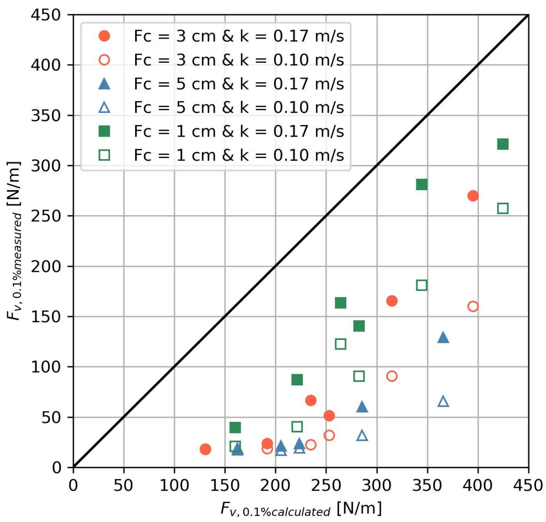

(a) Pedersen (1996)

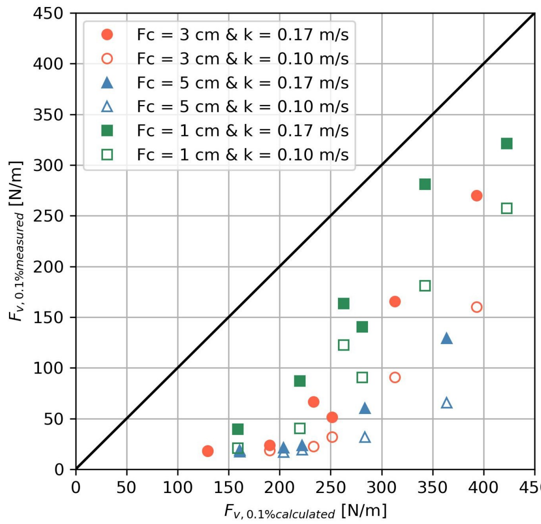

(b) Nørgaard et al. (2013)

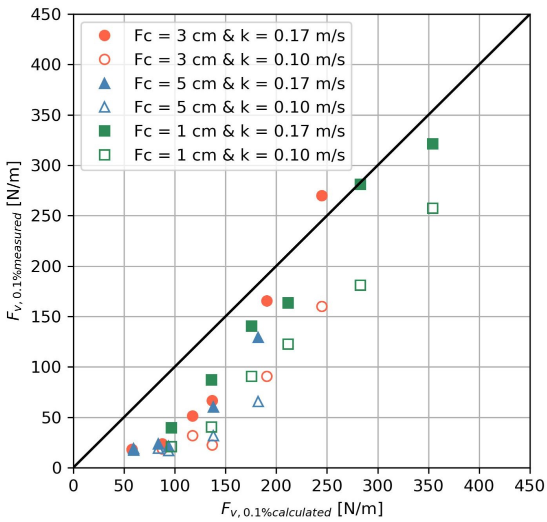

(c) van Gent and van der Werf (2019)

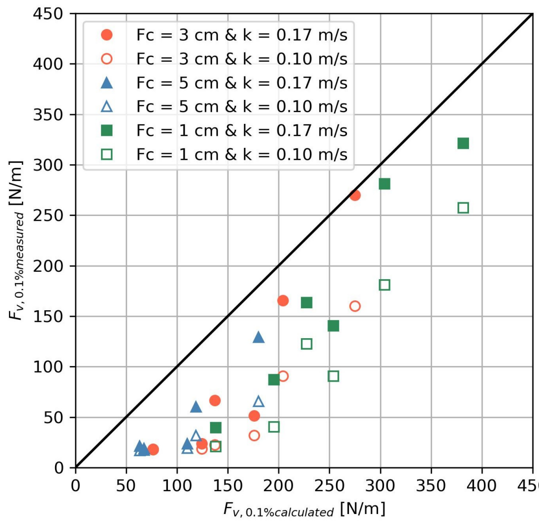

(d) Veringa (2023)

Figure 4.18: Comparison between measured and calculated vertical forces ($F_{v,0.1\%}$)

Fig. 4.18 presents a comparison between the existing methods for estimating uplift forces and the measured data from the testing campaign. In all four graphs, the black diagonal line represents perfect alignment between the estimated and measured data. The forces are categorized per freeboard level, with a distinction made between forces from the permeable core and those from the less permeable core. In Fig. 4.18a and Fig. 4.18b it is evident that both methods do not correspond with measured uplift forces. Therefore, the conclusions of Bekker (2017) and Veringa (2023) are further confirmed, as they stated that Pedersen and Norgaard's methods were overly conservative. Fig. 4.18c and Fig. 4.18d, illustrate the performance of the methods of van Gent and van der Werf (2019) and Veringa (2023). Both demonstrate a closer alignment between the estimated and measured data, with the method proposed by van Gent and van der Werf (2019) providing the most accurate estimations of uplift forces, though Veringa's method is not far behind. The graphs indicate that the error increases as the freeboard becomes larger, suggesting that the accuracy of these methods diminishes with higher freeboard values. Although this trend may not be entirely consistent across all methods, it is a noticeable phenomenon in the results, suggesting a potential dependency that could serve as an addition to the existing methods. Additionally, the influence of permeability is clearly observed, with lower permeability resulting in lower uplift forces.

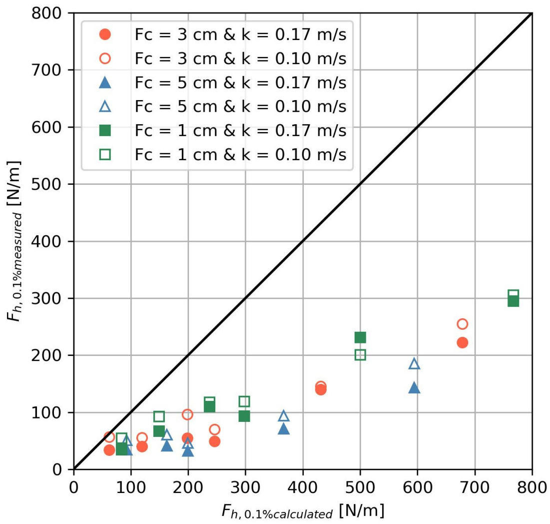

(a) Pedersen (1996)

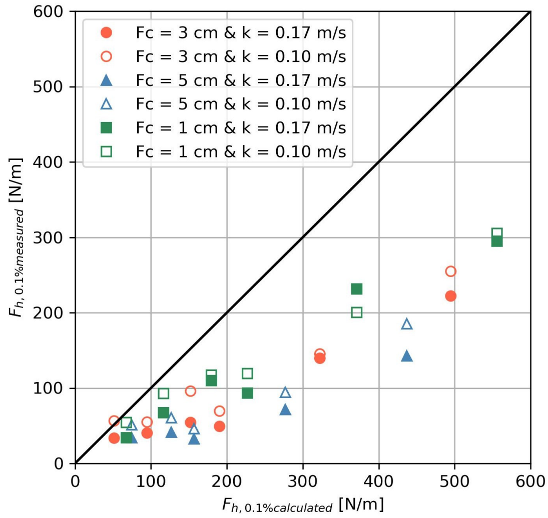

(b) Nørgaard et al. (2013)

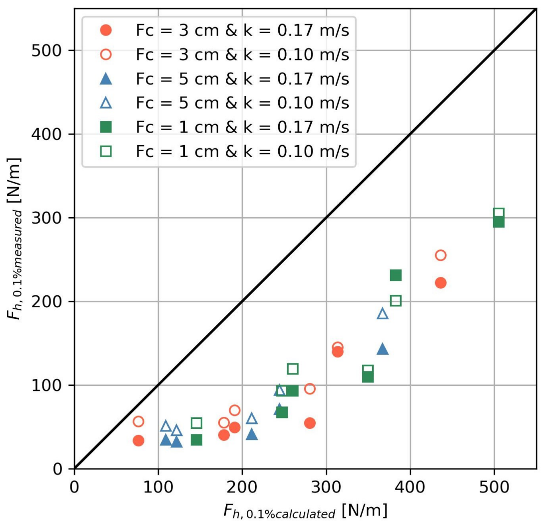

(c) van Gent and van der Werf (2019)

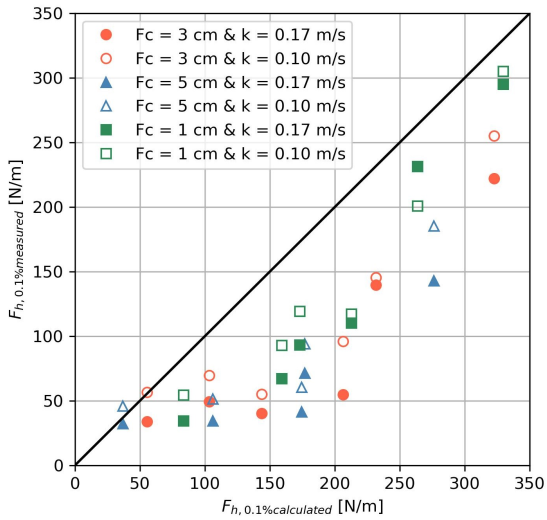

(d) Molines et al. (2018)

Figure 4.19: Comparison between measured and calculated horizontal forces ($F_{h,0.1\%}$)

Fig. 4.19 presents a similar comparison for the horizontal forces. In this figure, the methods of Pedersen (1996), Nørgaard et al. (2013), van Gent and van der Werf (2019) and Molines et al. (2018) are evaluated against the measurements. Consistent with the comparison of vertical forces, the methods proposed by Pedersen (1996) and Nørgaard et al. (2013) do not match the measured horizontal forces. In contrast, the method by Molines et al. (2018) appears to provide the most accurate force estimation. The graphs further indicate that the error tends to increase with higher freeboard values, similar to the trend observed in Fig. 4.18. Moreover, the influence of permeability is also depicted, illustrating an opposite effect: higher horizontal forces are observed for the less permeable breakwater core, as measured during the testing campaign.

The analysis identifies which calculation methods show the greatest and least alignment with the measured forces. For the vertical forces, the method by Van Gent aligns most closely with the measurements, while for the horizontal forces, the method by Molines shows the closest resemblance. However, as discussed in Chapter 2, the underlying physical idea on which the method of Molines is based is contradictory. The method predicts that significant overtopping leads to high forces, and conversely, low overtopping leads to low forces; however, the opposite effect is generally expected. Despite this, the Molines method performs the best, suggesting that the measurements fall within its specific validity ranges, leading to reasonably accurate results and making it the most suitable method for predicting these forces.

Due to this inconsistency, the decision was made to exclude the Molines method and instead propose an addition to the second-best method: the method developed by Van Gent.The CIRIA et al. (2007) suggests that the Pedersen method should be used, noting that *'Evaluation of these formulations (Camus Brana and Flores Guillen, 2005) has shown that the Pedersen method is the most reliable for the estimation of the maximum horizontal forces, uplift forces, and tilting moments of a sea state.'* As a result, Pedersen's method remains the most widely used approach for designing crown walls on rubble mound breakwaters, highlighting the necessity to develop an addition to this method, to improve its applicability for scenarios with non-zero freeboard.

4.4. Compensation to existing methods

As elaborated in the previous section, an addition will be developed for both horizontal and vertical force estimation methods to ensure that the methods are applicable to the measured data. These additions are first developed for the Van Gent method, which demonstrated the closest alignment with the measurements for both vertical and horizontal forces. Subsequently, an addition was also developed for the most widely used method, Pedersen, for both vertical and horizontal forces.

Compensation to van Gent

The comparison in the previous section revealed a possible dependency on the freeboard level. Therefore, it was investigated whether an addition could be developed that accounts for this effect, allowing the method to compensate for it and better align with the measurements.

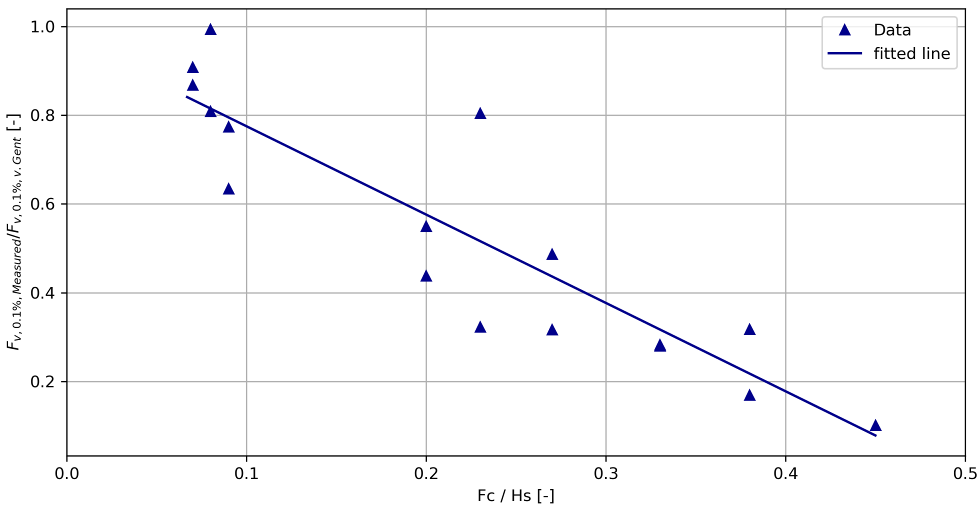

Figure 4.20: Relative freeboard vs. Vertical reduction coefficient for the van Gent method.

The possible dependency is examined in Fig. 4.20, where the relative freeboard (x-axis) is plotted against the ratio of measured to predicted forces using the Van Gent method. This ratio indicates the necessary reduction to the predicted force, to match the measured force accurately. The graph shows a negative trend that diminishes with increasing relative freeboard, providing a basis for a correction factor that adjusts the method of Van Gent accordingly. Additionally, no significant difference is observed between the two wave steepnesses, likely because the effect of wave steepness is already accounted for within the method, as shown in Eq. (2.29). The fit, illustrated in Fig. 4.20, is given in Eq. (4.1).

$$\gamma_{vertical} = \frac{F_{v,0.1\%,Measured}}{F_{v,0.1\%,v.Gent}} = -1.99\frac{F_c}{H_s} + 0.97 \quad \text{with } R = 0.91 \tag{4.1}$$

Upon closer examination of the method, it can be concluded that the effect of the freeboard is already accounted for within the method. This makes the dependency on the relative freeboard somewhat redundant. However, the difference between the predicted and measured forces is likely due to the different experimental set-ups used. The forces predicted by the method are almost always higher than the measured ones, which could be attributed to differences in the core permeability. The core used in the research of Van Gent had a narrow grading, resulting in higher permeability, whereas the core used in these model tests had a broader grading, leading to lower permeability. This difference in permeability could account for the observed discrepancies between the method and the measurements, as this influence has been tested, and similar effects have been measured in this study. The table below provided the application ranges within which the correction factor can be used with confidence.

All waves $s_{0p} = 0.015 - 0.04$	
$\gamma_V [-]$	**Condition**
$-1.99\frac{F_c}{H_s} + 0.97$	$0.07 \leq \frac{F_c}{H_s} \leq 0.46$
0	$\frac{F_c}{H_s} > 0.46$

Table 4.3: Application ranges for $\gamma_{vertical}$

Similar approach is used to develop a correction for the horizontal forces in the van Gent method. Fig. 4.21 presents a similar illustration. An important difference from the correction for the vertical force is that the method does not account for freeboard, making the dependency on freeboard more reasonable. Furthermore, the data illustrates different values for each wave steepness, necessitating a separate fit for each steepness.

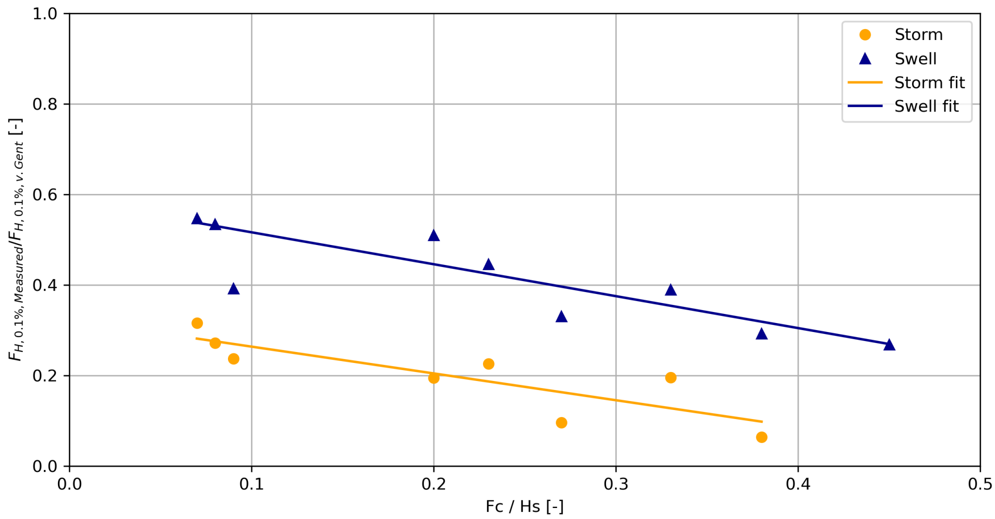

Figure 4.21: Relative freeboard vs. horizontal reduction coefficient for the van Gent method.

The functions for both developed correction factors is given below, followed by the range of applicability.

$$\begin{aligned} \gamma_{horizontal,swell} &= \frac{F_{H,0.1\%,Measured}}{F_{H,0.1\%,v.Gent}} = -0.71\frac{F_c}{H_s} + 0.59 \quad \text{with } R = 0.84 \\ \gamma_{horizontal,storm} &= \frac{F_{H,0.1\%,Measured}}{F_{H,0.1\%,v.Gent}} = -0.59\frac{F_c}{H_s} + 0.32 \quad \text{with } R = 0.85 \end{aligned} \tag{4.2}$$

The new aspect, compared to the vertical force correction, is the difference between storm waves and swell waves. It is evident that storm waves require a larger correction to align with the measurements. Therefore, it can be concluded that freeboard has a greater influence on storm waves than on swell waves.

Swell waves $s_{0p} = 0.015$	
$\gamma_H[-]$	**Condition**
$-0.71\frac{F_c}{H_s} + 0.59$	$0.07 \leq \frac{F_c}{H_s} \leq 0.46$
0	$\frac{F_c}{H_s} > 0.46$

Table 4.4: Application ranges for $\gamma_{horizontal,swell}$

Swell waves $s_{0p} = 0.04$	
$\gamma_H[-]$	**Condition**
$-0.59\frac{F_c}{H_s} + 0.32$	$0.07 \leq \frac{F_c}{H_s} \leq 0.38$
0	$\frac{F_c}{H_s} > 0.38$

Table 4.5: Application ranges for $\gamma_{horizontal,storm}$

Last step is to apply the new correction factor on the design method and compare it with the measurements, to test its effectiveness. To enable this, Fig. 4.22 has been created. In the graph, better alignment is illustrated between the predicted and measured data. Thus, the new correction factor performs quiet well.

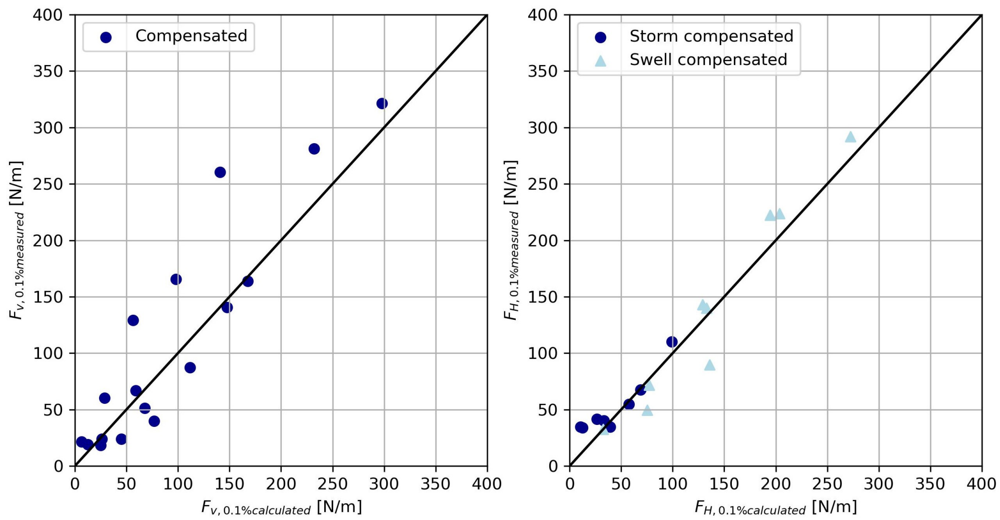

Figure 4.22: Comparison of measured and estimated forces using Eqs. (4.1) and (4.2).

Compensation to Pedersen

As concluded in the last section, next to the correction on the van Gent method, the Pedersen method also necessitates a correction to include the effect of freeboard. Similar approach has been utilized to develop this factor, since Section 4.3 highlighted the freeboard level as potential dependency that could serve as an addition on Pedersen.

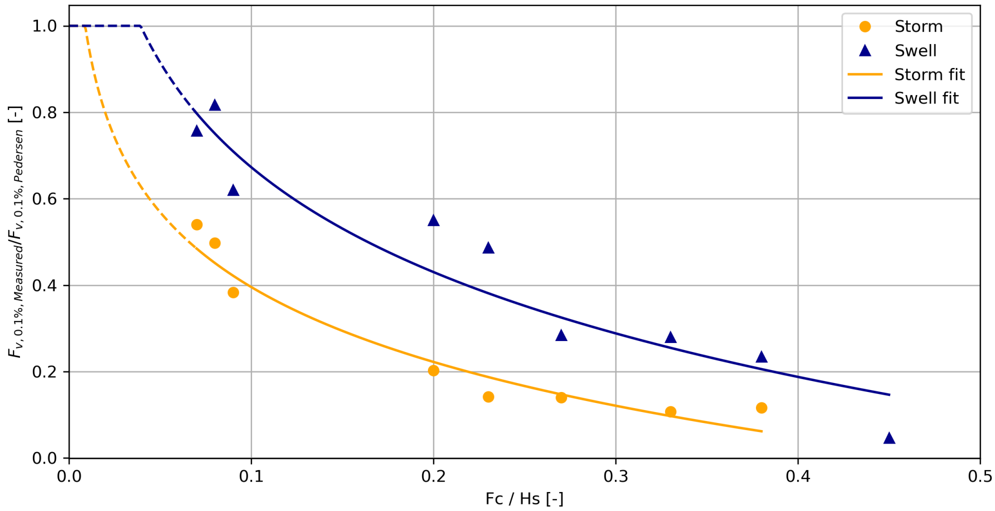

Figure 4.23: Relative freeboard vs. Vertical reduction coefficientfor the Pedersen method.

In Fig. 4.23, the aforementioned dependency is illustrated, first doing the analysis for the vertical forces. Similar as Figs. 4.20 and 4.21, the x-axis represents the relative freeboard and the y-axis represents the ratio between the measured and the calculated force by Pedersen. A sufficiently accurate line can then be fitted through the data, allowing for the determination of a correction factor as addition to modify Pedersen's method, to include the relative freeboard. A distinction was made between storm and swell waves in this analysis, as Fig. 4.23 clearly demonstrates different trends between the two. Eq. (4.3) illustrates how the factor is derived, followed by the actual function for both storm and swell waves.

$$
\begin{aligned}
\gamma_{vertical,swell} &= \frac{F_{v,0.1\%,Measured}}{F_{v,0.1\%,Pedersen}} = -0.35 \ln\left(\frac{F_c}{H_s}\right) - 0.13 \quad \text{with } R = 0.95 \\
\gamma_{vertical,storm} &= \frac{F_{v,0.1\%,Measured}}{F_{v,0.1\%,Pedersen}} = -0.25 \ln\left(\frac{F_c}{H_s}\right) - 0.17 \quad \text{with } R = 0.98
\end{aligned}
\tag{4.3}
$$

Additionally, the ranges of application are based on the outer boundaries of the data; however, since no measurements have been conducted beyond these boundaries, no definitive conclusions can be drawn for those areas. For smaller relative freeboard situations, the dashed line provides an indication of possible trends, but no definitive statements can be made with certainty. The similar methodology was employed for the horizontal forces.

Swell waves $s_{0p} = 0.015$	
$\gamma_V[-]$	**Condition**
$-0.35ln(\frac{F_c}{H_s}) - 0.13$	$0.07 \leq \frac{F_c}{H_s} \leq 0.46$
0	$\frac{F_c}{H_s} > 0.46$

Table 4.6: Application ranges for $\gamma_{vertical,swell}$

Storm waves $s_{0p} = 0.04$	
$\gamma_V[-]$	**Condition**
$-0.25ln(\frac{F_c}{H_s}) - 0.17$	$0.07 \leq \frac{F_c}{H_s} \leq 0.38$
0	$\frac{F_c}{H_s} > 0.38$

Table 4.7: Application ranges for$\gamma_{vertical,storml}$

Identical fits through the data were created for the horizontal forces, as illustrated in Fig. 4.24. A comparison of these fits reveals two key differences. First, the linear fit provides a better match to the measured data than the logarithmic function used for the vertical forces. Furthermore, the correction needed to align the predicted forces with the measured forces, is larger for the horizontal forces than for the vertical forces. Moreover, the trend shown in Fig. 4.23 appears to approach a value of 1 for all smaller freeboard values, which could suggest that the Pedersen method is effective in predicting the force for zero freeboard situations. However, this was not tested in the current study, and therefore, no definitive conclusions can be drawn from the test results. The second observation is the broader spread in the fit of Fig. 4.24, particularly for storm and swell waves, which, while larger, remains within a reasonable range. This observation is supported by the R factor (coefficient of determination). The increased variability in horizontal forces can likely be attributed to the differing physical processes that govern horizontal and vertical loading on the crown wall. Vertical forces result from a somewhat uniform loading of the wall, from below by a water column, leading to a distribution almost similar to hydrostatic pressure. This uniformity likely explains the smaller variation in the reduction ratio for vertical forces.

In contrast, horizontal forces are subject to wave impact, a dynamic process heavily influenced by turbulence and the nature of wave breaking. In some cases, particularly with smaller waves or those involving a larger freeboard, the wave does not directly impact the crown wall but instead reaches it through run-up, further contributing to the observed variation in horizontal force data. The variability in these loading mechanisms results in a greater spread, as demonstrated in Fig. 4.24.

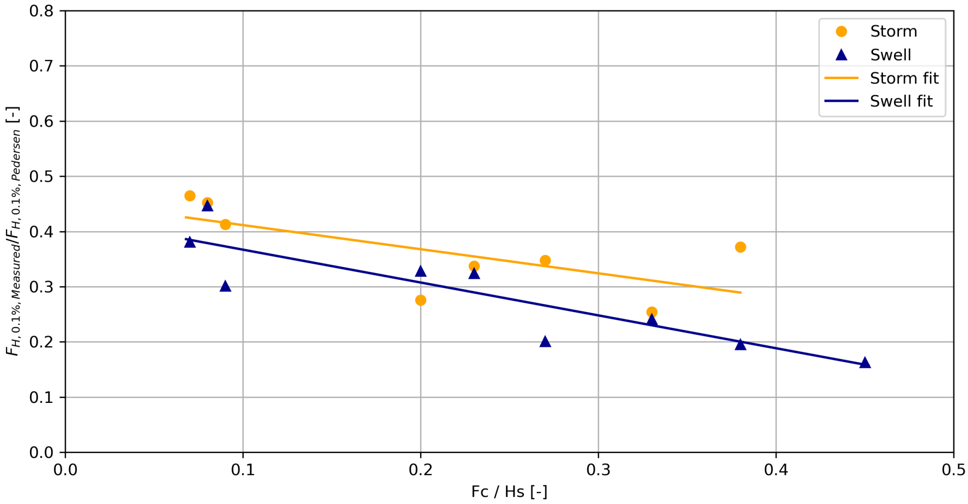

Figure 4.24: Relative freeboard vs. Horizontal reduction coefficient for the Pedersen.

The functions for both created fits are given below, followed by the range of applicability in Tables 4.8 and 4.9.

$$\begin{aligned}\gamma_{horizontal,swell} &= \frac{F_{h,0.1\%,Measured}}{F_{h,0.1\%,Pedersen}} = -0.60\frac{F_c}{H_s} + 0.43 \quad \text{with } R = 0.88 \\ \gamma_{horizontal,storm} &= \frac{F_{h,0.1\%,Measured}}{F_{h,0.1\%,Pedersen}} = -0.44\frac{F_c}{H_s} + 0.46 \quad \text{with } R = 0.79\end{aligned} \tag{4.4}$$

Swell waves $s_{0p} = 0.015$	
$\gamma_H[-]$	**Condition**
$-0.60\frac{F_c}{H_s} + 0.43$	$0.07 < \frac{F_c}{H_s} \leq 0.46$
0	$\frac{F_c}{H_s} > 0.46$

Table 4.8: Application ranges for $\gamma_{horizontal,swell}$

Storm waves $s_{0p} = 0.04$	
$\gamma_H[-]$	**Condition**
$-0.44\frac{F_c}{H_s} + 0.46$	$0.07 < \frac{F_c}{H_s} \leq 0.38$
0	$\frac{F_c}{H_s} > 0.38$

Table 4.9: Application ranges for $\gamma_{horizontal,storm}$

Final step in comparing the newly developed factor with existing design methods is to assess its effectiveness in estimating wave forces. To validate this, graphs similar to those in Fig. 4.18 have been created, intended to confirm an improved fit in line with the modified Pedersen method.

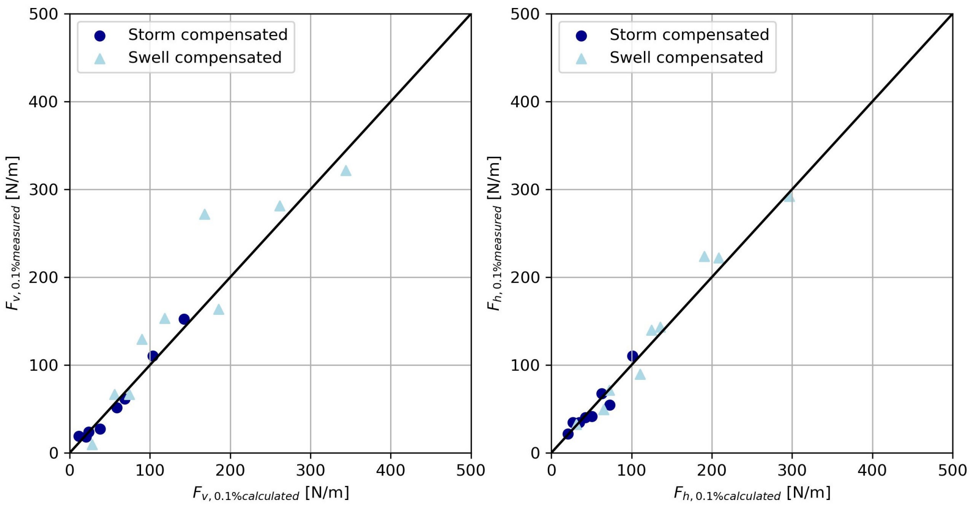

Figure 4.25: Comparison of measured and estimated forces using Eqs. (4.3) and (4.4).

In the graph, a quiet strong alignment can be seen between the expected forces and the measured data, where the expected forces have been compensated with the reduction factor. Therefore, it can be concluded that the new factor, which accounts for the effect of freeboard, performs quiet well when predicting the forces. Incorporating this factor will mostly result in lower predicted forces on the crown wall.

4.5. Factor of Safety

This analysis evaluates the stability of the crown wall during the physical model tests, where stability is assessed as a binary condition: either failure or stability under specific wave conditions, contingent on the wall's weight. As detailed in Section 3.4, weights were incrementally added to the crown wall to determine the critical weight, defined as the weight at which the wall remains stable. A total of 36 critical weights were identified using this procedure, facilitating the stability analysis through the evaluation of the factor of safety, as outlined in Section 1.1. The relevant equation, incorporating the critical weight (F_G), forces measured by pressure transducers (F_h and F_v) and friction factor (μ_s), is reiterated below:

$$\text{Factor of Safety}(t) = \frac{\mu_s(F_G - F_V(t))}{F_H(t)}$$

The analysis focused on the moment of failure, which theoretically occurs when the factor of safety (FoS) is approximately 1. To achieve this condition, the friction factor was iteratively adjusted to obtain an FoS close to 1 for the smallest wave condition. This calibrated friction factor was then uniformly applied across all wave conditions, enabling the analysis of the minimal FoS within the time series, which could be either above or below 1. The forces corresponding to this minimal FoS were subsequently used in the following analysis. Importantly, while tuning the friction factor changes the value of the FoS, it does not affect the location where the minimal FoS occurs or the forces leading to this minimal FoS. The analysis in this chapter concentrates on the 0.1% forces, as these were the forces that resulted in failure, as opposed to the 1% forces, which were used in the previous chapter. All figures that are shown in the remainder of this chapter are therefore made based on the 0.1% wave (critical wave).

Fig. 4.26 illustrates the temporal evolution of the factor of safety following the impact of a critical wave. The minimum factor of safety, marked by the orange dot, occurs between the two force maxima, highlighting the importance of considering the combination of these forces rather than their individual maxima. The vertical lines in the figure denote the time lag between the occurrences of these maxima. For illustrative purposes, and specifically to create Figs. 4.26 and 4.27, the friction factor was tuned so that the FoS is approximately 1.

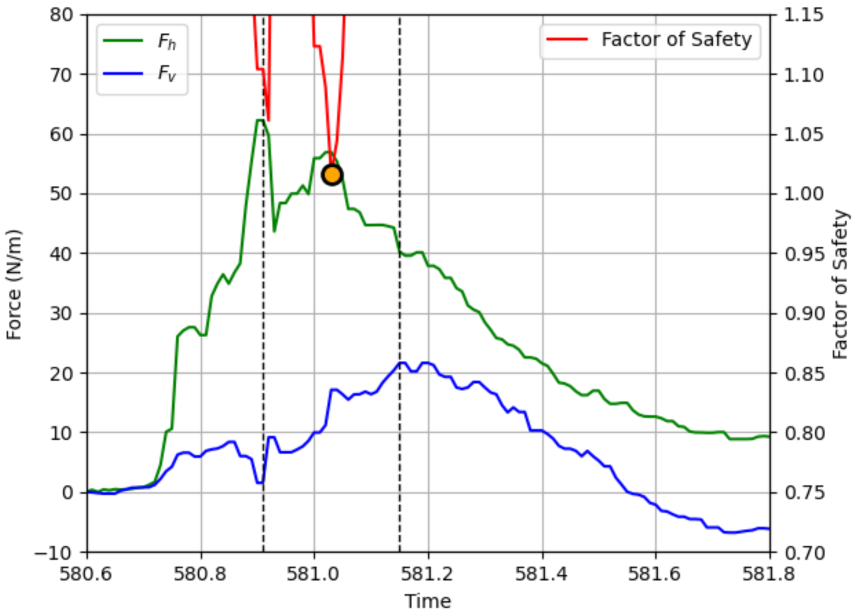

Figure 4.26: Temporal evolution of the factor of safety during the impact of the critical wave.

To further understand the moment of failure, we analyze the temporal relation between both force maxima relative to the point of failure. Three failure scenarios are identified: failure occurring at the maximal horizontal force, at the maximal vertical force, or between these force maxima, as illustrated in Fig. 4.26. The findings indicate that failure consistently occurs within the interval between the maximum horizontal and vertical forces, herein referred to as the *failure domain*. To analyze the influence of permeability on stability, we examine both the timing of failure within this domain and the duration of the failure domain itself, characterized by the time lag between the force maxima.

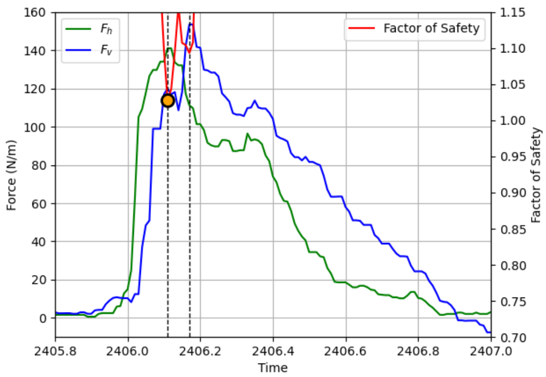

(a) Failure at the maximal horizontal force

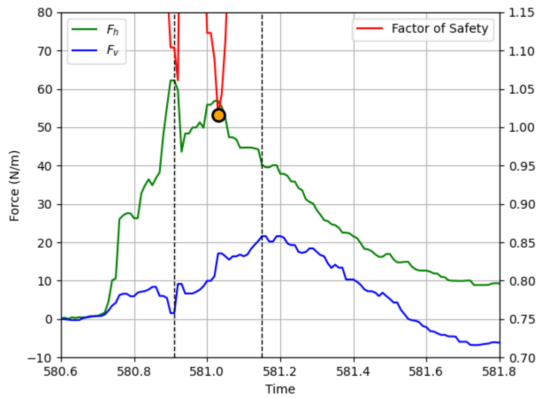

(b) Failure in between both force maxima

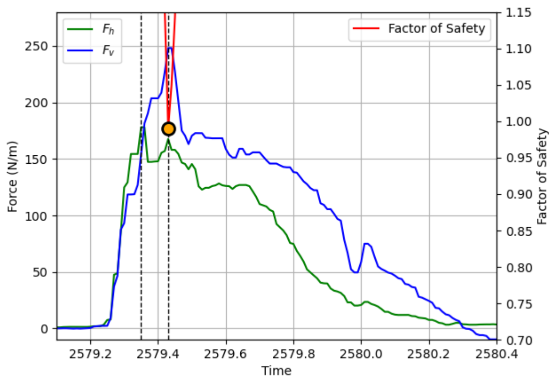

(c) Failure at the maximal vertical force

Figure 4.27: Three failure categories.

Fig. 4.28 shows the influence of permeability on the former mentioned criteria. The x-axis in the figure denotes the normalized moment of failure, with a value of 0 corresponding to failure at the maximal horizontal force, and a value of 1 indicating failure during the maximal vertical force. Values between 0 and 1 illustrate that failure occurred at a point in between these two force maxima. The y-axis represents the time lag between the two force maxima, or the duration of the failure domain. In the graph, solid points represent the permeable core, while hollow points indicate the less permeable core. Different colors are used make distinctions between various freeboard levels. A detailed version of this graph, featuring separate plots for each freeboard level, can be found in Appendix I.

The graph reveals the significant influence of permeability on the timing and nature of failure. For the permeable core, a larger portion of the failure events occurs later in time, closer to the maximal vertical forces. Except for the smallest freeboard levels, which fails at one of both force maxima. In contrast, the less permeable core - hollow icons -shows a larger portion of failures occuring earlier in time. This shift in moments of failure can solely be attributed to the change in permeability. Moreover, the hollow points' display higher values, demonstrating that the less permeable core has a larger time lag between both force maxima. This observation is consistent with the conclusions reached in Section 4.2.

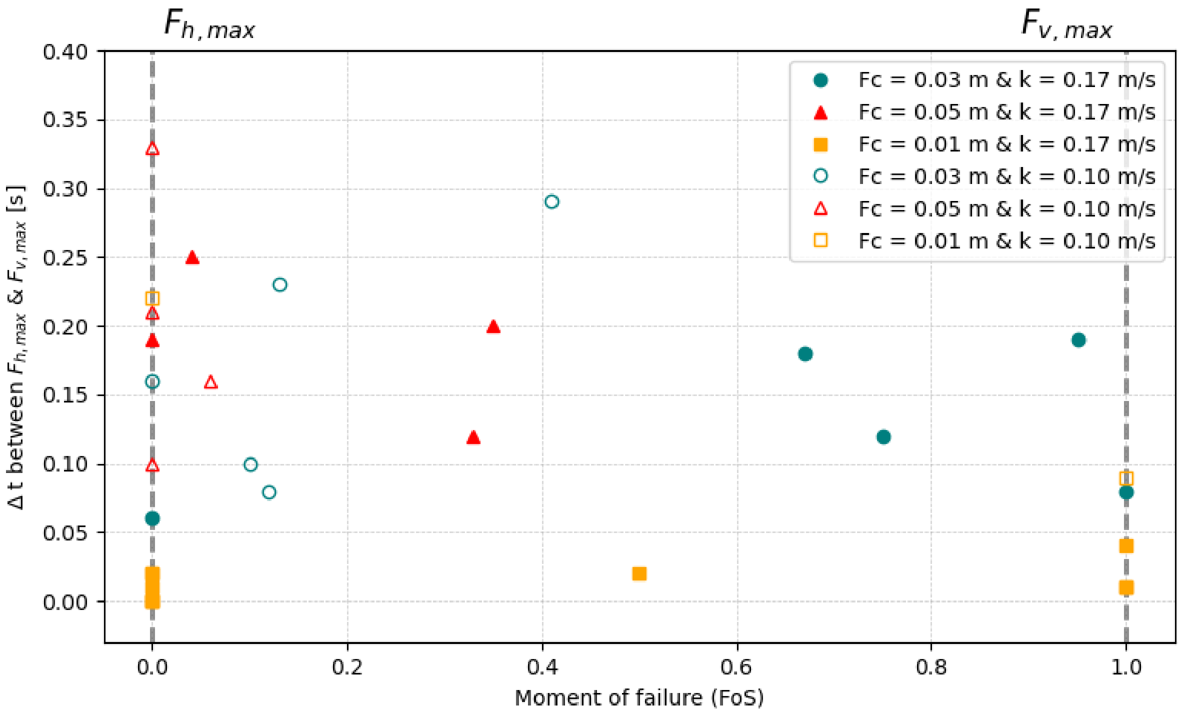

Figure 4.28: Moment of failure for all test conditions.

In analyzing the interplay of forces resulting in failure, it has traditionally been assumed that the crown wall fails when subjected to both peak forces simultaneously. However, as demonstrated in Fig. 4.26, failure is driven by a combination of both forces - or when one of them reaches its peak value - rather than when both forces are at their peak simultaneously. The factor of safety, representing this combination, reaches its lowest value at the moment of failure. Fig. 4.26 illustrates that failure does not occur at the simultaneous occurrence of peak forces, but rather when one of the forces is at its maximum value while the other is not, or between both maxima. This misunderstanding is an important factor contributing to the tendency to over-dimension crown walls and underscores the importance of considering combined loading conditions rather than evaluating both peak forces alone.

The difference between the described forces can be further analyzed through Fig. 4.29, where the relative freeboard is plotted against the ratio of the maximal uplift force and uplift force at the moment of failure (minimal Factor of safety). Veringa (2023) also evaluated this ratio and as discussed in Chapter 2 and Fig. 2.6, proposed a correction factor to account for this effect. Veringa (2023) refers to it as a correction for the time lag between the forces, which increases with higher freeboard levels. Despite different terminologies, both represent the same underlying principle.

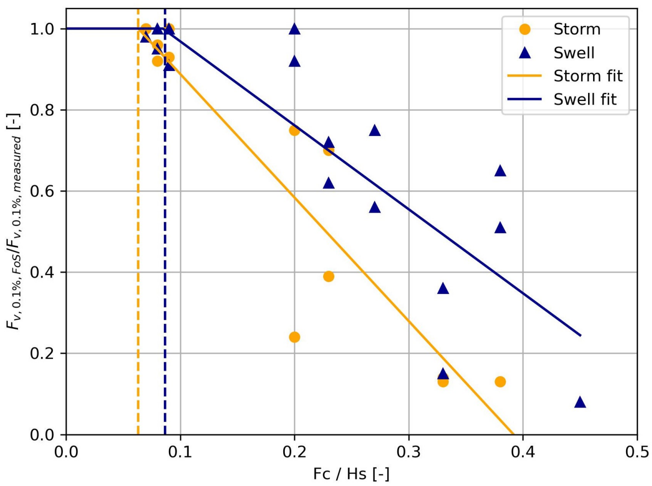

Figure 4.29: Relative freeboard vs. ratio of maximal vertical force and the force of failure.

In Veringa (2023) no distinction is made between storm and swell waves. Nevertheless, the test results presented in Fig. 4.29, reveal that this distinction is significant. This is apparent by the ability to plot two separate lines through the data, clearly indicating a difference between the two wave types. This implies that less steep waves exert larger forces, both horizontal and vertical, compared to steep waves. The fitted lines through the data are presented below, with the ranges of validity discussed at the end of the section.

$$\begin{aligned} \gamma_{FoS,Swell} &= \frac{F_{v,0.1\%,FoS}}{F_{v,0.1\%,measured}} = -2.03\frac{F_c}{H_s} + 1.16 \quad \text{with } R = 0.87 \\ \gamma_{FoS,Storm} &= \frac{F_{v,0.1\%,FoS}}{F_{v,0.1\%,measured}} = -3.01\frac{F_c}{H_s} + 1.19 \quad \text{with } R = 0.93 \end{aligned} \tag{4.5}$$

Furthermore, an analysis was conducted to determine whether permeability influences this ratio. The analysis, is illustrated in Fig. 4.30, where a graph similar to Fig. 4.29 was constructed. In the graph distinction was made between the two different cores. In the graph nearly identical lines could be fitted through the data points, suggesting that permeability does not have an impact on the correction factor mentioned before. Thus, permeability has an effect on the overall magnitude of the measured forces, but it does not influence the proportion between them, as is illustrated in Fig. 4.30.

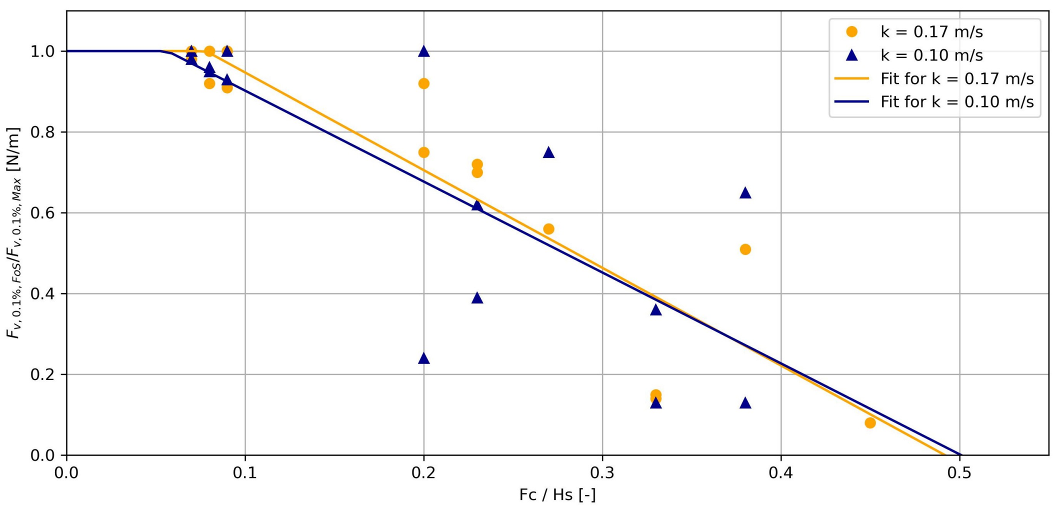

Figure 4.30: Permeability comparison

This effect is both surprising and interesting, particularly since the analysis in Section 4.2 has shown that the maximum uplift forces is affected by the core permeability. Although permeability affects the uplift forces, the ratio between the maximum uplift force and the uplift force at maximum instability remains consistent. This highlights the importance of horizontal forces at the point of failure, potentially even surpassing the significance of uplift forces, as was mentioned in an earlier section and has now been verified.

Comparing Fig. 2.6 with Fig. 4.29 it becomes evident that both graphs exhibit a negative correlation, where the proposed correction factor decreases for increasing freeboard. Thus, the correction factor proposed by Veringa (2023) performs fairly well. However, an important distinction can be made between both graph. In Fig. 2.6, for a F_C/H_s > 0, the fit begins to decrease, reaching a minimal value at F_C/H_s = 0.5. This effect is not observed in Eq. (4.5), where the influence of increasing freeboard on force reduction is not evident until F_C/H_s > 0.06, as illustrated by the horizontal line at the beginning of the graph. Consequently, it can be concluded that the effect of increasing freeboard is only noticeable after exceeding a certain threshold, with different values for both storm and swell waves.

Analysis of the video records, made during the tests, confirmed that this phenomenon is a direct result of the internal water level set-up within the permeable breakwater core. After wave impact, wave transmission through the breakwater develops an internal water level gradient within the permeable core, resulting in a slightly higher water level on the lee side of the structure compared to the sea side. This internal gradient induces flows within the breakwater. As the freeboard increases, the effect of this internal slope becomes more pronounced in the initial few centimeters due to the higher internal water level relative to the external level. This observation is supported by the video analysis, which showed that for the smallest freeboard situations, the base of the crown wall remained wet, indicating that the base freeboard effect was present at the smallest freeboard levels. The influence of this internal slope on the correction factor from maximum force to stability force, as depicted in Fig. 4.29, is noticeable for small relative freeboard values between 0 and 0.06. For values greater than 0.06, this effect becomes less pronounced, and the correction factor increases, beginning to have a significant impact. In these scenarios, the video analysis revealed that significant dry portions of the crown wall base became visible, with the extent of the dry area increasing as the freeboard increased.

Swell waves $s_{0p} = 0.015$	
γ_{Fos} [-]	**Condition**
1	$\frac{F_c}{H_s} < 0.09$
$-2.02\frac{F_c}{H_s} + 1.18$	$0.09 \geq \frac{F_c}{H_s} \leq 0.46$
0	$\frac{F_c}{H_s} s_{0p} \geq 0.46$

Table 4.10: Application ranges for $\gamma_{Fos,Swell}$

Storm waves $s_{0p} = 0.04$	
γ_v [-]	**Condition**
1	$\frac{F_c}{H_s} \leq 0.06$
$-3.04\frac{F_c}{H_s} + 1.19$	$0.06 > \frac{F_c}{H_s} \leq 0.39$
0	$\frac{F_c}{H_s} \geq 0.39$

Table 4.11: Application ranges for $\gamma_{Fos,Storm}$

Horizontal configurations

The effect of the three different horizontal configurations on stability has also been studied. Consistent with the analysis above, the forces corresponding to the minimal factor of safety are compared across each configuration, and the moment of failure is examined, including the time lag between the two force maxima.

First, the forces at the minimal factor of safety are analyzed. Fig. 4.31a presents the horizontal forces at this instance for all three configurations. Similar to Fig. 4.16, which illustrates the total maximum forces, the largest reduction is observed when shifting from configuration B to C. While individual differences can be seen per wave condition between configurations A and B, the average force remains largely unchanged. A similar pattern is evident for the vertical forces shown in Fig. 4.31b, where there is almost no change from configuration A to B, except in the case of steep storm waves. However, the most significant reduction occurs when shifting from configuration B to C. This suggests that altering the configuration from B to C, by moving the crown wall further back, significantly increases its stability.

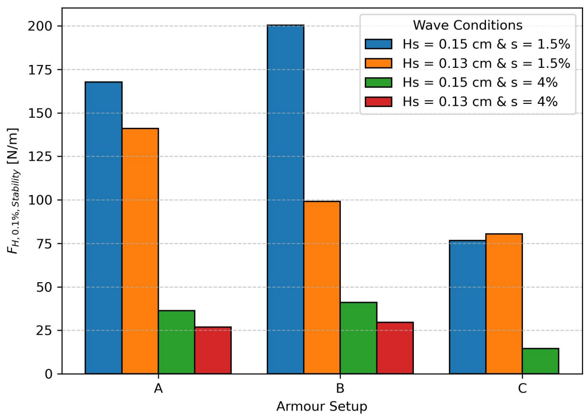

(a) Horizontal force at the minimal factor of safety

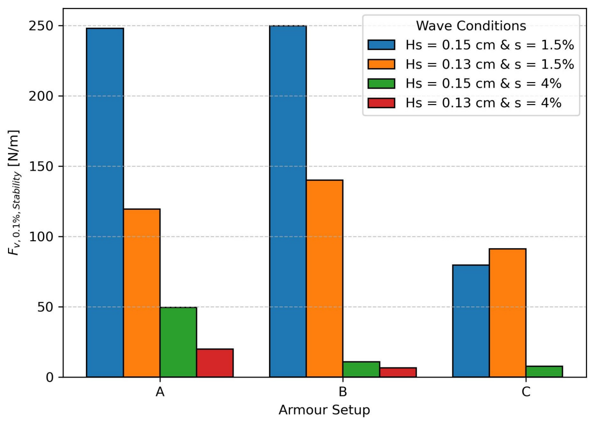

(b) Vertical force at minimal factor of safety

Figure 4.31: Forces at minimal factor of safety, for all configurations

Another point that can be analyzed is the timing of failure relative to the force maxima, by creating a similar illustration as Fig. 4.28. In Fig. 4.32 the x-axis represents the normalized moment of failure and the y-axis the time lag in between both force maxima. In the graph different colors are used to indicate different configurations and shapes are used to distinguish between the wave conditions.

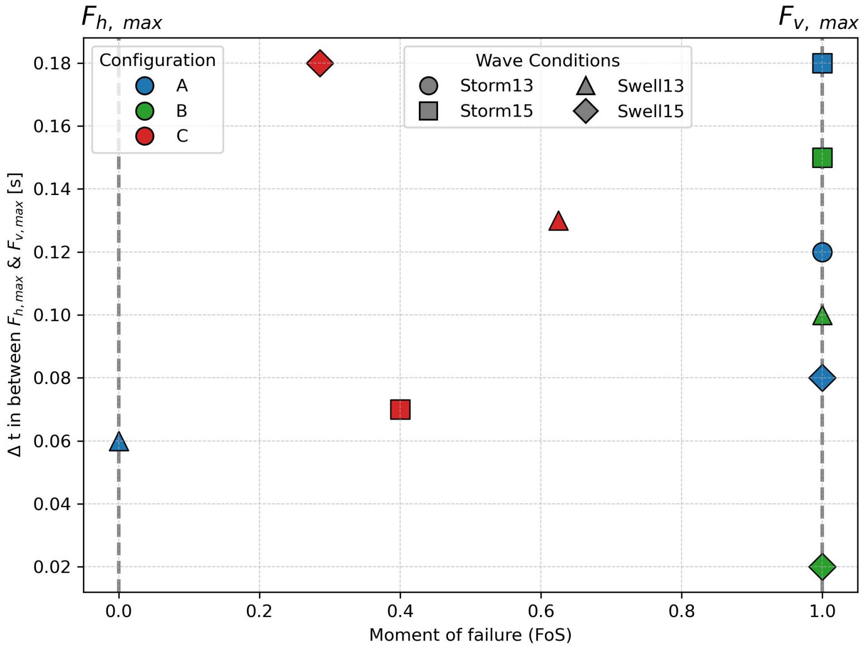

Figure 4.32: Moment of failure, for all configurations.

The analysis demonstrates that changing the armour configuration and position of the crown wall affects the timing of failure in relation to the force maxima. As illustrated in Fig. 4.32, the influence of the armor configuration on the moment of failure is evident. The measurements reveal that the time lag between the force maxima decreases when transitioning from configuration A to B. However, failure (the point of minimal factor of safety) still occurs during the maximum vertical force. Furthermore, shifting the crown wall further back (from configuration B to C) causes failure to occur between the force maxima, indicating that the point of failure moves forward in time. These findings highlight the importance of both armour configuration and crown wall positioning, in determining the timing and conditions of failure. Both factors should therefore also be considered during the design of crown walls on rubble mound breakwaters.

Part III

Conclusion

5 Conclusion

In this chapter, the conclusions drawn from the report are summarized. To maintain structure in this chapter, this is done by first addressing the sub-questions followed by the main research questions.

How can uplift pressure distribution and force better be described?

Current design methods assume a triangular pressure distribution along the base of the crown wall. Previous research has validated this assumption for scenarios with zero base freeboard. However, the findings from this study indicate that this triangular pressure distribution is also applicable for situations with minimal or near-zero freeboard across both tested permeabilities. Furthermore, this study delves into scenarios with non-zero base freeboard, specifically emphasizing changes in pressure distribution as a function of the base freeboard. The results indicate a decrease in pressure along the base, and in the most extreme situations, is no pressure at the back parts of the base. Based on the test results, this report proposes a novel method for determining forces, employing a two-step approach, which includes the effect of freeboard. According to early results, the traditional approach to calculate the forces tends to overestimate the forces at play. Therefore, correction factors are developed to accurately determine both the maximum horizontal and vertical forces, considering both the relative freeboard as the type of wave, since these showed great correlation. Since these encompass four distinct factors—vertical, horizontal, swell, and storm—only the general framework is presented here, while the detailed structure is elaborated upon in the subsequent chapter.

$$\gamma_{H,V;Storm\&Swell} = \frac{F_{h,0.1\%,Measured}}{F_{h,0.1\%,Pedersen}}$$

Subsequently, it is demonstrated that failure does not occur during the instance of maximum forces, but rather through a combination of both. This assumption has led to an overestimation, which can be compensated with the second reduction factor, where also a distinction is made between storm and swell waves.

$$\gamma_{FoS;Storm\&Swell} = \frac{F_{v,0.1\%,FoS}}{F_{v,0.1\%,Measured}}$$

Since nearly all crown walls are either overdesigned or designed based on physical model tests, applying one or both correction factors results in a significant reduction in the required material (e.g. concrete) compared to the use of the Pedersen (1996) method. This reduction not only decreases the amount of material needed for construction but also leads to a decrease in CO2 emissions during the construction of these components.

What is the impact of core permeability on the vertical and horizontal forces acting on a crown wall? Is stability of the crown wall influenced?

The effect of changing the core permeability was investigated in this study. The test findings showed that the lower core permeability led to a decrease in the maximum vertical forces. This reduction can be attributed to the smaller pore sizes, which enhance the core's ability to dissipate incoming wave energy, thereby increasing energy dissipation and damping within the porous medium. In contrast, the maximum horizontal forces showed an increase under all conditions for a lower core permeability. This increase develops because the smaller pores are less effective at absorbing incoming wave energy, leading to greater run-up and, consequently, increasing the horizontal forces of the crown wall. Both of these effects had a negative impact on stability, making the structure less stable as the permeability of the breakwater core decreased. Furthermore, it was observed that permeability influences the maximum forces, without affecting the ratio between the maximum forces and the forces that occur at the point of failure.

How do the horizontal forces develop as a function of different armour layouts, and how does this impact overall stability?

The horizontal forces are significantly impacted by the armour configuration used in front of the crown wall. In this study, multiple armour configurations were tested. It is observed that adding extra material, from configuration A to B, resulted in a 20.64% reduction in horizontal force. Additionally, the time lag between the maximum horizontal and vertical force decreased, and the stability was not affected by this adjustment. The greatest reduction in forces occurred when the wall is positioned further back (from layout B to C), leading to a reduction of 75.19%. This can be explained by the fact that, when the crest wall is moved further back, the wave tongue must travel a greater distance to reach the wall. As a result, it is possible that the wall does not experience a direct impact from the run-up, thereby avoiding a dynamic impact. As a result of this adjustment, the moment of failure shifted earlier in time, the time lag between the force maxima remained the same, and the overall stability increased due to this adjustment.

How do the vertical and horizontal pressure distributions on a crown wall develop?

Through model testing, this report examines the development of pressures both horizontally and vertically on crown walls with non-zero freeboard. The existing literature suggests that this scenario is still not fully understood, highlighting a knowledge gap regarding on this specific topic, indicating the need for further investigation. Additionally, this study conducts a thorough analysis of forces in relation to relative freeboard. Furthermore, the report studies the impact of permeability on the pressures, forces, and stability of crown walls. The investigation extends to the impact of various parameters—such as wave height, wave steepness, foundation level, and armor crest width—on both horizontal and vertical loading, and highlights their correlation with the acting forces. Moreover, it becomes evident that permeability has a significant impact on the forces and stability of a crown wall, underscoring its importance in the design of such structures. The importance of considering foundation level, permeability, and armor crest width is emphasized. Ultimately, a method is presented that accounts for the observed effects of non-zero freeboard on forces.

6 Limitations

In this chapter the limitations encountered during the research will be touched upon. So that future researchers can draw important lessons from this, which will improve the quality of their lab tests.

Set-up less permeable core

During the testing of the second set-up, movement of the core material was observed. This movement was possible because the material was not glued together, unlike in the first, permeable core. The movement occurred due to the impact of waves on the structure. As a result of this observed effect, it cannot be guaranteed that the friction coefficient remained constant throughout all the tests. Additionally, it is possible that the positional changes of the stones provided additional resistance to the wall, theoretically making it stronger and more resistant to failure. Although considerable effort was made during the tests to ensure that this factor did not play a significant role, it cannot be stated with certainty that the friction coefficient remained constant during the tests. This was, however, the case for the first set-up, where everything was glued in place.

Measured significant wave height

One potential improvement is the use of the measured H_s instead of the target H_s in the analysis, which could enhance the accuracy of the results. For all wave conditions (for both core types), it was verified that the measured H_s closely matched the target H_s, with the largest deviation being 8%. Given that the measurements showed small deviations, the target H_s was used for the following analysis. While incorporating the measured H_s could improve accuracy, it is expected that this would not have a significant impact on the overall results.

Instruments

As discussed in this report, the exposure of the instruments, sensors, or cables to water can influence the measurement results. Despite the special care taken to minimize these effects, it cannot be guaranteed that the cables or sensors remained dry and that the results are completely free from these influences. However, due to the nature of the set-up, which frequently comes into contact with water, it is impossible to determine this with certainty. Consequently, a different approach is needed. Therefore, it is recommended for future experiments to pre-wet all measurement instruments before testing begins, ensuring that the described effects no longer play a role.

7 Recommendations for future research

Following the main conclusions of the research, this chapter delves further into the recommendations and outlines the limitations of the study, suggesting methods to address these shortcomings in future research. Initially, recommendations concerning the physical model tests will be provided, followed by suggestions for subsequent stages of the research.

- **Sensors and cables**

  It is advised to ensure that the backside of the sensors remains either completely dry or fully submerged during the tests to counteract temperature effects. These temperature effects can occur when the sensors or cables become wet, leading to a shift in the pressure measurements. While this effect can be corrected during data processing, doing so may alter the initial pressure signal and potentially affect the final conclusions drawn from the data. Therefore, it is preferable to maintain the sensors in a consistent state (either dry or wet) to minimize the need for extensive data filtering. Possible solutions include using cable sleeves or sprinklers to ensure the sensors remain consistently wet during the tests. Additionally, it is prudent to use similar sensors and, more importantly, cables of the same length and thickness. This is crucial because if the cables become wet, they will exhibit similar temperature effects, simplifying the data processing. Different cables may respond differently to temperature changes, complicating the testing campaign. These adaptations could result on better measurements, ultimately increasing the understanding of forces acting on the crown wall.

- **Amplifiers**

  A concern encountered during this research, which was also noted by Veringa (2023), was the fast decay of the pressure signal after wave impact. Veringa partially addressed this issue by using a constant current (2 V) in the amplifiers instead of a constant voltage (10 V). However, this effect persisted in the current study. Upon comparing with the amplifiers used by Deltares, it was concluded that their amplifiers did not exhibit the fast decay effect, however, did measure noise level of similar magnitude. Therefore it is recommended to use amplifiers that do no measure both phenomenons.

- **Permeability**

  It is recommended to conduct additional model tests to investigate the influence of permeability on the stability of crown walls on top of rubble mound breakwaters. This research indicated that permeability significantly affects the uplift forces and stability of the crown wall. However, further research in this area is necessary. This is particularly important because the breakwater core used in this study, characterized by 'wide graded' material ($D_{n,85}/D_{n,85} = 2.21 and 2.03$), does not fully represent real-world conditions, where 'quarry run' gradation with $D_{n,85}/D_{n,85} > 2.5$ is commonly used.

- **Test set-up**

  It is recommended that, if further research is conducted on the influences of permeability, the breakwater core used should be glued together. This would ensure that the friction coefficient remains constant throughout the study, preventing it from having an additional impact on the stability criterion.

- **Breakwater geometries**

  For further research, it is recommended to conduct tests with different breakwater geometries, as this study only utilized a relatively simple geometry. Incorporating various filter layers, different armor types, and varying filter layer widths could lead to a better understanding of the forces acting on the crown wall. This is particularly important as these factors are expected to influence the forces significantly.

- **Continuation of the data set**

  Moreover, since some of the report's conclusions are based on a limited number of tests, continued testing efforts that include a wider range of hydraulic conditions (e.g., varying water depths, wave heights, and periods) are recommended. This could lead to more generalized conclusions applicable to a broader spectrum of geometries and hydraulic conditions. Extending this analysis may also enhance existing design methods or result in the development of entirely new methodologies, ultimately expanding the knowledge in this field.

- **Transition to numerical simulations**

  A growing trend in the field of coastal engineering is the increased use of numerical models. Consequently, it is recommended to incorporate numerical simulations in further research. The data set gathered from this study could be used for the calibration of such models. A calibrated model would facilitate the testing of various configurations and variables with greater ease, and examining a broader and more diverse set of variables could help to refine and improve the results.

Bibliography

Bekker, J. (2017). *Experimental research into the effect of freeboard on the stability of a crown wall on a rubble mound breakwater* [Doctoral dissertation, Delft University of Technology].

Bekker, J., Hofland, B., & Smith, G. (2018). Experiments on the effect of freeboard on the stability of a breakwater crown wall. *Proceedings of the Coastal Engineering Conference*, *36*(2018), 2018. https://doi.org/10.9753/icce.v36.papers.9

CIRIA, CUR, & CETMEF. (2007). *The Rock Manual. The use of rock in hydraulic engineering (2nd edtion)* (CIRIA London, Ed.).

Dai, Y. D., & Kamel, A. M. (n.d.). *Scale Effect Tests For Rubble-Mound Breakwaters* (tech. rep.). U.S. Army Engineer Waterways Experiment Station. Vicksbrug.

Frostick, L. E., McLelland, S. J., & Mercer, T. (Eds.). (2011, May). *Users Guide to Physical Modelling and Experimentation*. CRC Press. https://doi.org/10.1201/b11335

Günback, A., & Göcke, T. (1984). Wave screen stability of rubble mound breakwaters. *Proceedings of the International Symposium on Maritime Structures in the Mediterranean Sea, Athens, Greece,* 2099–2112.

Han, X., Jiang, Y., & Dong, S. (2022). Wave forces on crown wall of rubble mound breakwater under swell waves. *Ocean Engineering*, *259*, 111911. https://doi.org/10.1016/j.oceaneng.2022.111911

Heller, V. (2011). Scale effects in physical hydraulic engineering models. *Journal of Hydraulic Research*, *49*(3), 293–306. https://doi.org/10.1080/00221686.2011.578914

Iribarren, R., & Nogales, C. (1954). *Obras Marı´timas: Oleaje y Diques*. Dossat Madrid, Spain (in Spanish).

Losada, M. A., & Giménez-Curto, L. A. (1980). Flow characteristics on rough, permeable slopes under wave action. *Coastal Engineering*, *4*(100), 187–206. https://doi.org/10.1016/0378-3839(80)90019-8

Martin, F. L., Losada, M. A., & Medina, R. (1999). Wave loads on rubble mound breakwater crown walls. *Coastal Engineering*, *37*(2), 149–174. https://doi.org/10.1016/S0378-3839(99)00019-8

Molines, J., Herrera, M. P., & Medina, J. R. (2018). Estimations of wave forces on crown walls based on wave overtopping rates. *Coastal Engineering*, *132*, 50–62. https://doi.org/10.1016/j.coastaleng.2017.11.004

Negro Valdecantos, V., López Gutiérrez, J. S., & Polvorinos Flors, J. I. (2013). Comparative study of breakwater crown wall - calculation methods. *Proceedings of the Institution of Civil Engineers: Maritime Engineering*, *166*(1), 25–41. https://doi.org/10.1680/maen.2010.29

Nørgaard, J. Q. H., Andersen, T. L., & Burcharth, H. F. (2013). Wave loads on rubble mound breakwater crown walls in deep and shallow water wave conditions. *Coastal Engineering*, *80*, 137–147. https://doi.org/10.1016/j.coastaleng.2013.06.003

Pedersen, J. (1996). *Wave Forces and Overtopping on Crown Walls of Rubble Mound Breakwaters an Experimental Study* [Doctoral dissertation, Aalborg University].

Reedijk, B., Muttray, M., van den Berge, A., & de Rover, R. (2009). EFFECT OF CORE PERMEABILITY ON ARMOUR LAYER STABILITY. *Coastal Engineering 2008*, 3358–3367. https://doi.org/10.1142/9789814277426{_}0278

Schiereck, G. J. (2019). *Introduction to Bed, Bank and Shore Protection* (H. Verhagen, Ed.). CRC Press. https://doi.org/10.1201/9781315274935 van Gent, M. R. A. (1995a). Porous Flow through Rubble-Mound Material. *Journal of Waterway, Port, Coastal, and Ocean Engineering*, *121*(3), 176–181. https://doi.org/10.1061/(ASCE)0733-950X(1995)121:3(176)

van Gent, M. R., van den Boogaard, H. F., Pozueta, B., & Medina, J. R. (2007). Neural network modelling of wave overtopping at coastal structures. *Coastal Engineering*, *54*(8), 586–593. https://doi.org/10.1016/j.coastaleng.2006.12.001

van Gent, M. R., & van der Werf, I. M. (2019). Influence of oblique wave attack on wave overtopping and forces on rubble mound breakwater crest walls. *Coastal Engineering*, *151*, 78–96. https://doi.org/10.1016/j.coastaleng.2019.04.001

van Gent, M. (1995b). *Wave Interaction with Permeable Coastal Structures* [Doctoral dissertation, Technische Universiteit Delft].

van der Meer, J. W., & Stam, C.-J. M. (1992). Wave runup on smooth and rock slopes of coastal structures. *Journal of Waterway, Port, Coastal and Ocean Engineering*, *118*(5), 534–550. https://doi.org/10.1061/(ASCE)0733-950X(1992)118:5(534)

van der Meer, J. (1988). *Rock slopes and gravel beaches under wave attack* [Doctoral dissertation].

Veringa, M. (2023). *Wave Loads on Emerged Breakwater Crown Walls, a Physical Model Study* [Doctoral dissertation, Delft University of Technology].

Wolters, G., van Gent, M., Hofland, B., & Wellens, P. (2014). Wave damping and permeability scaling in rubble mound breakwaters. *Coastlab*.

Wolters, G., van Gent, M., Allsop, W., Hamm, L., & Muhlestein, D. (2010, January). HYDRALAB III: Guidelines for physical model testing of rubble mound breakwaters. In *Coasts, marine structures and breakwaters: Adapting to change* (pp. 559–670). Thomas Telford Ltd. https://doi.org/10.1680/cmsb.41318.0062

Part IV

Appendices

A

Appendix A: Experimental set-up


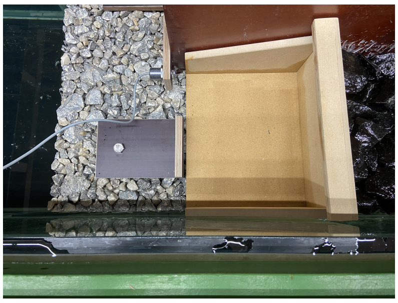


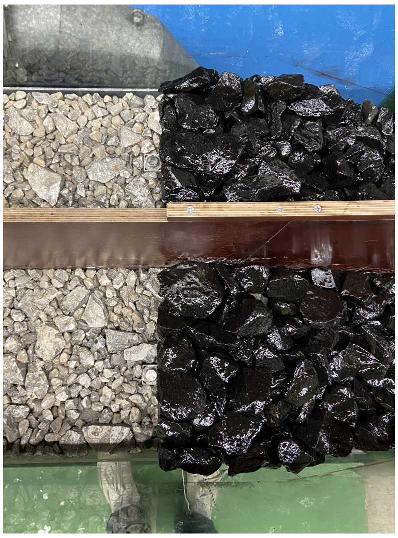

B

Appendix B: Permeability Tests

(a) Set-up used to perform the constant head test

(b) Mesh used to keep sample at its place

Figure B.1: Images of the constant head test

As highlighted in Section 3.5, the constant head test was conducted to measure the permeability of both core samples. The test was performed using the setup shown in Fig. B.1a, where a small head difference was created by allowing water to flow through the set-up. By recording the time it took for a known volume of water to pass through the setup, the permeability of the core samples could be determined using the equation provided below. To ensure accuracy and reliability, the test was performed multiple times.

$$k = \frac{qL}{Ah} = \frac{QL}{Aht} \tag{B.1}$$

C

Appendix C: Instruments

Multiple instruments have been employed to collect data during the testing campaign. The data obtained through the sensors is an analog output signal with a voltage range of -10 to 10 volts. This signal is then sent to a computer where the DaisyLab software for data gathering is used. The raw data signal, consisting of a signal representing varying voltages over time, is converted and processed to obtain valueble insights, with the help of python.

Pressure transducers (Kulite's HKM-375M)

The Kulite HKM-375M pressure transducers are the primary instruments used in the testing campaign to measure pressure along both sides of the crown wall. These sensors were mounted flush with the exterior of the crown wall and have a measurement range of 1 bar. To enhance the clarity of the results, the signals were amplified using signal amplifiers. During the tests, measurements were recorded at a frequency of 100 Hz, following the recommendation of Han et al. (2022), who indicated that this frequency would yield results comparable to those obtained at higher frequencies. The layout of the sensors is illustrated in Appendix G.

Wave gauges

To ensure that the incident wave conditions during each test corresponded to the pre-specified parameters, a system of multiple wave gauges was utilized. These submerged probes measure the conductivity of the water column above them. Given the reflection caused by the breakwater within the flume, it was necessary to deploy multiple gauges to effectively separate the reflected and incoming wave components. This separation was achieved using a set of three wave gauges, spaced optimally at distances of 30 and 40 cm, as recommended by Wolters (2010) in HYDRALAB studies on breakwaters. The DECOMP tool from the TU Delft Waterlab was employed to analyze the wave data collected in the flume. In this study, two sets of three gauges were used: one set positioned close to the structure and another set placed further away. The design choices regarding this set-up are further elaborated in Section 3.7, which provides an overview of the flume configuration.

Magnetic Proximity Switch

Since the stability tests were based on displacement, it was crucial to accurately measure any movement. This was accomplished using a magnetic proximity switch specific. The magnetic switch used for this purpose has a range of 2 cm and measures with an accuracy of 0.2 mm. It was attached to the rear side of the wall to monitor horizontal displacement.

D

Appendix D: Wave Analysis

Permeable set-up

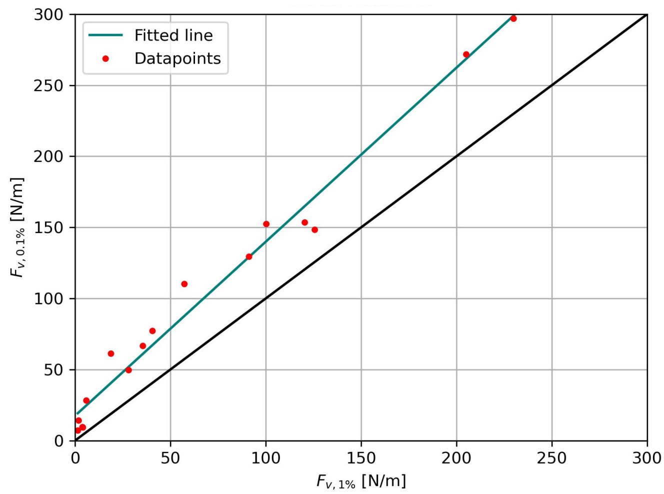

Figure D.1: Fitted line through $F_{v,1\%}$ to calculate $F_{v,0.1\%}$ (permeable core)

General Settings	Value
Slope	1.224
Intercept	17.471
R-squared	0.986
R - Value	0.993

Table D.1: Regression statistics set-up 1

With these regression statistics, the relation to determine the maximal uplift forces without any vulnerability for outliers can be seen in Eq. (D.1).

$$F_{u,0.1\%} = 1.224 * F_{u,1\%} + 17.471 \tag{D.1}$$

Less Permeable set-up

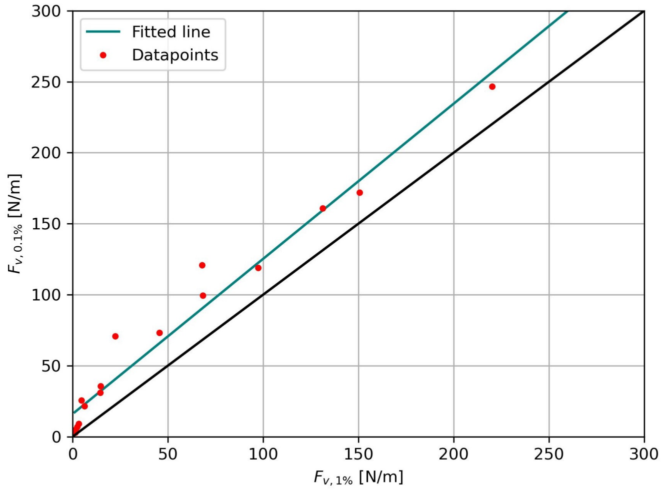

Figure D.2: Fitted line through $F_{v,1\%}$ to calculate $F_{v,0.1\%}$ (less permeable core)

General Settings	Value
Slope	1.093
Intercept	15.974
R-squared	0.964
R - Value	0.982

Table D.2: Regression statistics set-up 2

With these regression statistics, the relation to determine the maximal uplift forces without any vulnerability for outliers can be seen in Eq. (D.2).

$$F_{u,0.1\%} = 1.093 * F_{u,1\%} + 15.974 \tag{D.2}$$

E

Appendix E: Test Program

	#	s [-]	Hs [m]	Fc [m]	h [m]	Type
Freeboard tests (Core 1 and 2)	1	0.04	0.11	0.03	0.57	**Base Case**
	2	0.04	0.13	0.03	0.57	
	3	0.04	0.15	0.03	0.57	
	4	0.015	0.11	0.03	0.57	
	5	0.015	0.13	0.03	0.57	
	6	0.015	0.15	0.03	0.57	
	7	0.04	0.11	0.05	0.55	**Modification 1 (freeboard 0.05 m)**
	8	0.04	0.13	0.05	0.55	
	9	0.04	0.15	0.05	0.55	
	10	0.015	0.11	0.05	0.55	
	11	0.015	0.13	0.05	0.55	
	12	0.015	0.15	0.05	0.55	
	13	0.04	0.11	0.01	0.59	**Modification 2 (freeboard 0.01 m)**
	14	0.04	0.13	0.01	0.59	
	15	0.04	0.15	0.01	0.59	
	16	0.015	0.11	0.01	0.59	
	17	0.015	0.13	0.01	0.59	
	18	0.015	0.15	0.01	0.59	
Horizontal tests	19	0.04	0.13	0.03	0.57	**Set-up B**
	20	0.04	0.15	0.03	0.57	
	21	0.015	0.13	0.03	0.57	
	22	0.015	0.15	0.03	0.57	
	23	0.04	0.13	0.03	0.57	**Set-up C**
	24	0.04	0.15	0.03	0.57	
	25	0.015	0.13	0.03	0.57	
	26	0.015	0.15	0.03	0.57	

Table E.1: Test program used in research

F

Appendix F: Grading

	Nominal diameter [cm]		
Passing percentage	Armour	Permeable core	Less permeable core
10	4.34	1.58	0.64
15	4.48	1.65	0.69
50	5.34	2.21	0.92
60	5.55	2.36	1.05
85	6.16	3.65	1.40

Table F.1: Sample characteristics

	Grading		
	Armour	Permeable core	Less permeable core
D_{n85}/D_{n15}	1.42	2.21	2.03
Type	Narrow	Wide	Wide

Table F.2: Grading type

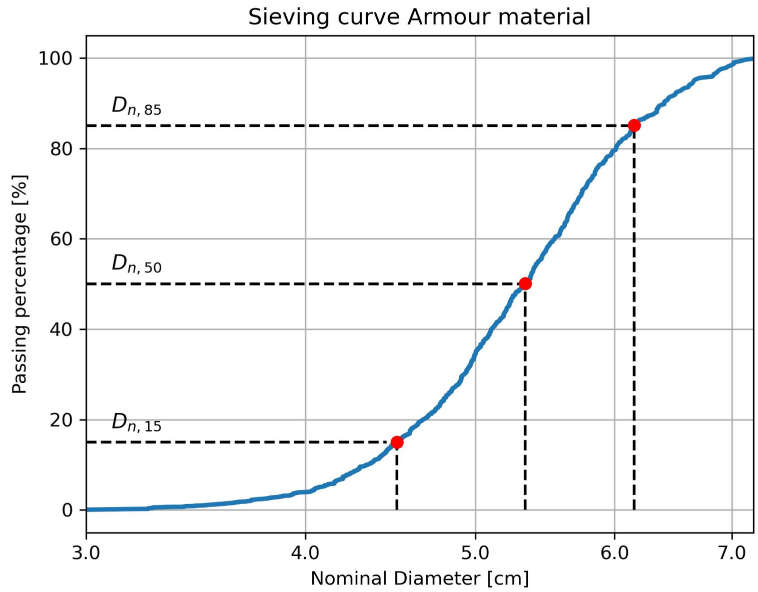

Figure F.1: Sieve curve of the armour layer, with characteristic values (summerized in Appendix F)

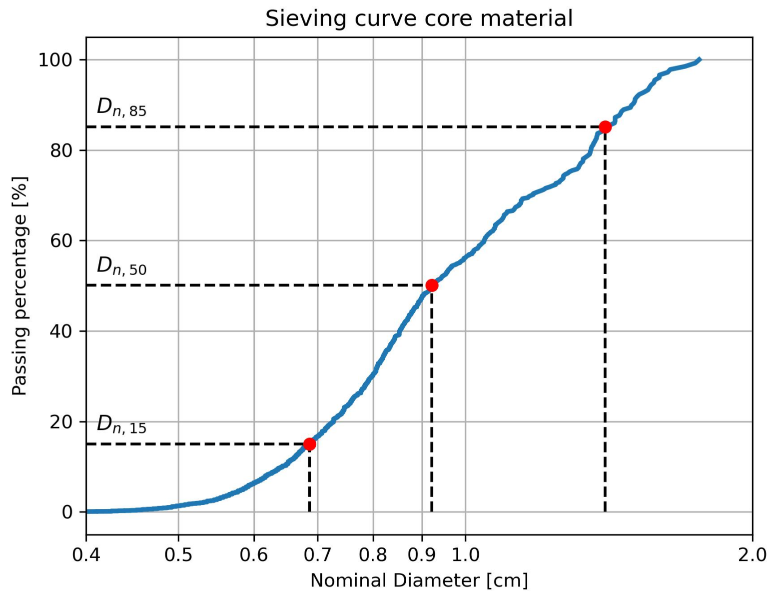

Figure F.2: Sieve curve of the less permeable core, with characteristic values (summerized in Appendix F)

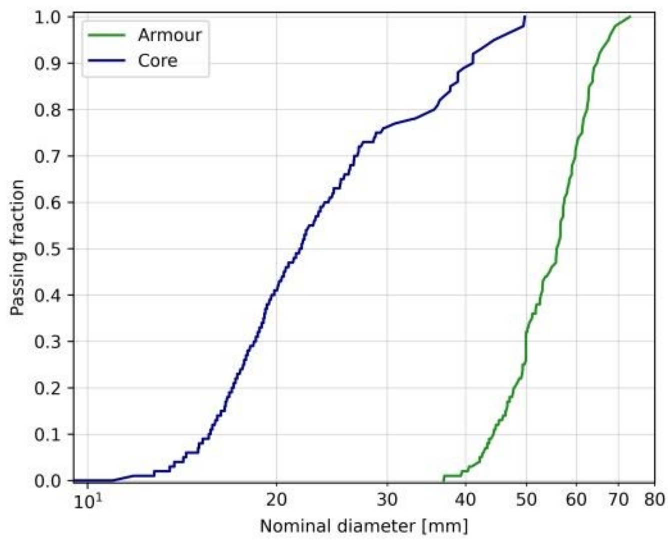

Figure F.3: Sieve curve of the permeable core (only the core sieve curve is of importance)

G

Appendix G: Sensor Placement

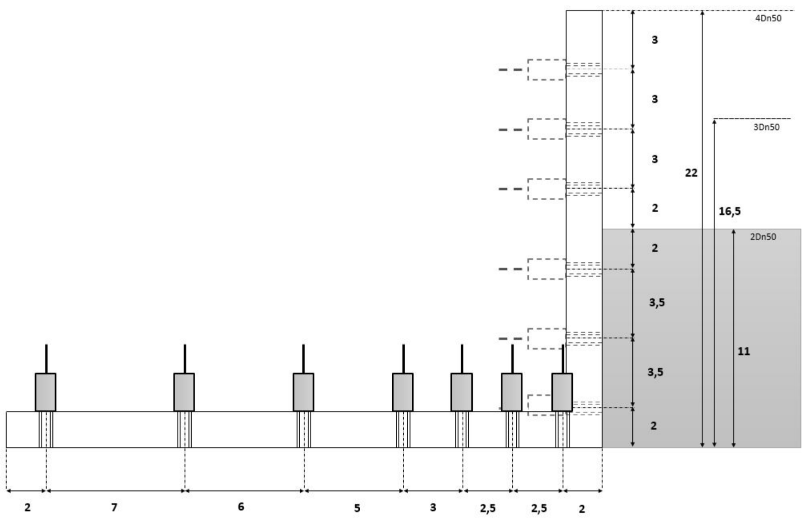

Figure G.1: Sensor placement in crown wall base

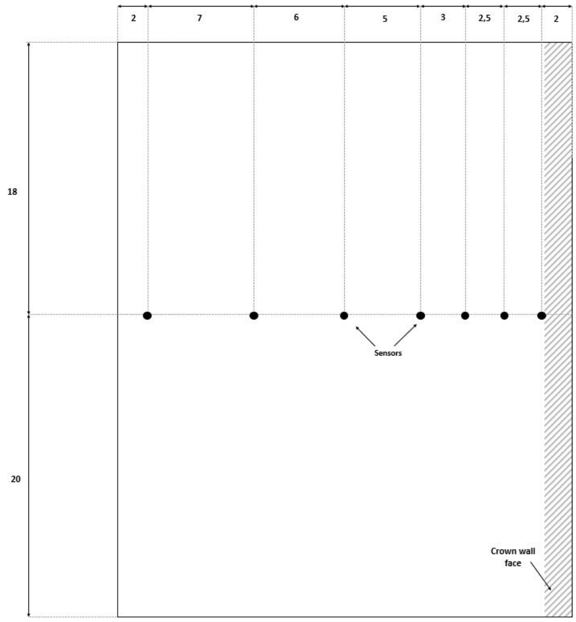

Figure G.2: Overview and dimensions of crown wall base

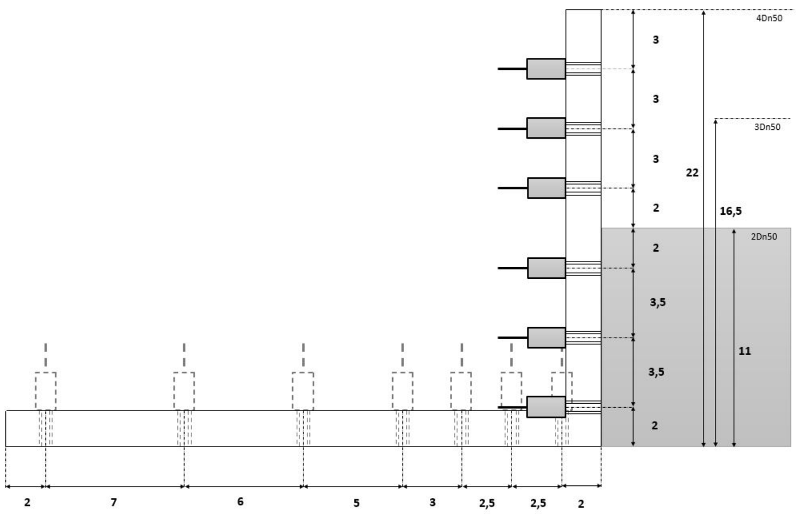

Figure G.3: Sensor placement in crown wall face

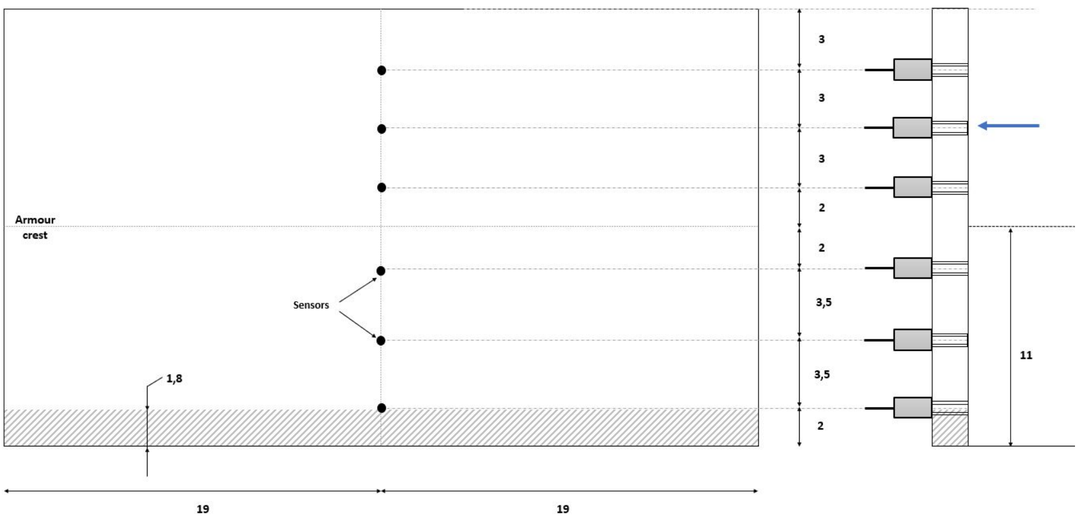

Figure G.4: Overview and dimensions of crown wall face

H

Appendix H: Horizontal Configurations

The values used, to construct Fig. 4.16, are given in Table H.1, seen below.

Wave conditions		$F_{h,1\%}$ **(N/m) per set-up**			**Change A - B**	**Change B - C**
s [-]	**Hs [m]**	**Set-up A**	**Set-up B**	**Set-up C**		
0.04	0.13	11.84	9.63	3.28	-18.65%	-65.95%
0.04	0.15	28.11	18.42	4.18	-34.47%	-77.28%
0.02	0.13	93.62	71.66	20.16	-23.46%	-71.87%
0.02	0.15	162.64	152.92	21.92	-5.98%	-85.67%

Table H.1: Reduction $F_{h,1\%}$ (N/m) per set-up

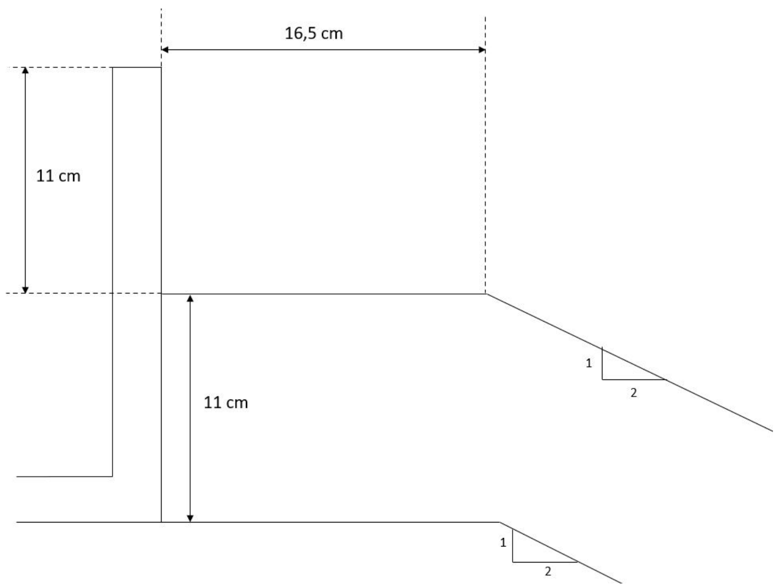

Figure H.1: Sketch and dimensions of setup A (Main test set-up)

In Fig. H.1 the main test set-up can be seen, which is used in the majority of all the tests in the testing campaign. Here, the armour layer thickness of 2 $D_{n,50}$, 11 cm, is illustrated, as is the armour crest width of 3 $D_{n,50}$. In set-up B, additional material was added by increasing the armour layer by one layer of stone to 3 $D_{n,50}$, as shown in the shaded area of the illustration. However, this resulted in the crest width no longer meeting the 2 $D_{n,50}$ requirement.

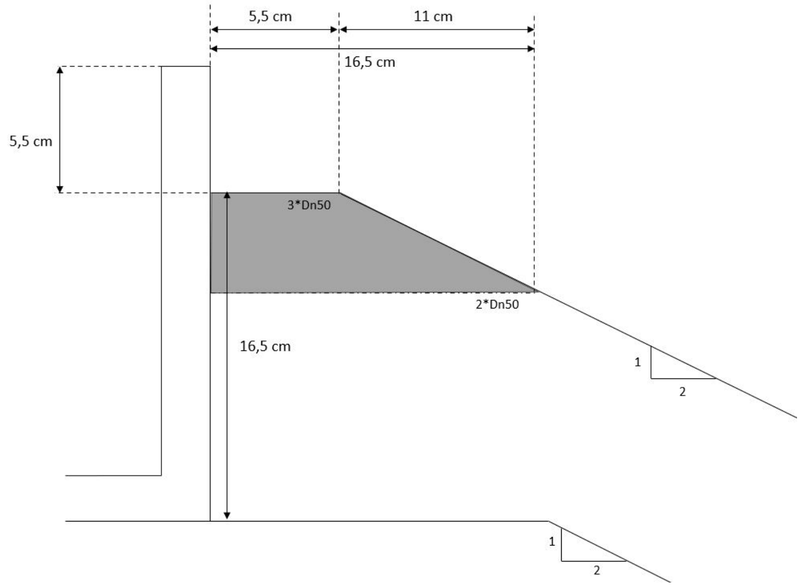

Figure H.2: Sketch and dimensions of set-up B

To meet the requirement of a crest width of 3 $D_{n,50}$ setup C was created by shifting the crown wall backward. This modification facilitates the testing of various adjustments, specifically the comparison of the influence of increasing the armor thickness and further shifting the crown wall.

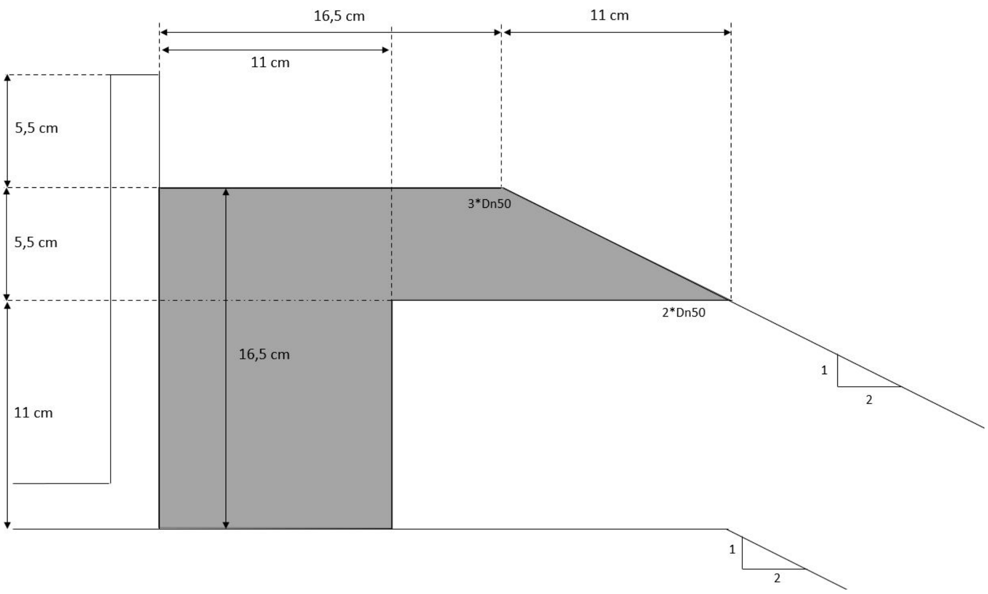

Figure H.3: Sketch and dimensions of set-up C

Horizontal force reduction

For completeness, the graph displaying the maximum horizontal forces is also provided. As discussed in Section 4.2, this method is sensitive to outliers. Nonetheless, it can be observed that this graph exhibits a similar behavior to that shown in Fig. 4.16, which analyzes the 1% horizontal forces.

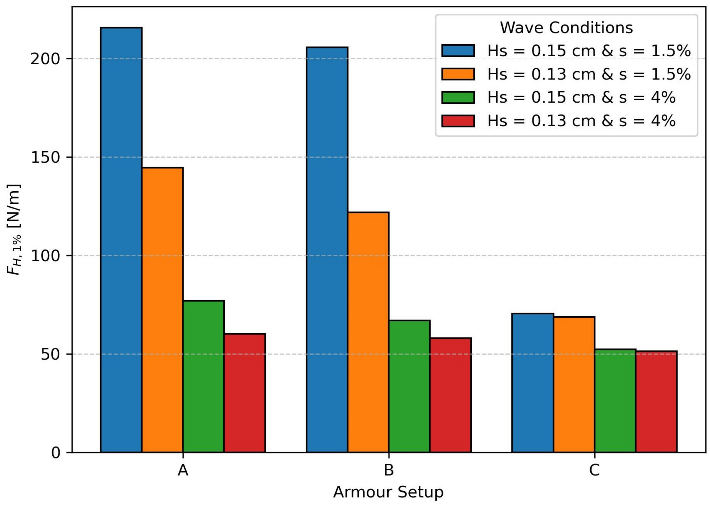

Figure H.4: Horizontal forces (0.1%) per set-up

Appendix I: Moment of failure

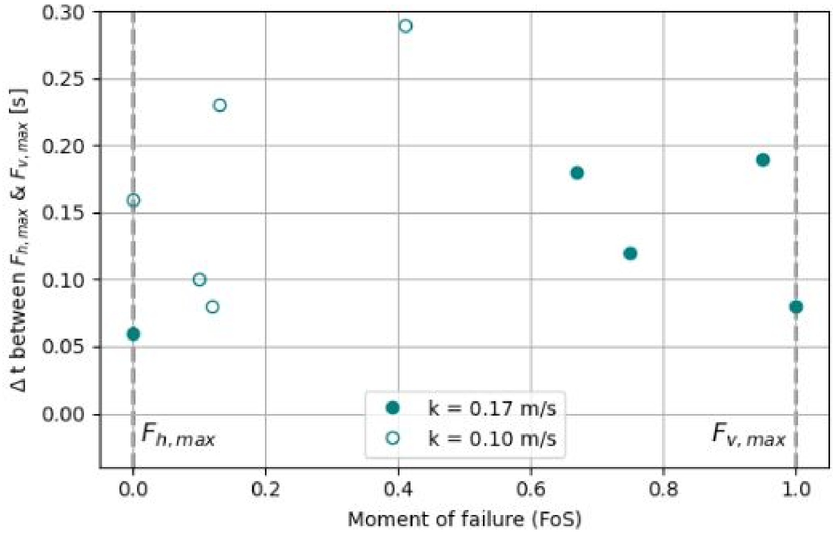

Figure I.1: Influence of permeability on the moment of failure for a 3 cm freeboard (Base case).

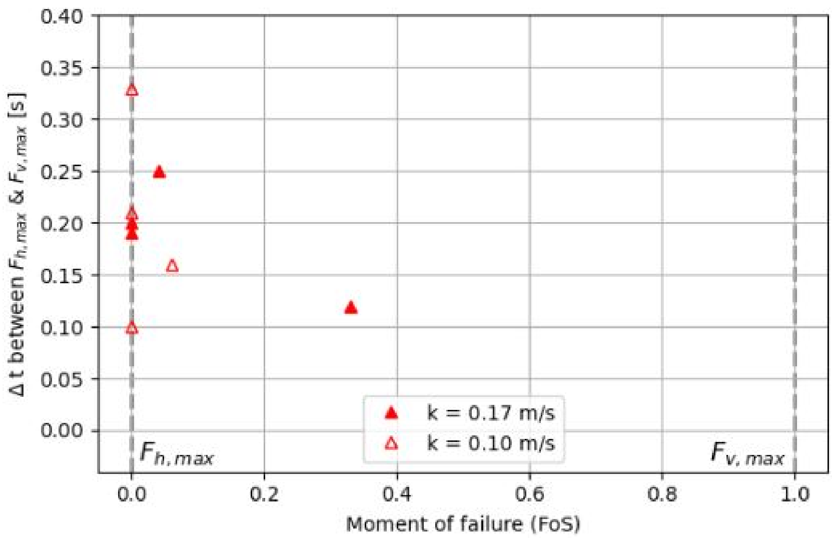

Figure I.2: Influence of permeability on the moment of failure for a 5 cm freeboard (Modification 1)

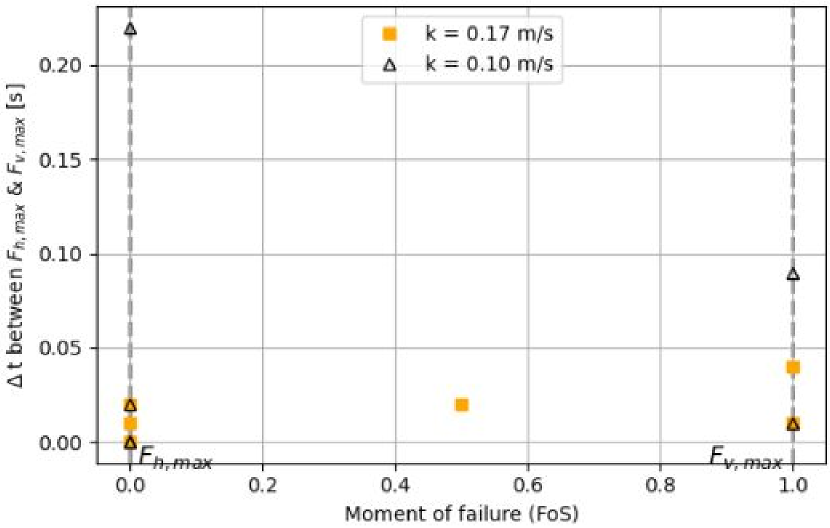

Figure I.3: Influence of permeability on the moment of failure for a 1 cm freeboard (Modification 2)